ABSTRACT

Title of dissertation: A SEARCH FOR Z BOSON PAIR PRODUCTION AT THE FERMILAB TEVATRON COLLIDER

Chad R. Jarvis
Doctor of Philosophy, 2007

Dissertation directed by: Professor Nicholas J. Hadley
Department of Physics

This dissertation describes a search for Z/γ^* boson pair production decaying into $\mu\mu\mu\mu$, $\mu\mu ee$, and $eeee$ final states with approximately 1 fb^{-1} of data at the Fermilab Tevatron Collider at $\sqrt{s} = 1.96$ TeV. The small cross section times branching ratio for each channel mandated a thorough study of the acceptance and efficiencies. After optimization, 1.7 ± 0.1 events are expected for Standard Model production with a background of 0.13 ± 0.03 events. One event was found in the $\mu\mu ee$ channel. A cross section limit of 4.4 pb is determined at a 95% confidence level for Standard Model production.

Additionally, one parameter and two parameter 95% C.L. limits are found for the anomalous neutral trilinear gauge couplings ZZZ^* and $ZZ\gamma^*$. The one parameter 95% C.L. coupling limits with a form factor scale of 1.2 TeV are: $-0.28 < f_{40}^Z < 0.28$, $-0.31 < f_{50}^Z < 0.29$, $-0.26 < f_{40}^\gamma < 0.26$, and $-0.30 < f_{50}^\gamma < 0.28$.

A SEARCH FOR Z BOSON PAIR PRODUCTION AT THE FERMILAB TEVATRON COLLIDER

by

Chad Jarvis

Dissertation submitted to the Faculty of the Graduate School of the
University of Maryland, College Park in partial fulfillment
of the requirements for the degree of
Doctor of Philosophy
2007

Advisory Committee:
Professor Nicholas J. Hadley, Chair/Advisor
Professor Andrew R. Baden, Co-Advisor
Associate Professor Douglas A. Roberts
Professor Stephen J. Wallace
Professor Alice Mignerey

Dedication

To my family, most of all, my parents George and Alice Jarvis

Acknowledgments

Now is the time for me to acknowledge and thank the people and friends who have inspired me and helped me during my tenure in graduate school.

At Maryland, I have been fortunate to have developed good relationships with the CERN and Fermilab professors: Andris Skuja , Drew Baden , Nick Hadley, and Sarah Eno.

First, I would like to thank Sarah. Her happy demeanor led me to approach the Maryland HEP group in the first place. I greatly appreciate her helpful insight into analysis and her advice. After Sarah's suggestion, I spoke with Andris and he sent me to CERN for the summer. At CERN I worked with Richard Kellogg. Dick's passion for his work was my first major inspiration for pursing a career in experimental particle physics (EPP). Drew sent me to CERN for two more summers to work with Dick. I greatly appreciate Andris and Drew giving me the opportunity to work at CERN. I also want to thank Drew for encouraging me to pursue my own interests at Fermilab. Most of all, I would like to thank Nick. I feel extraordinarily lucky to have had Nick as my advisor. Nick has always found time to help me and educate me.

I would also like to thank Tom Diehl for inspiring me to continue a career in EPP. Tom Diehl joined me at lunch in Wilson Hall in 2005 and proceeded to draw Feynman diagrams (on napkins) of trilinear and quartic gauge boson couplings. After having spent a year doing lepton efficiencies studies, it was exhilarating to

finally see physics again. Probably the most important lesson I have learned from him is to keep the focus on physics and to remember to see the forest through the trees. I have really enjoyed working in the di-boson group with Tom and Adam Lyon.

A number of other people have helped me both at Maryland and Fermilab: Michiel Sanders, Terry Toole, Jeremy Mans, Matt Wetstein, Junjie Zhu, Ming Yang, Lei Wang, Sally Megonigal, and Ivo.

I am very grateful to my my parents and siblings for supporting me through college and graduate school. Lastly but not least I want to thank Arin for her years of friendship and support.

Table of Contents

List of Figures

List of Abbreviations

SM	Standard Model
EM	Electromagnetic
EW	Electroweak
MET	Missing Transverse Energy
SMT	Silicon Microstrip Tracker
CFT	Central Fiber Tracker
VLPC	Visible Light Photon Counter
WLS	Wave length Shifting
CPS	Central Preshower
FPS	Forward Preshower
MIP	Minimum Ionizing Particle
EC	Endcap Calorimeter
CC	Central Calorimeter
FH	Fine Hadronic
CH	Coarse Hadronic
ICD	Inner Cryostat Detector
ICR	Inner Cryostat Region
PDT	Proportional Drift Tube
MDT	Mini Drift Tube
PMT	Photo Multiplier Tube
MUC	Central Muon Detector
MUF	Forward Muon Detector
L1, L2, L3	Level 1, 2, 3 (trigger)
ADC	Analog to Digital Converter
DCA	Distance of Closest Approach
HTF	Histogram Track Finder
AA	Alternative Algorithm

Chapter 1

Introduction and Theory

1.1 Particle Physics

Particle physics is the branch of physics which describes, or attempts to describe, matter and its interactions at the most fundamental level. There have been many ideas through out recored history which have postulated matter being made of "uncuttable" building blocks. The first scientific evidence for some kind of discrete blocks of matter was the reactions of chemicals in simple proportions explained in the mid 19th century by atoms. However, it was not until 1897 that the first indivisible particle, the electron, was discovered. This is often defined to be the beginning of elementary particle physics. As of the year 2007, one hundred and ten years after its discovery, the electron has survived all attempts to cut it into smaller pieces.

Since the discovery of the electron, atoms have been found to be composed of smaller particles: electrons, protons, and neutrons. These particles make up most of the visible mass of the universe. Along with the photon, the search for the fundamental building blocks could have ended with these particles. However, after the discovery of the neutron, muons and pions were discovered. Particle physics quickly became complicated as more exotic particles were discovered such as neutrinos and kaons. Neutrons and protons are now known to have substructure and to be composed of more fundamental particles called quarks. The total number

of known particles is mind numbing and far exceeds the total number of known atoms in the periodic table. Most of these particles, however, are not elementary. Fortunately, a very successful theory has developed which describes all the known particles from a few handfuls of elementary particles and a few particles responsible for their interactions. This theory is known as the Standard Model (SM).

1.1.1 Standard Model

The elementary particles can be separated into two classes: fermions and bosons. Fermions make up the matter particles and have half-integer spin. Bosons are the force mediating particles and have integer spin. No more than one fermion can occupy the same quantum state (the Pauli Exclusion Principle). Bosons, however, do not have this restriction.

1.1.1.1 Fermions - the Matter Particles

The matter particles are subdivided into two types known as leptons and quarks. The leptons and quarks each have three generation of particles. Each generation has the same properties except the mass of the particles between generations differ. Each generation of leptons has a charged lepton and one neutral lepton called a neutrino. For example, the first generation of leptons has the charged electron and the neutral electron-neutrino. Each generation of quarks has a quark with +2/3 charge and a quark with -1/3 charge. For example the first generation of quarks has the up quark and the down quark. Every charged fermion has an anti-particle with

the same mass and opposite charge. The fermions have other quantum numbers such as weak isospin and hypercharge. The anti-particles of the charged fermions do not have the same weak isospin or hypercharge; charged anti-particles are not simply the same mass particle with opposite charge. It is not yet know if the neutral fermions, the neutrinos, have an anti-particle that is a different particle[1]. See Table 1.1 for a summary of all the fermions.

	Generation 1		Generation 2		Generation 3		Charge
Quarks	Up	u	Charm	c	top	t	2/3
	Down	d	Strange	s	bottom	b	-1/3
Leptons	Electron	e	Muons	μ	Tau	τ	1
	Electron-neutrino	ν_e	Muon-neutrino	ν_μ	Tau-neutrino	ν_τ	0

Table 1.1: Elementary matter particles - the Fermions

Composite particles of quarks are grouped into two types: baryons and mesons. Baryons, such as the proton, are made of three quarks. Mesons, such as the pions, are composed of a quark and an anti-quark.

1.1.1.2 Bosons - the Force Particles

Interactions (or forces) between the leptons and quarks are mediated by particles called gauge bosons. The number of fundamental forces is conventionally given as four: strong, weak, electromagnetic, and gravitation. The Standard Model does

[1]Fermions with the same anti-particle are known as Majorana fermions. Neutrinoless double beta decay, if it occurs, would verify that neutrinos are Majorana fermions.

not include gravitation. However, if gravitation is to be consistent with the quantum field theory for point particles, it must be mediated by a spin 2 particle. The SM includes a fifth kind of interaction which gives mass to particles. This interaction is denoted the Higgs force and is mediated by the Higgs boson. The Higgs boson has yet to be observed, however, unlike the graviton, it is consistent with the Standard Model. Table. 1.2 shows a summary of all the forces and their corresponding gauge boson(s).

Force	Particle	Particle Symbol	Mass(GeV/c^2)	Spin
Strong	Gluon	$g_\alpha(\alpha = 1, 2, 3, ...8)$	0	1
Electromagnetic	Photon	γ	0	1
Weak	W^+,W^- boson	W^+,W^-	80.398 ± 0.025	1
	Z boson	Z	91.1876 ± 0.0021	1
Higgs	Higgs boson	H	> 114	0
Gravitation	Graviton	G	0	2

Table 1.2: Interaction elementary particles - the Bosons. Gravitation is not in the Standard Model.

Figure. 1.1 shows a schematic of all the particles in the Standard Model (except for the anti-particles of the fermions) including linking lines representing the interactions among the particles. Note that gluons only interact with the quarks (and themselves), the photon only with charged particles, and the Higgs boson only with particles which have mass. Also note that the neutral gauge bosons can interact with the charged gauge bosons.

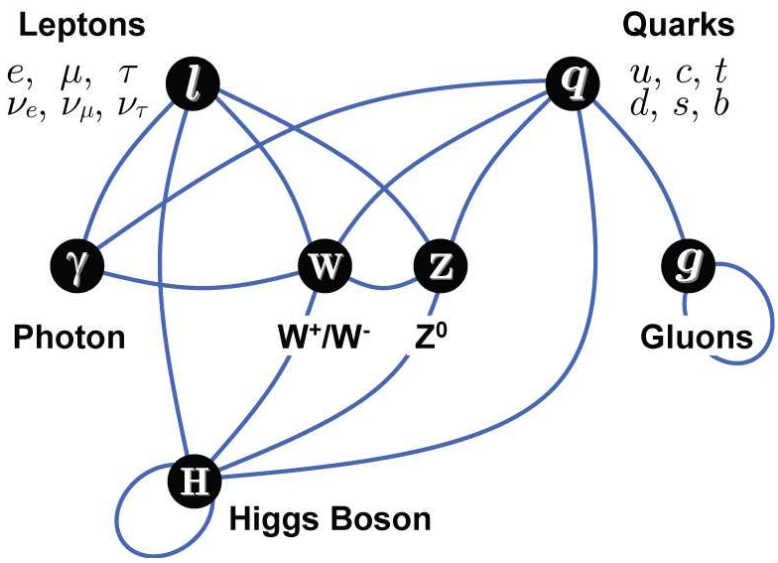

Figure 1.1: Particles that make up the Standard Model including connecting lines indicating interactions between the particles. The anti-particles of the fermions are not shown.

1.1.2 Theoretical Formalism

The Standard Model is a relativistic quantum field theory within the gauge group $\mathrm{SU(3)_C \times SU(2)_L \times U(1)_Y}$. The $\mathrm{SU(3)_C}$ group represents the strong interactions and its generators are the eight gluons $g_\alpha(\alpha = 1, 2, 3, ...8)$. The $\mathrm{SU(2)_L \times U(1)_Y}$ group represents the electroweak (EW) interactions whose interactions (after breaking the symmetry) are mediated by the $W^\pm$ bosons, the Z boson, and the photon. For this analysis, gluon interactions only play a small role[2] and therefore we will concentrate our discussion on the electroweak component [1] of the SM.

The generators of the $\mathrm{SU(2)_L}$ group are the weak isospin $W^i_\mu(i = 1, 2, 3)$ bosons

[2]For example, the p_T of the Z bosons from $p\bar{p} \to ZZ$ arises primarily from the tree-level recoil of one Z boson off the other and not from higher order initial state gluon radiation.

with coupling constant g' and the generator of the $\mathrm{U(1)_Y}$ group is the weak hypercharge boson B_μ with coupling constant g. Corresponding to these gauge bosons are the field-strength tensors

$$F^{\ell}_{\mu\nu} = \partial_\nu W^{\ell}_{\mu} - \partial_\mu W^{\ell}_{\mu} + g\,\epsilon_{jkl}\,W^{j}_{\mu}\,W^{k}_{\nu} \tag{1.1}$$

for the weak isospin symmetry, and

$$f_{\mu\nu} = \partial_\nu B_\mu - \partial_\mu B_\nu \tag{1.2}$$

for the weak-hypercharge symmetry.

The weak interactions only couple to left handed particles, however, electromagnetic (EM) interactions couple to both left and right handed particles. Therefore, we write the lepton field as a left handed weak isospin doublet:

$$L = \begin{pmatrix} \nu_\ell \\ \\ \ell^- \end{pmatrix}_L$$

and a right handed weak isospin singlet

$$R = (\ell^-)_R \tag{1.3}$$

1.1.3 Electroweak Lagrangian

The electroweak Lagrangian $\mathscr{L}_{EW}$ is given as:

$$\mathscr{L}_{EW} = \mathscr{L}_{gauge} + \mathscr{L}_{fermi} + \mathscr{L}_{scalar} + \mathscr{L}_{Yukawa}. \tag{1.4}$$

The term $\mathscr{L}_{gauge}$ specifies the interactions between the gauge bosons (the trilinear and quartic gauge boson couplings) and is given as:

$$\mathscr{L}_{gauge} = -\frac{1}{4}F^{\ell}_{\mu\nu}F^{\ell\mu\nu} - \frac{1}{4}f_{\mu\nu}f^{\mu\nu}. \tag{1.5}$$

The interactions of the fermions with the gauge bosons $\mathscr{L}_{Fermi}$ is given as:

$$\bar{R}i\gamma^{\mu}(\partial_{\mu} + i\frac{g'}{2}B_{\mu}Y)R + \bar{L}i\gamma^{\mu}(\partial_{\mu} + i\frac{g'}{2}B_{\mu}Y + i\frac{g}{2}\sigma_{\ell}W_{\mu}^{\ell})L \tag{1.6}$$

where Y is the weak hyper-charge and σ_{ℓ} are the Pauli matrices.

The scalar term $\mathscr{L}_{scalar}$ specifies the interactions of the Higgs boson scalar ϕ:

$$\mathscr{L}_{scalar} = (D^{\mu}\phi)^{\dagger}(D_{\mu}\phi) - V(\phi^{\dagger}\phi) \tag{1.7}$$

where the potential V has the form

$$V(\phi^{\dagger}\phi) = \mu^2(\phi^{\dagger}\phi) + |\lambda|(\phi^{\dagger}\phi)^2 \tag{1.8}$$

and, D_{μ} is given as:

$$D_{\mu} = \partial_{\mu} + i\frac{g'}{2}B_{\mu}Y + i\frac{g}{2}\sigma_{\ell}W_{\mu}^{\ell}. \tag{1.9}$$

Lastly, the term $\mathscr{L}_{Yukawa}$, gives the coupling of the fermions to the scalar ϕ:

$$\mathscr{L}_{Yukawa} = -\zeta_i[\bar{R}(\phi^{\dagger}L) + (\bar{L}\phi^{\dagger}R)]. \tag{1.10}$$

Mass terms for a fermion field ψ in a Lagrangian appear in a form $m\psi^{\dagger}\psi$ where m is the mass of the fermion. The full Lagrangian $\mathscr{L}_{EW}$ defined in Eq. 1.4 – Eq. 1.10, however, has no terms which give mass to the fermions, the weak isospin W_{μ}^{ℓ} bosons, or the hyper charge B_{μ} boson. Mass terms for the fermions and EW bosons are acquired by breaking the symmetry of the $\mathrm{SU(2)_L \times U(1)_Y}$ group through the Higgs mechanism.

1.1.3.1 Spontaneous Symmetry Breaking

By requiring $\mu^2 < 0$ in Eq. 1.8 and solving for the potential being zero we get $\phi_0 = v/\sqrt{2}$. This breaks the $\mathrm{SU(2)_L \times U(1)_Y}$ symmetry but preserves $U(1)_{EM}$

symmetry. Expanding the Lagrangian $\mathscr{L}_{EW}$ about the vacuum state energy ϕ_0 the fermions acquire mass through the $\mathscr{L}_{Yukawa}$ term and the gauge bosons acquire mass through the $\mathscr{L}_{scalar}$. The $\mathscr{L}_{Yukawa}$ Lagrangian has terms of the form $\zeta\phi_0\psi^\dagger\psi = \zeta\frac{v}{\sqrt{2}}\psi^\dagger\psi$. The mass of a charged lepton ℓ is $M_\ell = \zeta\frac{v}{\sqrt{2}}$. Note that the Higgs mechanism does not tell us what the mass of the leptons will be. It only accounts for the terms that give mass. The mass of the leptons (or the couplings ζ) are inputs that must be measured.

Choosing the unitarity gauge and rearranging $\mathscr{L}_{scalar}$ to account for the vacuum energy state ϕ_0, we find new mass terms for the charged bosons $W^\pm_\mu$ and neutral bosons Z_μ and A_μ defined as linear combinations of the W^i_μ and B_μ bosons:

$$W^\pm = \frac{1}{\sqrt{2}}(W^1_\mu \pm i\, W^2_\mu) \tag{1.11}$$

$$Z_\mu = \cos\theta_W\, W^3_\mu - \sin\theta_W\, B_\mu \tag{1.12}$$

$$A_\mu = \sin\theta_W\, W^3_\mu + \cos\theta_W\, B_\mu \tag{1.13}$$

where θ_W is the Weinberg angle (or weak mixing angle). The mass term for the $W^\pm_\mu$ has value $M_W = \frac{gv}{2}$. With the relation $g' = g\tan\theta_W$ and Eq. 1.12 we find $M_Z^2 = M_W^2\cos^2\theta_W$. However, the A_μ boson (the photon) has no mass term as the $U(1)_{EM}$ symmetry is not broken. Unlike the fermions, we can predict the mass of the $W^\pm$ and Z bosons with fewer inputs (such as the weak mixing angle). This has been one of the great successes of the Standard Model. The Higgs mechanism requires the existence of an additional particle: the Higgs boson with mass $\sqrt{-2\mu^2}$. The Higgs boson has yet to be observed.

1.1.4 Z Boson Pair Production

Recall that the coupling of the fermions to the gauge bosons is described by the $\mathscr{L}_{Fermi}$ term in Eq. 1.4. After symmetry breaking the $\mathscr{L}_{Fermi}$ term can be written as the sum of three terms:

$$\mathscr{L}_{Fermi} = \mathscr{L}_{CC} + \mathscr{L}_{NC} + \mathscr{L}_{EM} \tag{1.14}$$

where $\mathscr{L}_{CC}$ represents the charged current interactions of the fermions to the $W\pm$ bosons, $\mathscr{L}_{NC}$ represents the neutral current interactions of the fermions to the Z boson, and $\mathscr{L}_{EM}$ represents couplings of the fermions to the photon. For this analysis we are only interested in couplings of the Z boson to the fermions.

The SM also allows for the self coupling of the gauge bosons through the $\mathscr{L}_{gauge}$ term in Eq. 1.4. This leads to trilinear gauge boson couplings of $WW(Z/\gamma)$ (where Z/γ means a Z boson or a photon) and quartic gauge bosons couplings of $WW(Z/\gamma)(Z/\gamma)$. However, the SM does not allow for neutral trilinear or quartic gauge boson couplings, for example $ZZ(Z/\gamma)$ or $ZZ(Z/\gamma)(Z/\gamma)$. Therefore, in the SM, Z boson pair production at tree-level is described by the $\mathscr{L}_{Fermi}$ term only.

The Z bosons decay essentially instantaneous (with a life time on order 10^{-25} s) into same flavor fermion anti-fermion pairs. For this analysis only the final states where both the Z bosons decay to charged leptons, excluding τ leptons, are studied. The three final states are: $\mu\mu\mu\mu$, $eeee$, and $\mu\mu ee$. The four lepton final states can cleanly reconstruct the four-momenta of each lepton. Additionally, the four lepton final states have small backgrounds.

At the Tevatron collider, 980 GeV protons collide with 980 GeV anti-protons

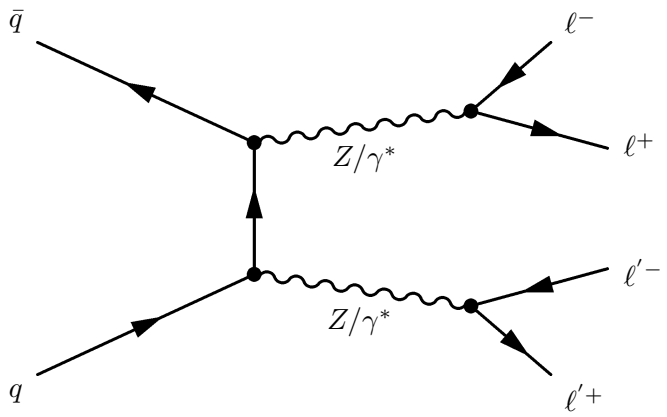

Figure 1.2: Feynman diagram for tree level the Standard Model process $q\bar{q} \rightarrow ZZ \rightarrow \ell^+\ell^-\ell'^+\ell'^-$

moving in the opposite direction (see Sec. 2.1). The proton is made up of three valence quarks, two up quarks and one down quark, and a sea of gluons. Z bosons do not couple to gluons directly; at the Tevatron Z bosons are produced primarily from quark anti-quark pairs from the proton and anti-proton. The tree-level Feynman diagram for Z boson pair production decaying into four leptons at the Tevatron is shown in Fig. 1.2. This is a t-channel diagram. There is no s-channel Z boson pair production because there are no neutral trilinear gauge boson couplings in the SM.

The cross section for $p\bar{p} \rightarrow ZZ$ at the Tevatron is 1.6 pb [2]. The cross section times branching ratio for all three channels is approximately 7 fb. For a total integrated luminosity of 1 fb^{-1} (the approximate data set for this analysis) the number of $p\bar{p} \rightarrow ZZ$ decaying into $\mu\mu\mu\mu$, $eeee$, or $\mu\mu ee$ is 7 events; however, after factoring in the acceptance of the detector the expected observed yield is only one or two events.

1.2 Monte Carlo Expectations

Due to the fact that the expected event yield is so small, it is difficult to study the properties of Z boson pair production from data. Additionally, because of the selection properties on the data sample, such as kinematic cuts, the events selected are biased to a restricted region of phase space. However, assuming we trust the theory, we can study Z boson pair production from a Monte Carlo event generator.

The SM Monte Carlo event generator PYTHIA [21] is used to study $p\bar{p} \rightarrow ZZ \rightarrow \mu\mu\mu\mu$. Only one channel is studied because to the most part at generator level the distributions of the other channels are identical. Comparisons before and after kinematic cuts are done to compare the full phase space and the restricted phase space; when kinematic cuts are applied they are done to emulate the data selection (lepton $p_T > 15$ GeV and $M_{\ell\ell} > 30$ GeV).

Figure 1.3 shows the di–muon invariant mass of one Z boson versus the di–muon invariant mass of the other Z boson in $p\bar{p} \rightarrow ZZ \rightarrow \mu\mu\mu\mu$ production where the invariant mass is determined from the final state muons. PYTHIA was required to have $M_Z > 4.2$ GeV and lepton $p_T > 0$ GeV. There are four corners of high intensity at roughly (4 GeV,4 GeV), (91 GeV,4 GeV), (4 GeV,91 GeV), and (91 GeV,91 GeV). These correspond to contributions from $\gamma^*\gamma^*$, $Z\gamma^*$, and ZZ events. The small number of events below 4.2 GeV originates from final state photon radiation because the invariant mass cut in PYTHIA is done on M_Z and not on $M_{\mu\mu}$. After requiring lepton $p_T > 15$ GeV and $M_{\mu\mu} > 30$ GeV (see Sec. 1.2.1 as to why some events have $M_{\mu\mu} < 30$ GeV) Fig. 1.3 reduces to Fig. 1.4. Note that again mostly only ZZ events

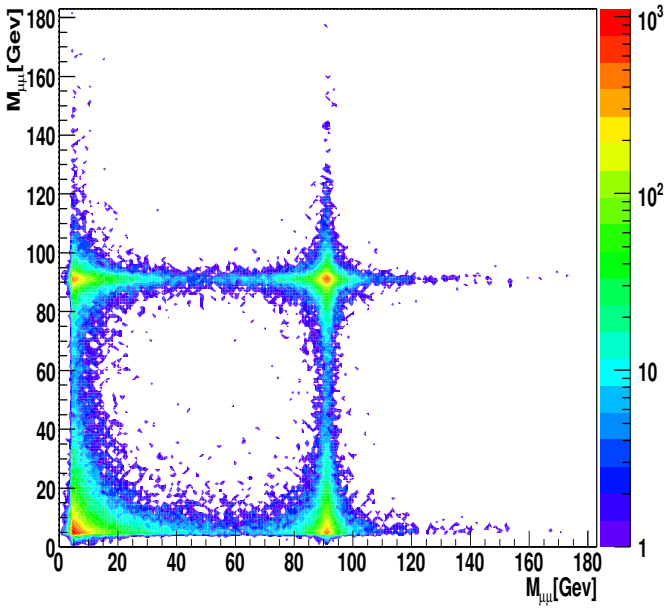

Figure 1.3: $M_{\mu\mu}$ of one Z boson versus $M_{\mu\mu}$ of the other Z boson for $M_Z > 4.2$ GeV before lepton p_T cuts. The color intensity represents the number of events per square invariant mass bin.

remain with a small tails from $Z\gamma^*$.

In addition to the invariant mass of the Z bosons there is the invariant mass of the Z boson pair system from the four final state leptons. Figure 1.5 shows the four-lepton invariant mass of the Z boson pair system. There are three significant peaks from $\gamma^*\gamma^*$, $Z\gamma^*$ and ZZ. After requiring $p_T > 15$ GeV on the leptons and $M_{\ell\ell} > 30$ GeV the four-lepton mass of the Z boson pair system is shown in Figure 1.6. Note that mostly only ZZ events remain.

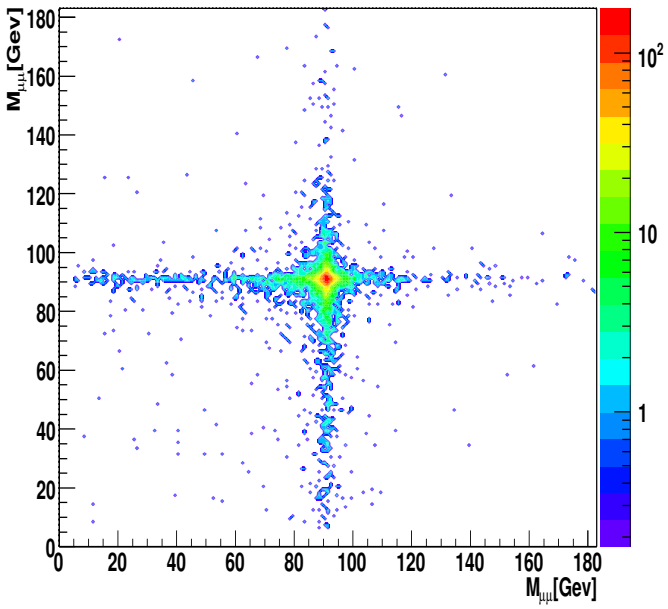

Figure 1.4: $M_{\mu\mu}$ of one Z boson versus $M_{\mu\mu}$ the other Z boson for $M_{\mu\mu} > 30$ GeV and lepton $p_T > 15$ GeV. The color intensity represents the number of events per square invariant mass bin.

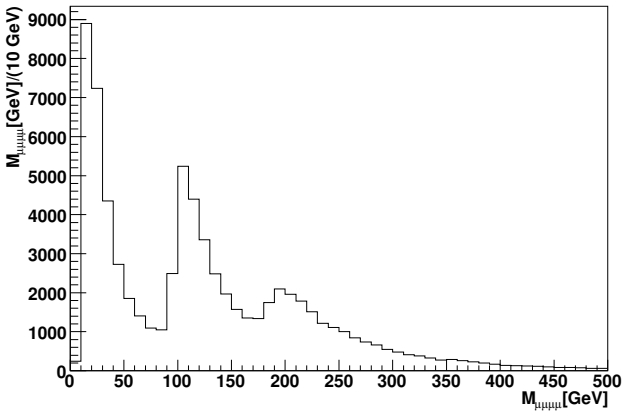

Figure 1.5: Four lepton invariant mass $M_{\mu\mu\mu\mu}$ of the Z boson pair system before lepton p_T cuts.

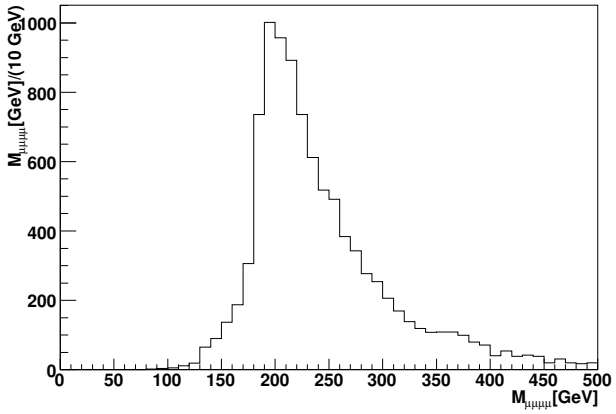

Figure 1.6: Four lepton invariant mass $M_{\mu\mu\mu\mu}$ of the Z boson pair system for $M_{\mu\mu} > 30$ GeV and lepton $p_T > 15$ GeV.

1.2.1 Lepton Pairing Combinatorics

In the channels $\mu\mu\mu\mu$ and $eeee$, where both Z bosons decay to the same lepton generation, there is an issue with not being able to distinguish identical flavor leptons. This affects the invariant mass distribution in these channels. Figure 1.7 shows the invariant mass of Z boson events for the correct invariant mass pairs (dashed red line), the false invariant mass pairs (doted blue line), and the combined invariant mass pairs (solid black line). The correct invariant mass pair is the invariant mass pair from the leptons from the Z bosons. The false invariant mass pair is the invariant mass from the leptons that had opposite charge but did not come from the same Z boson. Note that most of the time the false invariant mass pair passes the invariant mass cut of 30 GeV. The combined invariant mass is the invariant mass distribution that would be measured (ignoring detector resolution effects) in these channels if many events were found. Note also that in Fig. 1.4 some events

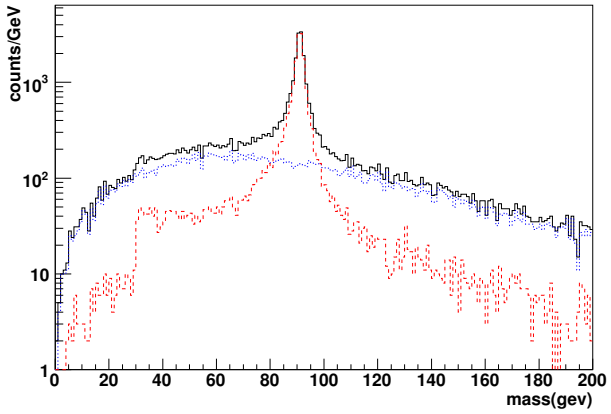

Figure 1.7: $M_{\mu\mu}$ of Z boson events for the correct invariant mass pairs (dashed red line), the false invariant mass pairs (dotted blue line), and the combined invariant mass pairs (solid black line)

remain with invariant mass below the 30 GeV invariant mass cut. This is because only at least one Z boson pair candidate is required to pass the 30 GeV invariant mass cut. Sometimes the false invariant mass pairs pass the invariant mass cut when the real invariant mass pairs fail. In data, it is impossible to know for certain which invariant mass pairs originate from each Z boson.

1.2.2 Single Z Boson and Z Boson Pair Production Comparisons

Some distributions in Z boson pair production diverge significantly from those in single Z boson production ($p\bar{p} \rightarrow Z/\gamma^* \rightarrow \ell^+\ell^-$). A few of the most important differences are the boson p_T, $\Delta\phi$, and R between the leptons. The quantity R is defined as

$$R = \sqrt{\Delta\phi^2 + \Delta\eta^2} \tag{1.15}$$

where $\Delta\phi$ and $\Delta\eta$ are the difference in ϕ (the azimuthal angle) and η (the pseudo-rapidity - see Appendix A) of each lepton.

All comparisons between Z boson pair production and single Z boson production are done for lepton $p_T > 15$ GeV and $M_{\ell\ell} > 30$ GeV.

Figure 1.8 shows the boson p_T from single Z boson production and Z boson pair production. Note that the boson p_T of $Z \to \mu\mu$ events peaks at less than 5 GeV and falls rapidly and that the boson p_T of $Z \to \mu\mu\mu\mu$ events peaks closer to 30 GeV and is much broader with a long tail. The boson p_T in inclusive Z boson production arises primarily through next to leading order initial state gluon radiation, however, for Z boson pair production the boson p_T arises primarily from the leading order recoil of one Z boson off the other Z boson. If any Z boson events are found in data, a large boson p_T is expected.

Figure 1.9 and Fig. 1.10 show the $\Delta\phi$ and R between the leptons that came from a Z boson in Z boson pair production (solid black line), between the leptons from the Z boson in single Z boson production (dashed red line), and between the leptons that had the smallest $\Delta\phi$ and R for all lepton pairs in Z boson pair production. Note that the leptons from the Z bosons in Z boson pair production are not as back-to-back in ϕ as for single Z boson production. This is related to the large boson p_T for the Z bosons in Z boson pair production. Additionally, note that the smallest separation for the leptons in Z boson pair production shows that the leptons can often overlap. The fact that leptons overlap much more in Z boson pair production can have a large effect on both the acceptance and efficiency for detection in the $\mu\mu\mu\mu$ and $eeee$ channels. Isolation cuts for muons and electrons often require

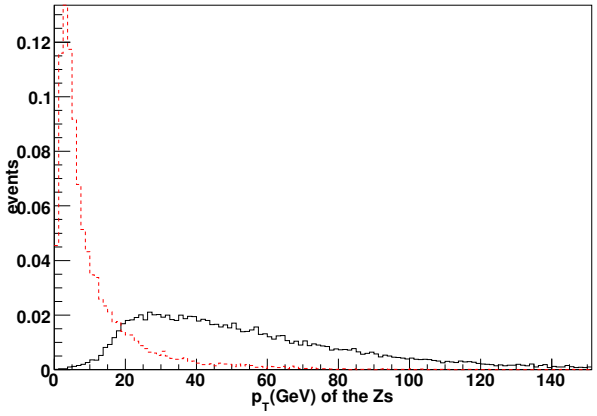

Figure 1.8: p_T of each Z boson in Z boson pair production (solid black line) and for the single Z boson production (dashed red line).

the leptons to be spatially separated in R. For single Z boson production this does not have much effect on the kinematic acceptance because the leptons rarely overlap and an isolation cut only really affects the efficiency. For Z boson production the leptons can often overlap and so both the kinematic acceptance and the lepton identification efficiencies are affected. Care should therefore be taken with cuts that require separation between leptons (which includes low invariant mass cuts).

The p_T distribution of all the leptons for Z boson pair production and single Z boson production is shown in Fig. 1.11. Note that the lepton p_T in Z boson pair production does not have the sharp peak near 45 GeV that single Z boson production does, additionally Z pair production has a long high p_T tail compared to single Z boson production.

The η distribution of all the leptons for Z boson pair production and single Z boson production is shown in Fig. 1.12. Note that the lepton η in Z boson pair

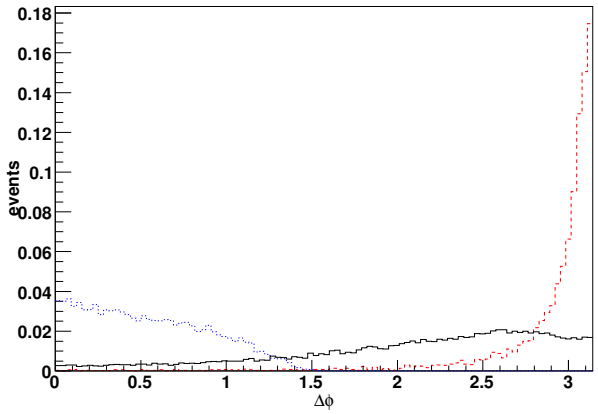

Figure 1.9: $\Delta\phi$ between the leptons from each Z boson in Z boson pair production (solid black line), between the leptons from the Z boson in single Z boson production (dashed red line), and between the leptons with the smallest $\Delta\phi$ in Z boson pair (doted blue line).

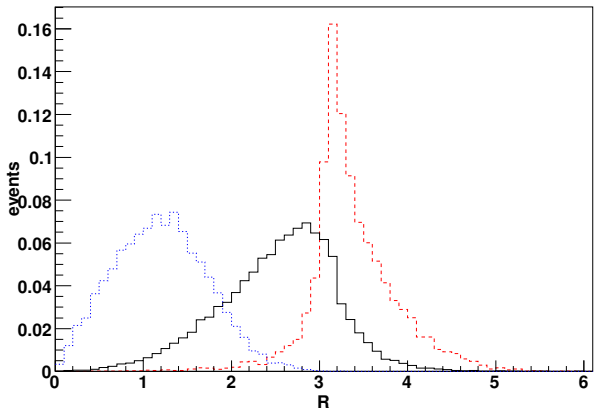

Figure 1.10: R from the leptons from each Z boson in Z boson pair production (solid black line), between the leptons from the Z boson in single Z boson production (dashed red line), and between the leptons with the smallest R in Z boson pair production (doted blue line).

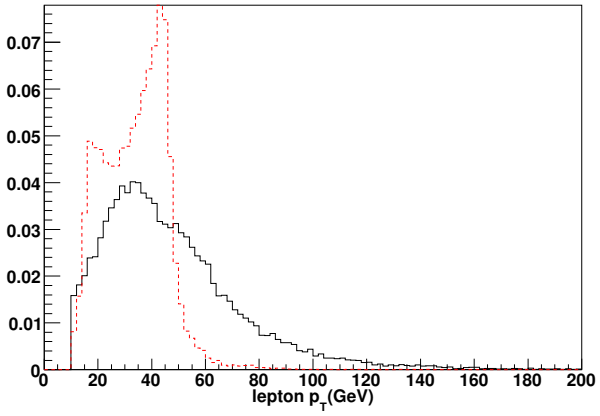

Figure 1.11: p_T of all the leptons for Z boson pair production (solid black line) and single Z boson (dashed red line) production.

production is more central than the lepton η in single Z boson production.

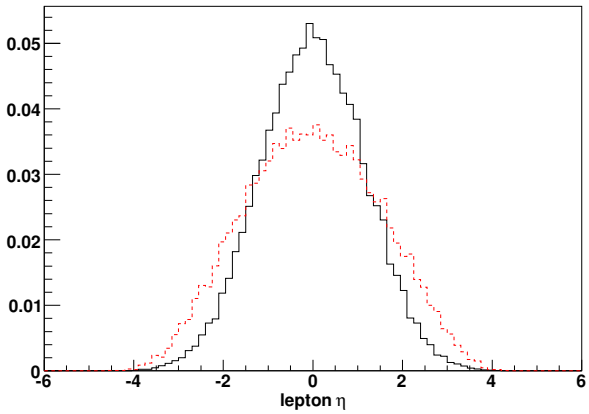

Figure 1.12: η of all the leptons for Z boson pair production (solid black line) and single Z boson (dashed red line) production.

Chapter 2

Apparatus

2.1 The Accelerator System

This chapter describes the Fermi National Accelerator Laboratory (Fermilab) Tevatron collider as well as the DØ detector for the period of time known as Run IIa. The Fermilab Tevatron currently produces the highest energy collisions of any accelerator in the world. Protons and anti-protons are accelerated to energies of 980 GeV and collide head on for a total production energy of 1960 GeV. This is accomplished through a chain of many different accelerator components. In this chapter, however, we only discuss the Tevatron. A description of the other components in the accelerator chain before the Tevatron can be found in Appendix B.

2.1.1 Tevatron

The Tevatron is the sixth and final synchrotron in the accelerator chain. Its circumference is 6.28 kilometers. It is made of over 1000 superconducting quadrupole and dipole magnets. The dipole magnets can provide a magnetic field of 4.2 Tesla. Each superconducting magnet contains over 42,000 miles of wire. The superconducting magnets wires are made of NbTi (Niobium Titanium) and must be cooled to 4.6 Kelvin. The magnets are cooled with liquid helium. Currently, the Tevatron cryogenic cooling system is the largest cryogenic system in the world. The cooling

system consists of many helium compressors, helium and nitrogen storage tanks, and a moat of water which surrounds the accelerator to provide a heat sink for the cooling.

When enough anti-protons have been accumulated, the Main Injector (see Appendix B) loads first protons and then anti-protons into the Tevatron. The protons move clock-wise around the ring and the anti-protons counterclockwise. Each beam in the Tevatron moves in a helix around the other (forming a double helix). This allows the beams to share the same beam pipe and magnets without colliding into one other. Once the Tevatron is loaded with both beams, the beams are accelerated to 980 GeV.

The beam is then subjected to a number of quality controls to improve its properties. For example the beam is usually surrounded by a halo of particles not directly in the main beam. By squeezing the beam with collimators the halo can be reduced. Once the beams are stable, low-beta quadrupole magnets are used to focus the beams for collisions at the point B0 where the CDF detector resides and at point D0 (See Fig. B.1) where the DØ detector resides.

2.1.2 Timing and Beam Structure

The Main Injector loads the Tevatron with 36 bunches of protons and 36 bunches of anti-protons. The 36 bunches are not uniformly distributed in the Tevatron, instead they are grouped into three super-bunches, with 12 bunches in each super bunch. The time between each bunch in a super-bunch is 396 ns. The time

between each super-bunches is 2.65 μs. Figure 2.1 shows a drawing of the timing of the bunches. It takes approximately 21 μs for a proton or anti-proton to complete one revolution around the Tevatron ring.

The period of time from the first collisions until collisions are stopped is called the store. As the store progresses the beam becomes less focused and the luminosity diminishes. During a store, more anti-protons are being stacked and stashed in the Accumulator and Recycler. It takes over 12 hours to produce enough anti-protons for the next store.

The rate at which interactions happen is measured with a quantity called the instantaneous luminosity. This quantity is given in $\mathrm{cm}^{-2}\,\mathrm{s}^{-1}$. A typical instantaneous luminosity is of order $10^{31}\,\mathrm{cm}^{-2}\,\mathrm{s}^{-1}$. A store can last for over 30 hours, at which time, assuming no unexpected anti-protons losses there should be enough anti-protons available for the next store. The luminosity integrated over time is defined as the integrated luminosity. Currently, the Tevatron has delivered more than 3 fb^{-1} of data. The integrated luminosity of the Tevatron as a function of time can be seen in Fig. 2.2.

One might ask why a proton on anti-proton colliding beam accelerator was chosen over a proton on proton colliding beam accelerator. One answer is economics. The same magnets that direct and focus protons can be used to direct and focus anti-protons which move in the opposite direction. A proton on proton accelerator requires twice as many quadrupole and dipole magnetics as a proton on anti-proton accelerator. Another reason for using anti-proton is that the cross sections for some processes are greater for proton anti-proton collisions than for proton on proton

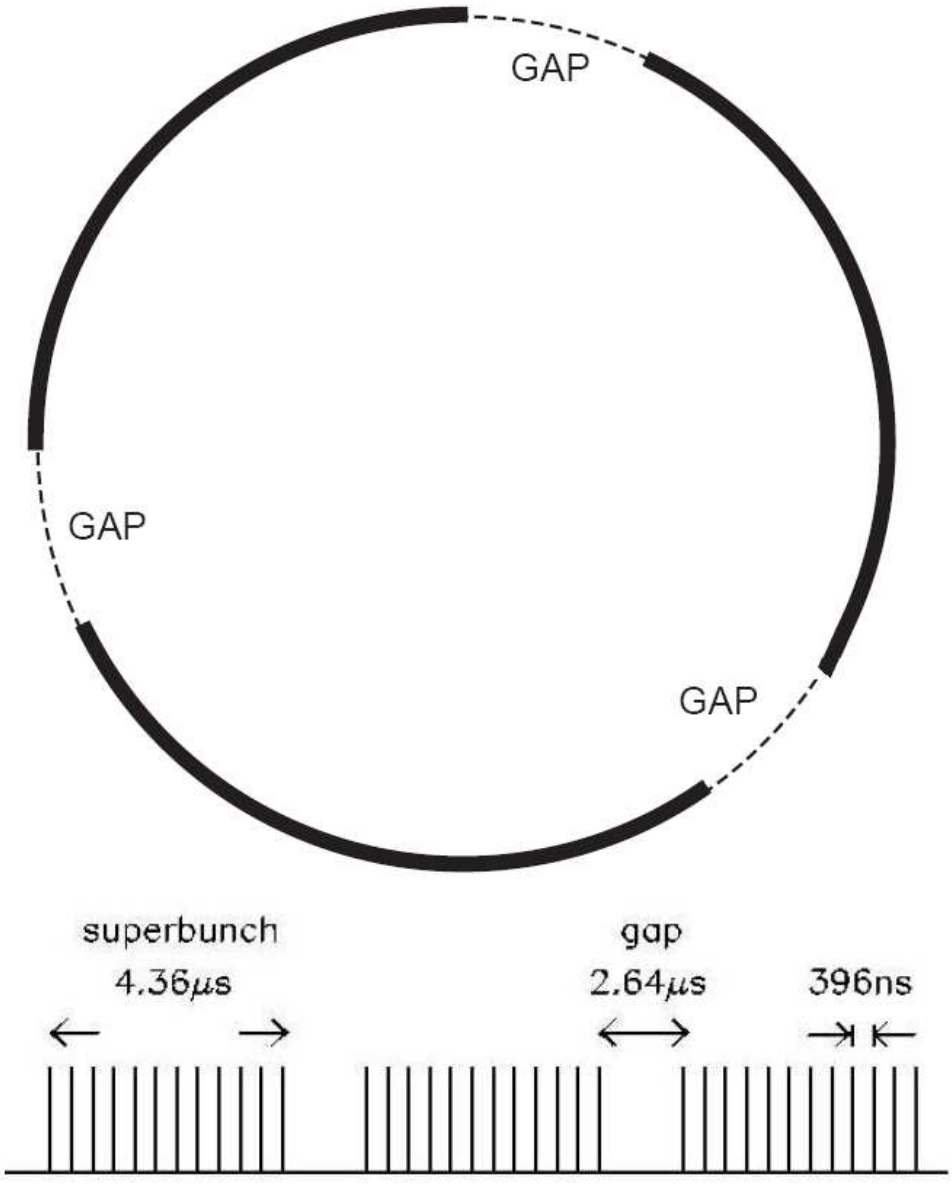

Figure 2.1: Timing of the bunches in the Tevatron. There are 36 bunches for each beam, 12 Bunches in a super-bunch, and three super-bunches per beam. The Circle represents the Tevatron, the dark solid lines represent a super bunch.

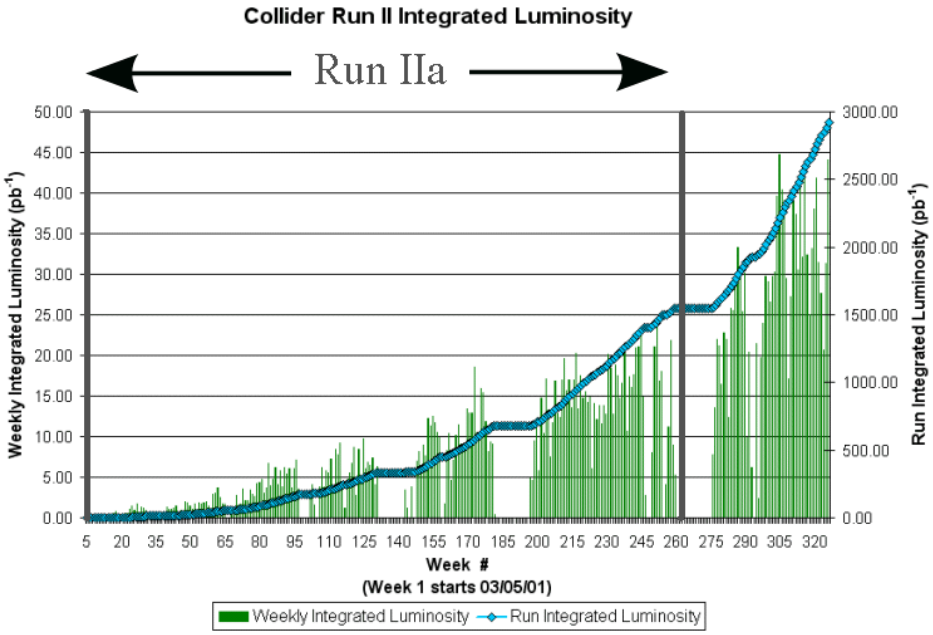

Figure 2.2: Total integrated luminosity up until June 2007. Run IIa is the period of time for which the data of this analysis was collected.

collisions.

2.2 Definitions and Conventions

Here we discuss some common conventions and useful definitions. Unless otherwise stated, the following conventions and notation will be assumed through the rest of the text. All quantities which involve the speed of light c are normalized such that $c = 1$.

2.2.1 The DØ Coordinate System

The direction of the proton is defined as the positive z direction (recall that protons move clockwise around the ring), positive x points away from the center of the Tevatron ring, and the positive y direction points up. This defines a right-handed rectangular coordinate system as can be seen in Fig. 2.3. The origin is defined to be $(x, y, z) = (0, 0, 0)$. This defines our basis, however, it is often more

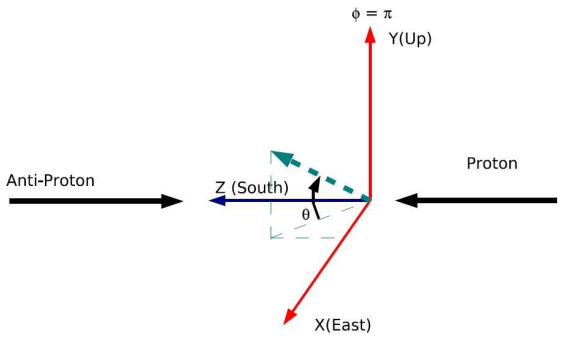

Figure 2.3: Rectangular coordinate system used at DØ

convenient to work in a modified spherical coordinate system using the azimuthal

angle ϕ and pseudorapidity η (see Appendix A for a definition of η). This coordinate system is especially useful for objects defined in the calorimeters. In the muon detectors, which have rectangular symmetry, a rectangular or cylinder coordinate system is sometimes more convenient. In each coordinate system, the variable r is the magnitude of a point with respect to the origin, an invariant quantity. In rectangular coordinates $r = \sqrt{x^2 + y^2 + z^2}$.

The momentum of elastic or inelastic scattering which goes down the beam pipe is not measured, therefore it is difficult to determine the total longitudinal component of momentum after a collision. The total transverse component of momentum before collision is negligibly small. We can require that the total transverse component of momentum of a system be zero before and after collision. We therefore define the following quantity:

$$p_T = p \sin\theta = p_x^2 + p_y^2. \tag{2.1}$$

We determine p_z from p_T using the relation $p_T/p_z = \tan\theta$, solving for p_z in terms of η we get:

$$p_z = p_T \sinh\eta \tag{2.2}$$

$$p_x = p_T \cos\phi \tag{2.3}$$

$$p_y = p_T \sin\phi \tag{2.4}$$

The total momentum can then be written as:

$$p^2 = p_x^2 + p_y^2 + p_z^2 = p_T^2 + p_z^2 = p_T^2(1 + \sinh^2\eta) \tag{2.5}$$

Knowing η, ϕ, p_T, and E of a particle, we can determine its momentum four-vector.

Sometimes it is useful to use the transverse component of energy E_T defined as:

$$E_T = E \sin\theta. \tag{2.6}$$

This may seem a bit confusing because energy is a scalar and therefore has no components. Most high p_T final state particles such as muons and electrons in a hard scatter are moving relativistically, therefore their magnitude of momentum and energy are the same ($E = |\,\mathbf{p}\,|$). If we measure the momentum of a particle (in the tracking detectors) and the energy (in the calorimeters) they should be equal. However, instead of p we measure p_T, therefore, instead of comparing E with p, we compare E_T to p_T. This can be useful for discriminating between particle types and interactions.

Another important definition that is often employed is:

$$\Delta R = \sqrt{(\eta_i - \eta_j)^2 - (\phi_i - \phi_j)^2}. \tag{2.7}$$

This is used to describe the separation between two objects in the detector with coordinates (η_i, ϕ_i) and (η_j, ϕ_j). The variable ΔR is Lorentz invariant (recall that differences in rapidity are Lorentz invariant). With the variable ΔR we can discuss the separation between objects without worrying about which frame of reference we are in.

Proton and anti-proton bunches have widths. For this reason the interaction point has a spread z (of roughly 25 cm.) Therefore it can be useful to distinguish between physics-η and detector-η. Physics η represents the η of a particle from its production point and detector-η represents the eta of a particle from the origin

(0,0,0) to some point at each sub-detector. We will use η to denote physics η and η_D to denote detector η. The definitions of η_D for each sub-detector are described in Sec. 3.2 and Sec. 3.4. The interaction point in r, has a small width (of order of 0.1 cm) and therefore detector ϕ and physics ϕ are essentially identical.

2.3 DØ Detector

The DØ is a multipurpose detector with various detector components designed to identify long lived particles such as electrons, photons, muons and hadronic jets which are made mostly of pions and kaons. Short lived particles such as B mesons and tau lepton decays can be identified from their decay vertices and products. All prompt decays such as the Z boson decays must be inferred from their decay products.

The detector is quite large; the entire assembly is about 13 m high $\times$ 11 m wide $\times$ 17 m long with a total weight of about 5500 tons (of which the toroid magnets account for 65%). The main components of the DØ detector are listed as follows:

- Tracking system - solenoid, inner silicon tracker, outer fiber tracker
- Preshower detectors - central and forward
- Calorimeters and Inner Cryostat Detectors
- Muon detectors - central, forward, toroid magnet
- Trigger system - Level-1, Level-2, Level-3
- Luminosity system

Electrons, photons, and hadronic particles are identified with the calorimeters. Muons which penetrate the calorimeters (and the toroid magnets) without depositing significant energy (at Tevatron energies) are detected with the muon detector beyond the calorimeter. A superconducting two Tesla solenoid magnet is used to bend the path of charged particles from which the p_T of the particles can be inferred. A 2D cross section of the DØ detector can be seen in Fig. 2.4.

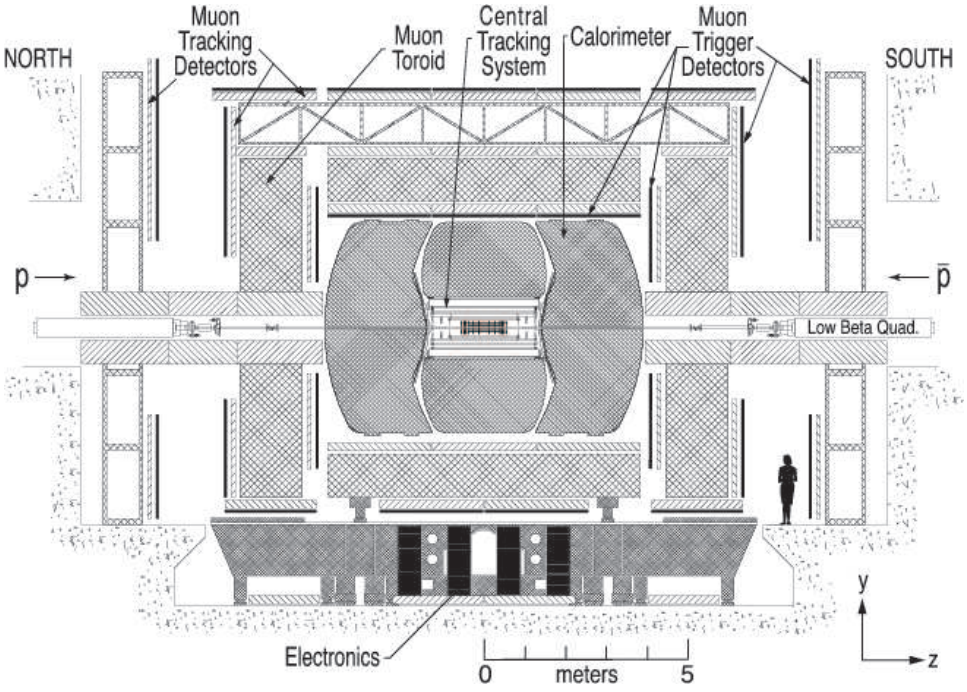

Figure 2.4: Side-view Drawing of the DØ detector.

The DØ detector resides at point DØ along the Tevatron ring. The beam sits in a lower corner of the tunnel. This description of the DØ detector applies to the period of time known as Run IIa for which this analysis was done. Since Run IIa ended in 2006 and Run IIb began some hardware upgrades have been done for the tracking system and preshower electronics. These upgrades do note apply to this

analysis and therefore are not discussed.

2.3.1 Tracking System

The DØ tracking system is made up of three primary components: a 2 T solenoid magnet which generates a magnetic field along the beam axis, a finely segmented inner tracking detector called the Silicon Microstrip Tracker (SMT), and a more coarsely segmented outer tracking detector called the Central Fiber Tracker (CFT). A cross section drawing of the DØ tracking system can be seen in Fig. 2.5.

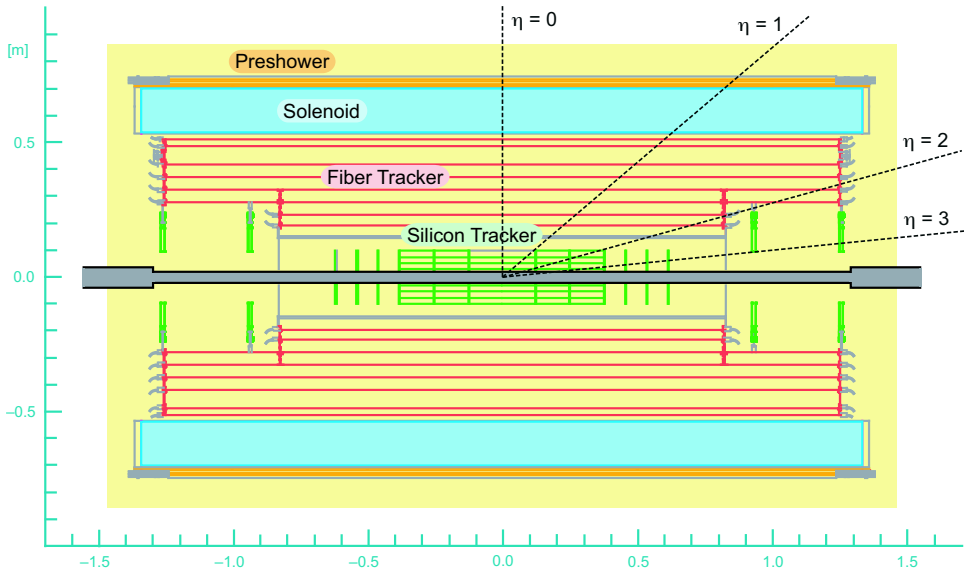

Figure 2.5: Cross sectional view of the tracking system.

The tracking system helps with particle identification. For example a charged particle such as a muon or an electron should leave a track in the tracking system, whereas, a photon which has no charge does not. Additionally, jets made mostly of many pions will be associated with many tracks. Another important use of the tracking system is to measure the momentum of a charged particle. The curvature R

of charged particle with charge q and a component of momentum p_T perpendicular to a magnet field is given as

$$R = \frac{p_T}{qB}. \tag{2.8}$$

With the tracking system the curvature of a charged particle can be determined from which the p_T/q of a particle can be inferred.

2.3.1.1 Superconducting Solenoid

Solenoid is 2.8 m in length, 1.42 m in diameter, with a mean thickness of 60 cm. The solenoid plus cryostat adds about one radiation length of material. The magnet windings are made of niobium-titanium superconducting wire and are encased in an aluminum cylinder. The magnet is chilled to 4.2 Kelvin with liquid helium.

2.3.1.2 Silicon Microstrip Tracker

The SMT detector [5] is the first detector encountered by particles from collisions. It uses both single and double sided silicon microstrip detectors with over 793,000 cells. The expected hit resolution in $r\phi$ in 10 μm.

The SMT inner tracker consists of six 12 cm long barrels along the beam axis with interspersed perpendicular disks (12 F-disks and 4 H-disks). In general, the barrels are used to identify particles with small η and the disks for particles with large η. A drawing of the SMT can be seen in Fig. 2.6. Each barrel has four readout layers. The readout layers are divided into two sublayers. Figure 2.7 shows the

drawing of the barrel layers and sublayers. The F-disks contain 12 double sided silicon microstrip detectors. The H-disks use 24 single sided microstrip detectors, 12 on each side of the disk. The F-disks are located at $|z|$ =12.5, 25.3, 38.2, 43.1, 48.1, and 53.1 cm. The barrels end at $|z| = 38.1$ cm and are capped off by an F-disk. The H-disks are located at $|z| = 100.4$ and 121.0 cm.

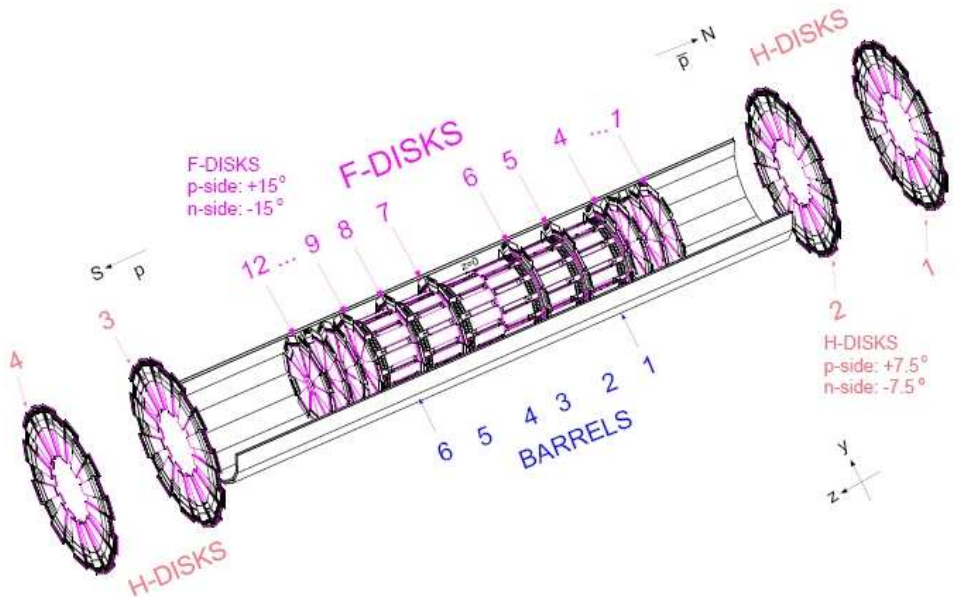

Figure 2.6: Drawing of the six barrels, 12 F-disks, and 4 H-disks of the SMT detector.

2.3.1.3 Central Fiber Tracker

Surrounding the SMT is the Central Fiber Tracker [6]. The CFT uses 76,800 scintillating fibers mounted on eight barrels of increasing radius ranging from 20 cm to 52 cm from the beam pipe. The CFT can detect tracks up to an $|\eta|$ of about two. Each barrel contains four layers of fibers: doublet axial layers and doublet stereo layers. The doublet axial layers, also know as the x layers, measure ϕ. The doublet

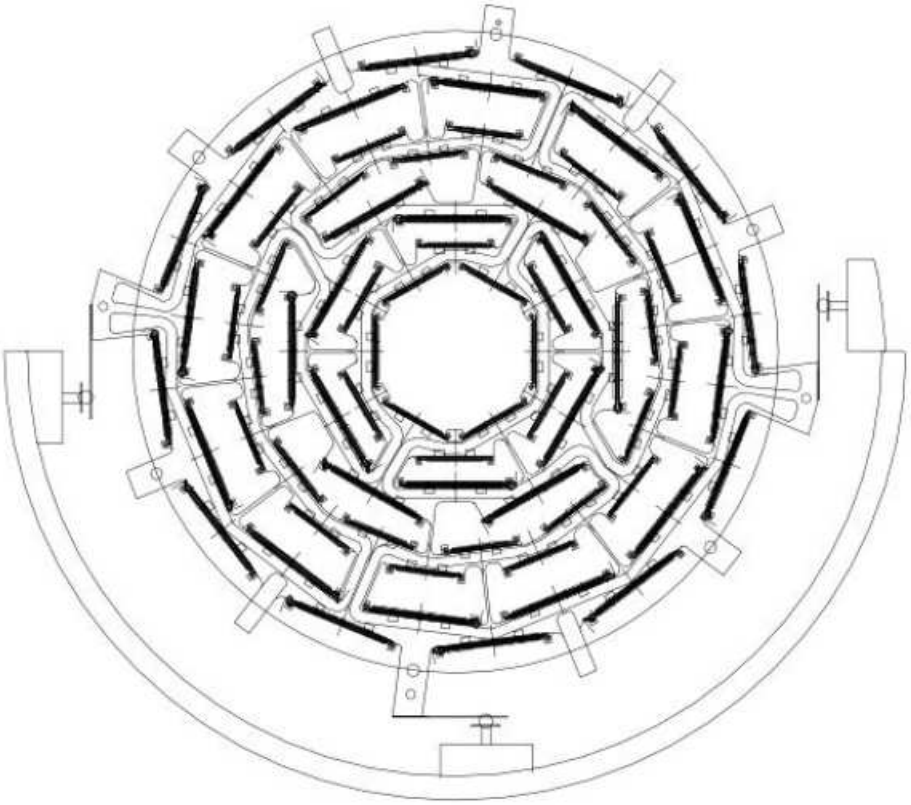

Figure 2.7: Cross section of the SMT barrels.

stereo layers, also known as the u and v layers, are tilted $+3°$ and $-3°$ to the beam axis and are used to measure η. Fig. 2.8 shows a cross sectional drawing of the CFT highlighting the doublet stereo and axial layers. The fibers are 835 microns thick. Each layer has a resolution on the order of 100 microns.

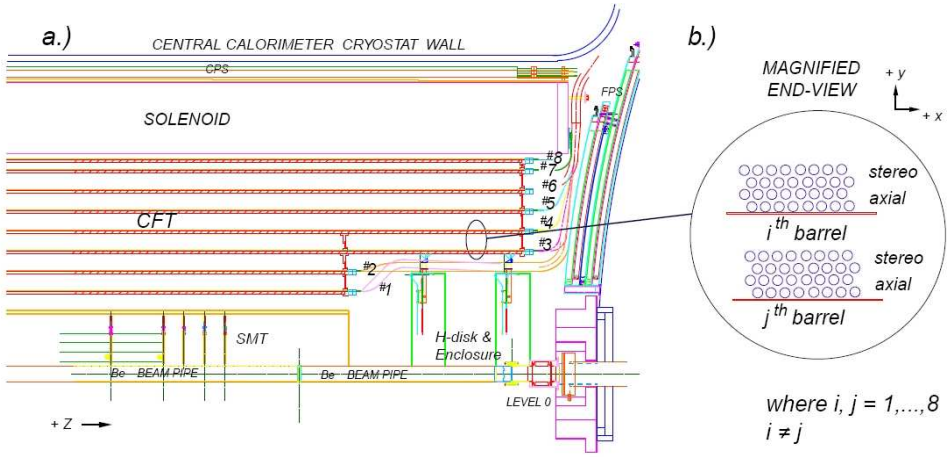

Figure 2.8: (a) Quarter $r-z$ view of the CFT showing the 8 barrels. (b) Magnified $r-\phi$ view of the double axial and stereo layers for two different barrels.

Ionizing particles that pass through a fiber produce on average 10 photons. The photons are then detected with a Visible Light Photon Counter (VLPC) which coverts the light into an electrical signal.

2.3.2 Preshower Detectors

The last detectors before the calorimeters are the preshower detectors: the central preshower (CPS) detector covering $|\eta| < 1.3$ and the forward preshower (FPS) detector covering $1.1 < |\eta| < 2.5$. The preshower detectors are designed to assist the tracker by providing precise position measurements and to assist the calorimeter by

early energy sampling of the shower. Additionally, the preshower detectors provide discriminating power to help distinguish electrons and photons from muons and pions. In practice, due to poor design of the electronics, the preshower detectors are effectively useless at measuring energy (at least for Run IIa); however, they are still useful for position measurements and discrimination. The preshower detectors are not used in this analysis. A detailed description of the preshower detector can be found in Appendix C.

2.3.3 Calorimeters

After the preshower detectors are the DØ calorimeters [10]. The calorimeters are designed to measure the energy of electrons, photons, and hadronic jets. Layers of dense material are used to sample EM and hadronic shower at many points to determine an energy profile.

Electrons and photons interact with matter by pair production ($\gamma \rightarrow e^+e^-$) and bremsstrahlung ($e \rightarrow e\gamma$). Each new electron or photon interacts in the same way, creating a cascade of particles called a shower until the total mean energy per particle falls below a threshold. The effective energy loss of an electron or photon, as a function of depth x, moving through matter is:

$$E(x) = E_0 e^{-x/X_0} \tag{2.9}$$

where E_0 is the originating particles starting energy and X_0 is the radiation length of the material from which the shower develops. For a dense material such as Uranium X_0 is 3.2 mm.

Hadronic particles such as pions and kaons interact with matter primarily through the strong nuclear force. These interactions produce pions, both charged (π^+, π^-) and neutral (π^0). The neutral pions decay promptly to photons which produce an EM shower . The charged pions continue producing more pions. A hadronic shower is a combination of a hadronic cascade and a EM cascade and develops over longer and wider distance than a purely EM shower. The effective energy loss of a hadronic particle moving through matter is characterize by absorption lengths λ_0. Uranium has a absorption length of 10.5 cm. Clearly more material is needed to contain a hadronic shower than a EM shower.

The DØ experiment consists of three calorimeters, one central calorimeter (CC) covering $|\eta| < 1.1$, and two end cap calorimeter (EC) covering $1.4 < |\eta| < 4.2$. Each calorimeter is contained inside a cryostat and maintained at temperature of 90 Kelvin. The region $1.1 < |\eta| < 1.4$ is called the inner cryostat region (ICR).

The fundamental unit of the calorimeter is the di-gap. A di-gap is a read out board sandwiched in between two absorbing plates (usually uranium) with liquid argon between the gaps; each di-gap is effectively a capacitor. An electric field is maintained between the metal absorbing plates and the signal boards by attaching a 2 kV source to the signal boards and grounding the absorbing plates. A schematic drawing of a di-gap of the calorimeters is shown in Fig 2.9. The charged particles in the shower (electrons or pions) produce ions which move in the liquid argon under the influence of the electric field and accumulate on the signal board. The maximum drift time from the absorber to the signal board is 450 ns.

The calorimeter is built in several layers. The first four layers are called the

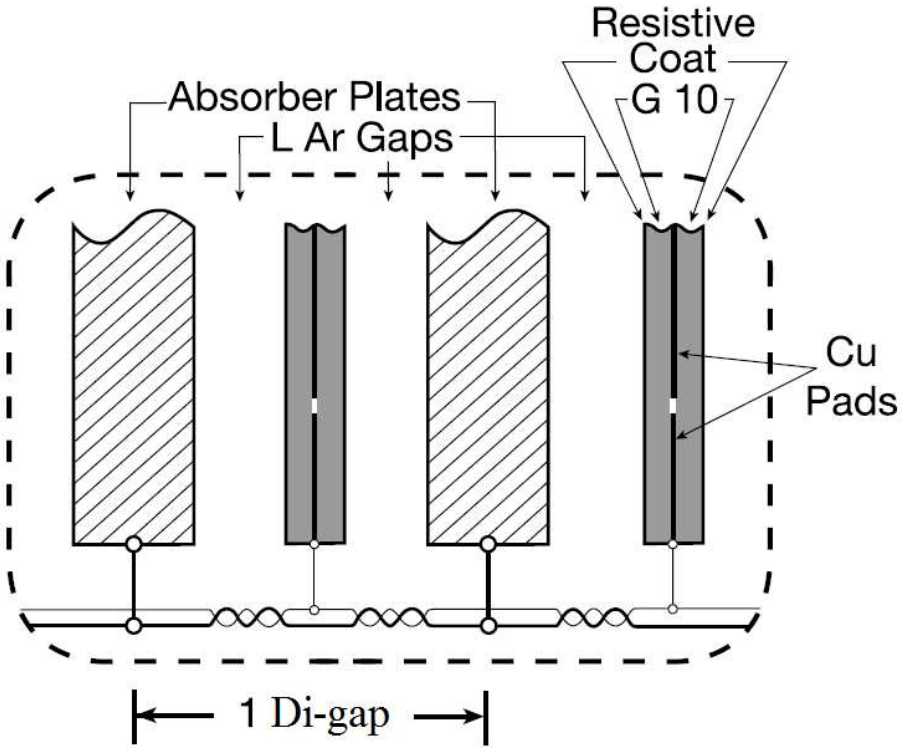

Figure 2.9: Cartoon of a calorimeter di-gap.

EM layers, the next three layers are called the fine hadronic (FH) layers, and the last layer is called the coarse hadronic (CH) layer.

Each layer is subdivided into cells[1] with 0.1×0.1 ($\Delta\eta \times \Delta\phi$) segmentation. The one exception is third EM layer, this layer has 0.05×0.05 segmentation. This is suppose to correspond to the maximum of an EM shower. This was true in Run I, however, in Run II due to the solenoid and lead layer the peak is shifted between the 2nd and 3rd EM layer [13]. Figure 2.10 shows a cross sectional view of one quarter of the detector showing the cells dimensions in η and r. A more abstract drawing of the cell distribution, clearly labeling each layer, but not showing the correct depth r, can be seen in Fig. 2.11. Each cell has multiple depths of di-gaps. For example a cell in the first EM layer has two depths of di-gaps (meaning three layers of absorbing plates, two signal boards, and two argon gaps) and a cell in the first hadronic layer has 20 depths of di-gap. Each cell , however, only has one output (called a read out channel). In other words each cell is effectively one capacitor made from 2-20 di-gaps. All the layers in one 0.1×0.1 projection are called a tower. In total there are on the order of 50,000 cells and 5,000 towers.

The Central Calorimeter is built in ϕ-modules. For the EM layers there are 32 modules subtending $2\pi/32 \approx 0.2$ radiants, two towers width in ϕ. For the FH and CH layers there are 16 modules. The boundary of these modules, called the ϕ module cracks, are dead regions. The energy of a particle which moves between the module cracks is less well measured. The EM layers of the endcap calorimeters are not built in ϕ-modules and do not have these dead regions.

[1]Di-gaps are often also called cells in the literature which can be a source of confusion

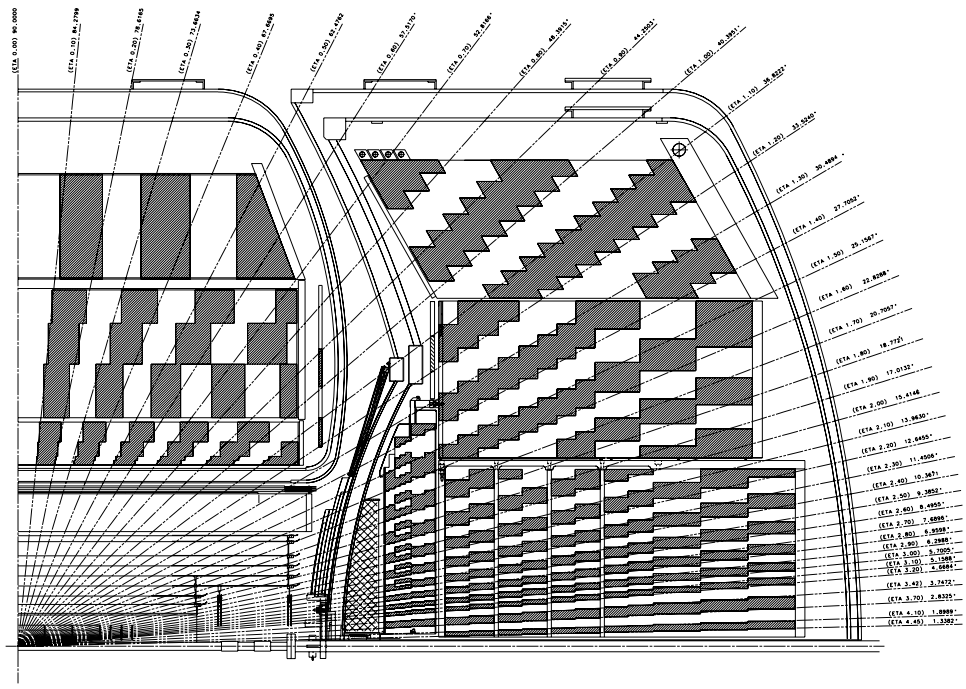

Figure 2.10: One quarter of the detector highlighting the transverse η and longitudinal segmentation of the calorimeter cells.

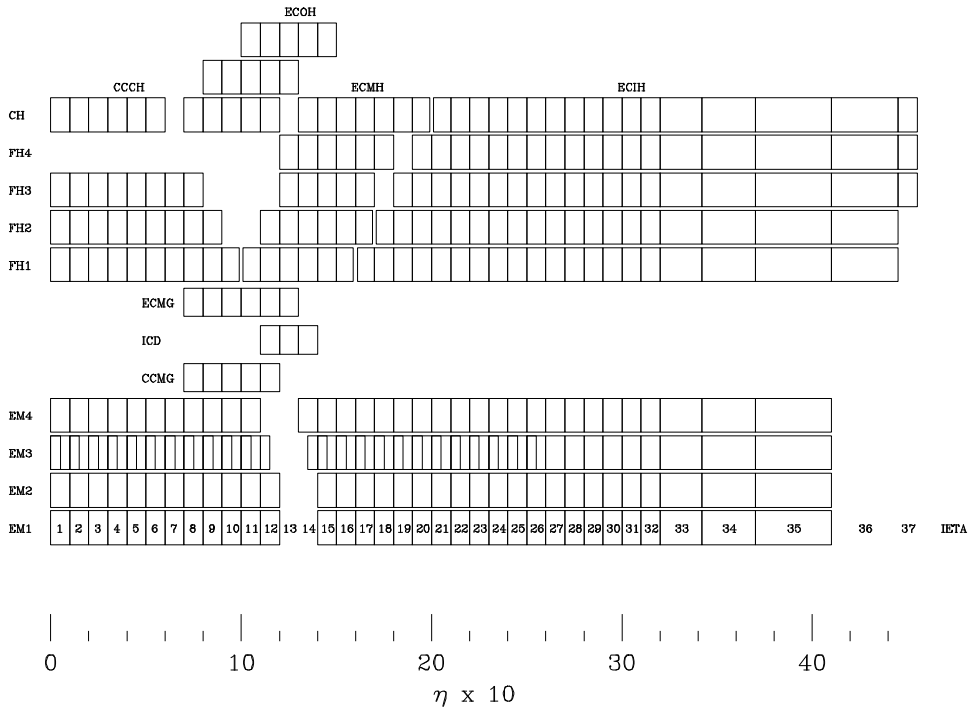

Figure 2.11: Calorimeter cell locations in terms of η.

The absorbing plate material and thickness is a function of the layers. In the EM layers depleted uranium is used with a thickness of 3 mm for the central and 4 mm for the endcap calorimeters. The fine hadronic plates employ a uranium-niobium alloy with width 6 mm. The coarse hadronic layers use thick 46.5 mm plates of copper for the central calorimeters and stainless steal for the end cap calorimeters. Table 2.1 and Table 2.2 shows summaries of various quantities for the CC and EC respectively.

In the region $0.8 < |\eta| < 1.5$ between the CC and EC cryostats there is a reduced number of total interaction lengths and little or no radiation coverage (meaning no EM calorimeter layers). Therefore, there is less sampling of jet energies. To improve the hadronic jet energy measurements in this region, which is especially

	EM	FH	CH
Number of Modules	32	16	16
Absorber	Uranium	Uranium	Copper
Absorber Thickness (mm)	3	6	46.5
Argon Gap (mm)	2.3	2.3	2.3
Number of Layers	4	3	1
Di-gaps per Cell	$2, 2, 7, 10$	$20, 16, 14$	9
Total Radiation Length (X_0)	20.5	96.0	32.9
Total Interaction Length (λ)	0.76	3.2	3.2

Table 2.1: Central Calorimeter Module Parameters.

important for determining missing energy, the following devices are employed:

- Central Cryostat Massless Gaps (CCMG) - covering $0.75 < |\eta| < 1.2$,
- End Cryostat Massless Gaps (ECMG) - covering $0.7 < |\eta| < 1.3$,
- Inner Cryostat Detectors (ICD) - covering $0.8 < |\eta| < 1.4$.

The CCMG and ECMG reside inside the cryostats and are basically calorimeter di-gaps without the absorbing plate; they are effectively very thin cells. The ICDs [11], however, are not inside the cryostats, and are instead mounted on the outside of the Endcap Cryostat. See Fig. 2.10 and Fig. 2.11 in the region $0.8 < |\eta| < 1.5$ for the CCMG, ECMG, and ICD locations.

Each ICD consists of 16 wedges in ϕ called super-tiles mounted to the Endcap

	EM	IFH	ICH	MFH	MCH	OH
Number of Modules	1	1	1	16	16	16
Absorber	Uranium	UNb	SS	UNb	SS	SS
Absorber Thickness (mm)	4	6	46.5	6	46.5	46.5
Argon Gap (mm)	0.23	0.21	0.21	0.22	0.22	0.22
Number of Layers	4	4	1	4	1	3
Di-gaps per Cell	$2, 2, 6, 8$	16	14	15	12	8
Total Radiation Length (X_0)	20.5	121.8	32.8	115.5	37.9	65.1
Total Interaction Length (λ)	0.95	4.9	3.6	4.0	4.1	7.0

Table 2.2: End Calorimeter Module Parameters. IFH, ICH, MFH, MCH, OH stand for inner fine hadronic, inner coarse hadronic, middle fine hadronic, middle coarse hadronic and outer hadronic section respectively. UNb and SS stand for Uranium-Niobium alloy and Stainless Steel.

calorimeter. Each wedge (called a super-tile) contains 12 scintillating tiles with 0.1×0.1 dimensions corresponding to the $\eta \times \phi$ dimensions of a calorimeter tower.

Figure 2.12 shows a drawing of one super-tile illustrating the 12 scintillating tiles . Each wedge is encased in aluminum. Figure 2.13 shows a photograph of one ICD. Wave length shifting fiber runs from each scintillating tile to photo multiplier tubes (PMTs). The PMTs are not mounted directly to the tiles due to the strong magnetic field between the solenoid and toroid magnets, instead they reside in crates away from the main detector.

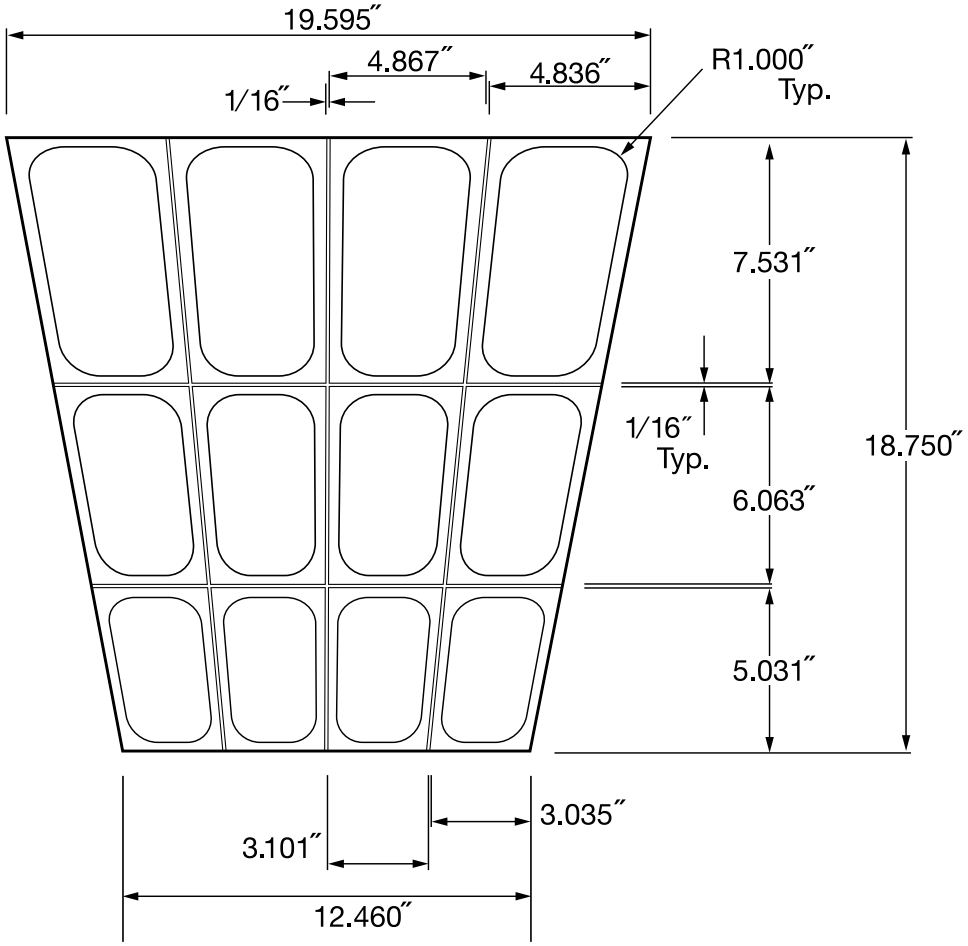

Figure 2.12: Drawing of a Inner Cryostat Detector super-wedge showing the 12 scintillating tiles

.

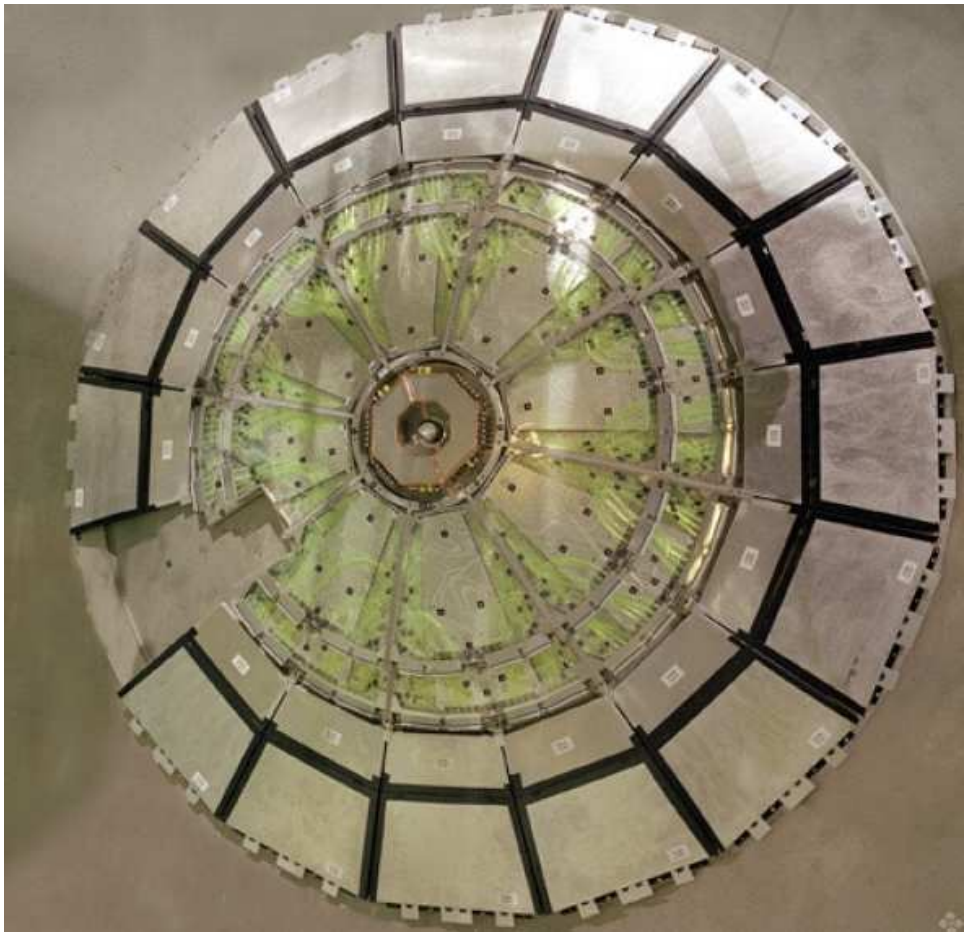

Figure 2.13: Photograph of the FPS and ICD wedges on one Endcap.

2.3.4 Muon Detectors

Muons produced in collisions at the Tevatron with energy greater than one GeV primarily lose their energy in matter through ionization. The energy loss per unit length of a muon passing through matter is fairly constant.

We can define the energy loss of a muon in matter in terms of nuclear interaction lengths. This should not be confused with the energy loss of hadronic particles. The energy of a muon moving through matter does not fall exponentially like a hadronic particle or an electron, instead the energy loss per unit length it is mostly linear from a GeV to a TeV. A muon losses about (0.23-0.25) GeV per interaction length in matter. It takes a lot of mass to stop a high energy muon.

For a muon to get to the A layer it must pass through the solenoid, preshower, and calorimeter. The solenoid and preshower together with the calorimeter have a thickness that is approximately 7-11 interaction lengths. Therefore a muon will lose approximately two to three GeV getting to the A layers. The iron toroid adds another 7-10 interaction lengths. A muon will lose approximately another 2 GeV passing through the toroid getting to the B and C layers.

The muon detector [12] is a cube and thus has rectangular symmetry. The calorimeter is contained within this cube. The four sides of the box parallel to the beam pipe are called MUC and the two sides perpendicular to the beam pipe are called MUF. Because the detector has rectangular symmetry and not cylindrical symmetry the edges of MUF and MUF are not at at a constant η, however, to a rough approximation the boundary of MUC and MUF is at $|\eta| = 1$. The detectors

are made in three layers of wire chambers. Two to three of these layers also have scintillators. The layers are called the A, B, and C-layers. The drift tubes measure z and either x or y (but not both). The scintillators determine ϕ. Additionally, the scintillators provide timing for triggers and for background reduction. Figure 2.14 shows an expanded view of the drift chamber location for each layer; Fig 2.15 shows a similar drawing with the scintillator tiles. A thick iron toroid magnet of 1.8 Tesla resides after the A-layer and before the B and C-layers.

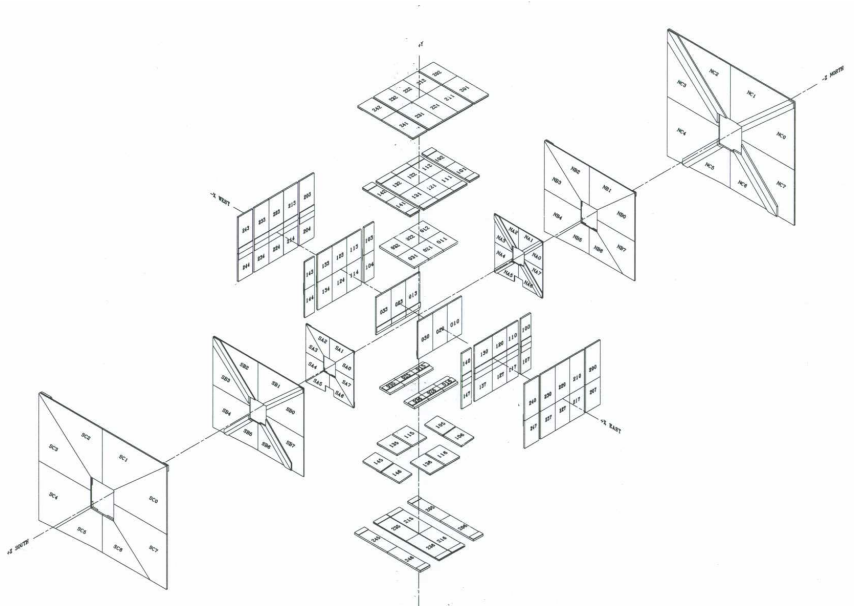

Figure 2.14: Drawing of the wire chambers locations in the muon detectors.

A drift tube is an enclosed vessel filled with a gas and an electric field gradient. A charged particle passing through a drift tube ionizes the gas, the electrons move (drift) in the electric gradient and are collected at the anode. By determining the drift time of the electrons the location of the particle through the drift tube can be determined.

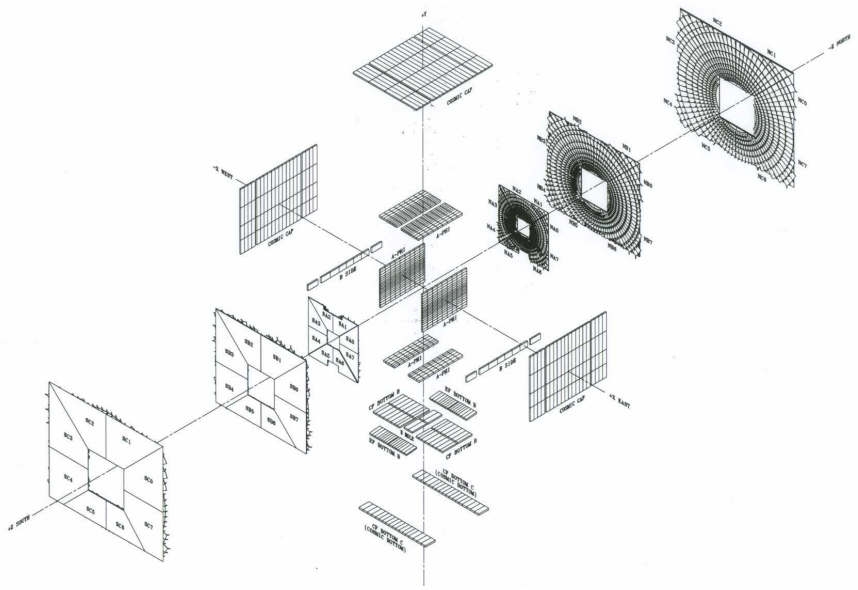

Figure 2.15: Drawing of scintillator tile location in the muon detectors.

The MUC detector uses proportional drift tubes (PDTs). Each PDT consists of an aluminum box 10 cm wide, an anode wire at the center, and two cathode copper pads on the inside of the aluminum box above and below the anode. The enclosure is filled with a gas mixture of 84% argon, 8% CF_4, and 8% CH_4. The anodes operate at 4.7 kV and the cathodes at 2.3 kV. The maximum drift time of electrons in the 10 cm drift tubes is 450 ns. The PDTs can resolve the distance a particle passed within the anode wire within 1 mm. The PDTs are arranged in decks: four decks for the A-layer, and three decks for each of the B and C layers. Fig. 2.16 shows a cross section of the four decks of the A-layer. There are 6624 PDT cells installed in the MUC detector.

For the MUF detector mini drift tubes (MDTs) are used. The MDT cells are significantly smaller than the PDTs with dimensions approximately 1×1 cm^2.

There are 8 tubes per MDT module (meaning a module is roughly 8 cm wide). An anode wire is suspended in the center of each tube, the wires are supported by plastic spacers every meter (in the direction along the wire). The length of the MTDs varies from 1 to 6 m. The gas mixture is 90% CF_4, and 10% CH_4. The drift time is approxiamtley 10 ns per mm from the anode. Fig. 2.18 shows the MDT location in one side of MUF (other side has a nearly identical layout). Note that a muon passing through a tube only provides positional measurement in one direction on the layer surface, either x or y (z is also determined). The A layer has four layers of MDTs, the B and C layers have three layers.

Both the drift tubes and scintillators for MUC and MUF are built in ϕ octants. The boundaries of the octants are called the octant gaps, these regions are partially dead which reduces the overall muon acceptance. For MUC there are additional gaps along Z, however, a particle that transverses a z gap at one layer is unlikely to transverse another z gap at another layer. Therefore, the acceptance loss at the η gaps is not as significant. See Fig 2.14, Fig 2.15, and Fig. 2.18 for clarification on the octant gap and z gap locations.

The calorimeter, which resides inside the muon detector cube must be supported. These supports lead to gaps inside the muon detectors. This region is denoted the muon hole region. In part of the hole region there are no drift tubes or scintillators. Section 4.5.3.1 discusses the octant gaps, z gaps, and hole region in more detail.

The muon detector scintillators provide crucial timing information for triggering and the drift tubes. MUC generally only has two layers of scintillating counters,

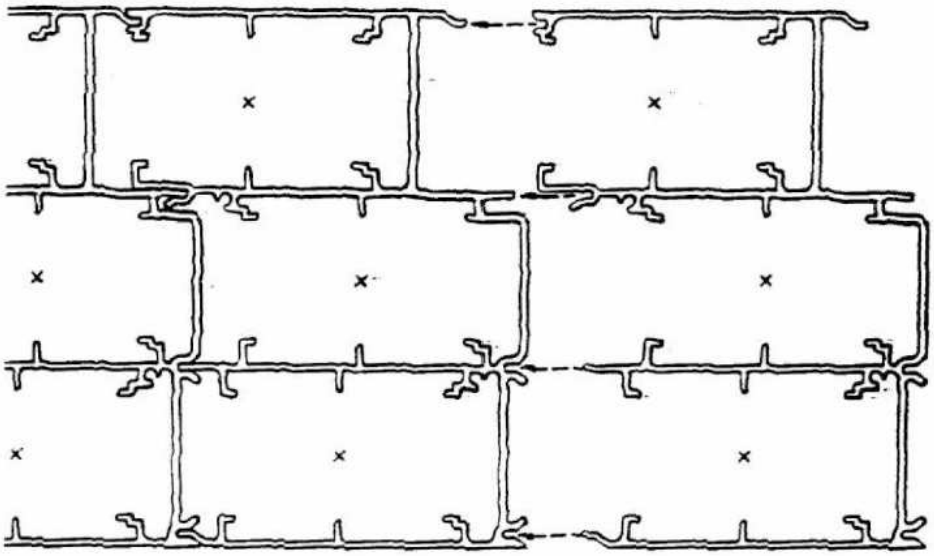

Figure 2.16: Cross section of the four decks of proportional drift tubes in MUC

.

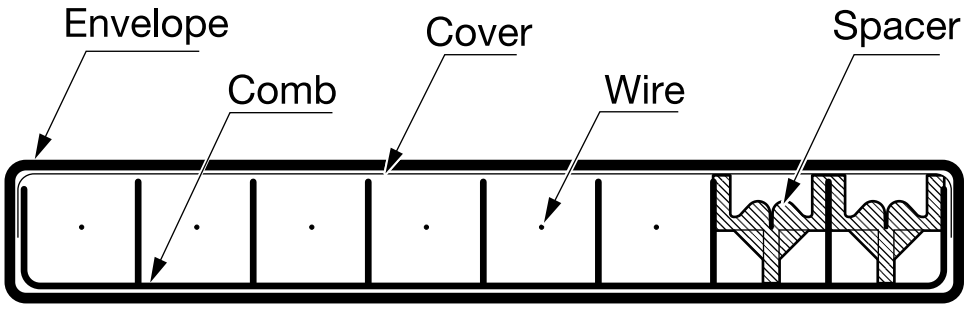

Figure 2.17: Cross section of a series of mini drift tubes.

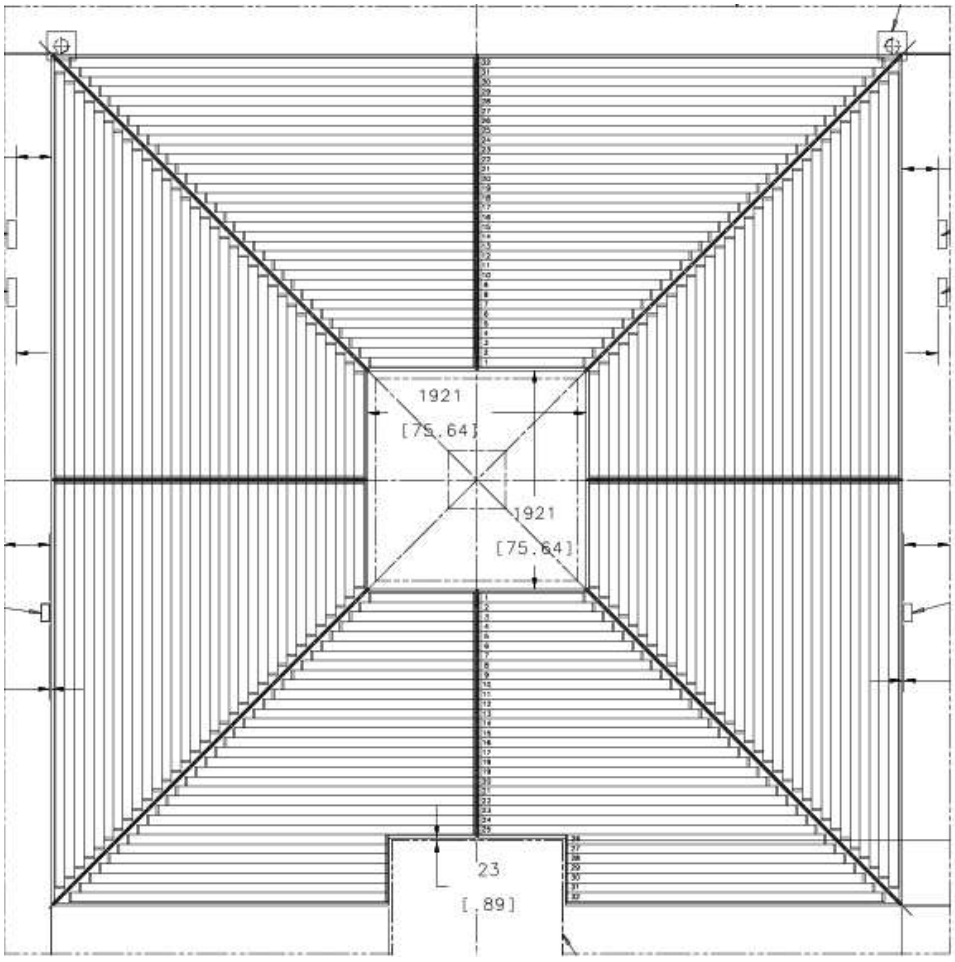

Figure 2.18: Drawing of the mini drift tube layout for one layer.

one at the A-layer and one at the C-layer. There are some B-layer scintillators at the lower side and lower edges of the detector cube.

Special consideration was give to the A-Layer scintillators which must operate in the residual magnetic field between the solenoid magnet and toroid magnets (200-350 G). Cylindrical metal shields surround each PMT for the A-layer. Within the shield the magnetic field is reduced to less than 1 G. The size of the counters in the C-Layer is 200 cm $\times$ 40 cm and 12.7 mm thick; each counter is arranged so that it covers about 4.2° in ϕ. Wave length shifting (WLS) fiber is embedded in a machined grove in each panel. The fibers are bundled together and directed onto PMTs. Each counter is encased in a welded aluminum box. A-layer counters have a length of 84.5 cm and their widths vary from 23.1 to 36.7 cm.

The MUF scintillator counters (also called pixel counters) are trapezoidal shaped rather than rectangular. The MUF pixel counters are arranged concentrically around the beam-pipe. There are 4214 pixel counters in total. Fig. 2.19 shows a photograph of the C-Layer pixel counters. The ϕ-segmentation is 4.5°. The pixel counters vary in size from 9 $\times$ 14 cm^2 to 60 $\times$ 110 cm^2. The pixel counters use the same scintillating plastic as the central pixel counters. Table. 2.3 shows a summary of the number of drift tubes and scintillators for the muon detectors.

The toroid magnets are built in four parts: two central pieces parallel to the beam pipe, and two end caps perpendicular to the beam pipe. Each piece is made of iron. The central toroids have 20 coils with 10 turns per coil. The forward toroids have 8 coils with 8 turns per coil. Figure 2.20 shows drawings of the central toroid and one forward toroid highlighting the coils. Each coil is connected in series

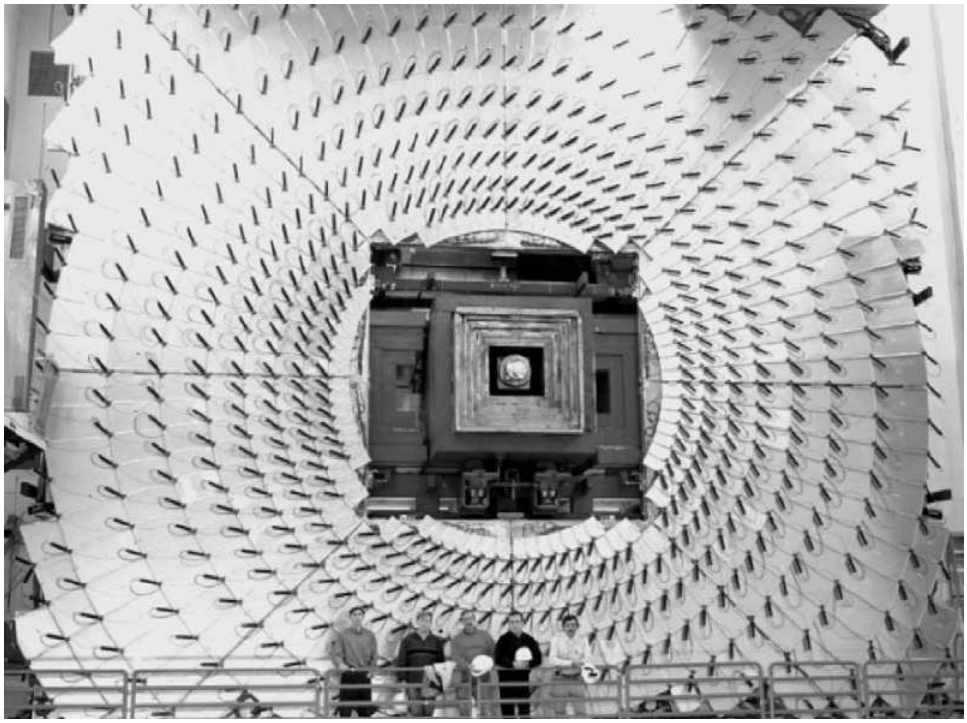

Figure 2.19: Photograph of one side of the MUF C-layer pixel counters.

and operate at a current of 1500 A. The current in the toroid magnets and the solenoid magnets is periodically reversed between stores so that data is taken in the four possible field orientations $(+z,+z),(+z,-z),(-z,+z),(-z,-z)$. The magnetic field lines of the solenoid are returned by the toroid magnet as shown in Fig. 2.21.

2.3.5 Luminosity Monitor

Typical inelastic collisions produce low p_T events. The collection of final state pions carry most of the longitudinal momentum of the proton or anti-proton from which they fragment from before collisions, therefore the scattering angle is small ($p_T/p_Z = \tan(\theta)$). Small angle corresponds to large η. By counting interactions at high η the inelastic cross-section can be determined.

Item	Layer A	Layer B	Layer C	Total
PDT cells	1584	2424	2616	6624
MDT cells	16,384	15,552	16,704	48,640
Central scint. counters	630	96	276	1002
Forward scint. counters	1518	1420	1276	4214

Table 2.3: Muon detector drift tube and scintillator counts

The number of events observed N is defined as:

$$N = AL\sigma \tag{2.10}$$

where A is our efficiency for observing the event, L is the total luminosity, and σ is the cross section for the process.

The DØ luminosity system consists of an array of scintillating wedges arranged in a circle around the beam-pipe at $|z| = 140$ cm. The scintillating wedges cover $2.7 < |\eta| < 4.2$. Photo multiplier tubes are used to convert the light to an electric signal. Figure 2.22 shows a drawing of the luminosity monitor system.

An estimation of the interaction point along the beam axis is $fastz = \frac{c}{2}\Delta t$, where Δt is the time difference between the two scintillating counters. This is used to determine if a beam has a halo; residual particles moving with the beam but outside the main beam. Beam halo peaks at $|fastz| = 140$ cm; the luminosity counters ignore events with $|fastz| > 100$ cm.

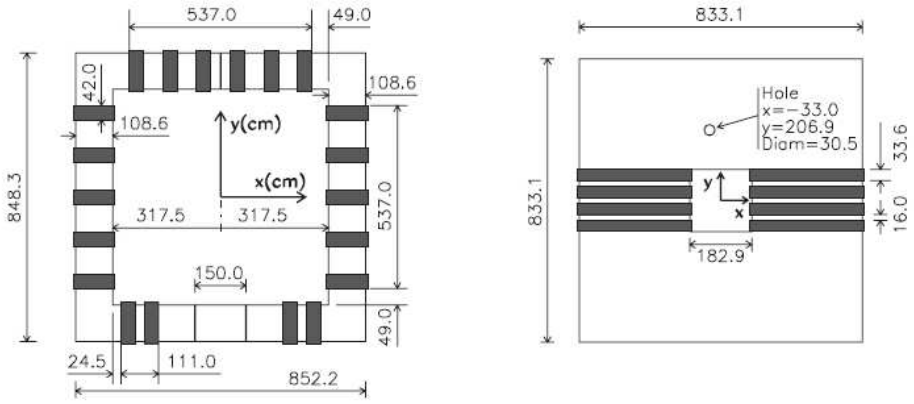

Figure 2.20: Drawing of the central toroids and one forward toroid. The dark bands represent the coils of the toroids. The hole at $(x = -33, y = 206.9)$ is from the Main Ring in Run I, in Run II it is filled with concrete.

2.3.6 Trigger

It takes 21 μs for a bunch to make one revolution around the Tevatron. There are three super-bunches and 12 bunches per super bunch in one beam. Therefore there are $36/21\mu\text{s} = 1.7$ million bunch crossings per second. The data collected during one bunch crossing is called an event. Each event requires 0.25 MB. If we recorded every bunch crossing in a second we would need 425 GB per second; such a storage rate is not practical. Instead we must apply a selection process which keeps certain events and rejects others. This selection process is done by the Trigger system.

The DØ trigger system has a three level hierarchy called the Level 1 (L1), Level 2 (L2), and Level 3 (L3) trigger. L1 reduces the event rate by a factor of 1000, L2 by a factor of 2-5, and L3 by a factor of 10. The final result of the trigger

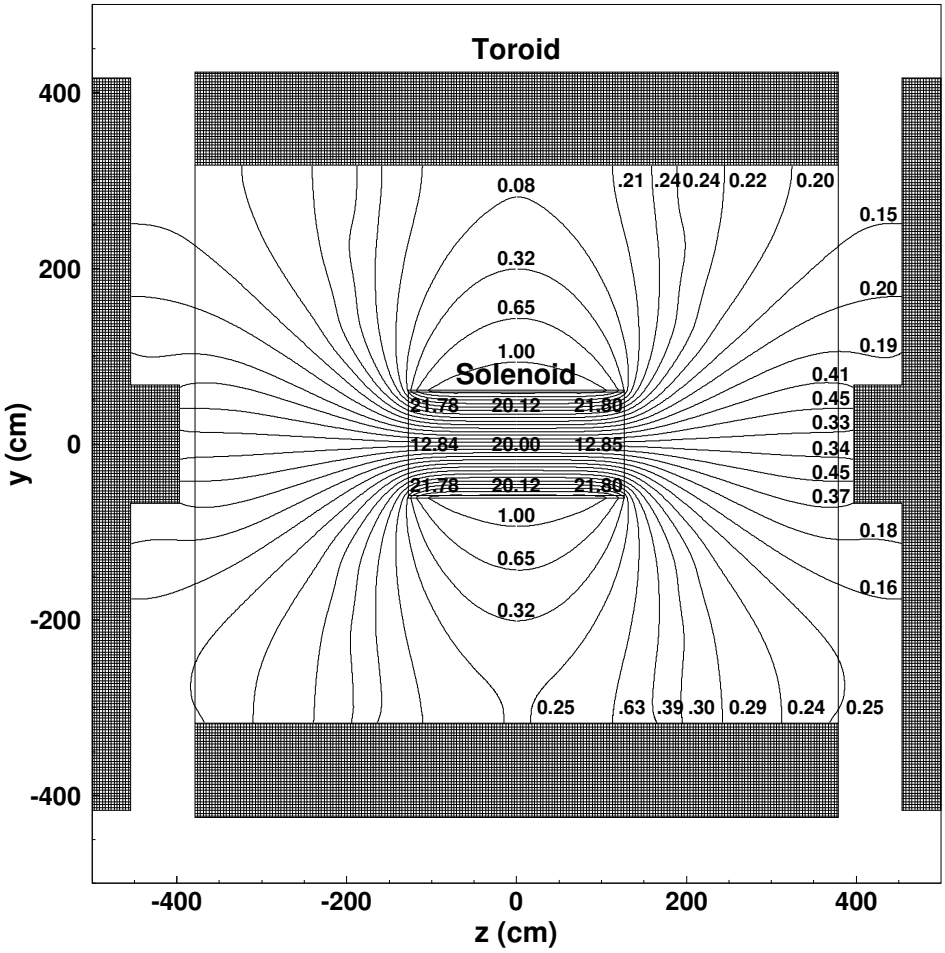

Figure 2.21: Magnetic field lines between the solenoid magnet and the toroid magnets

.

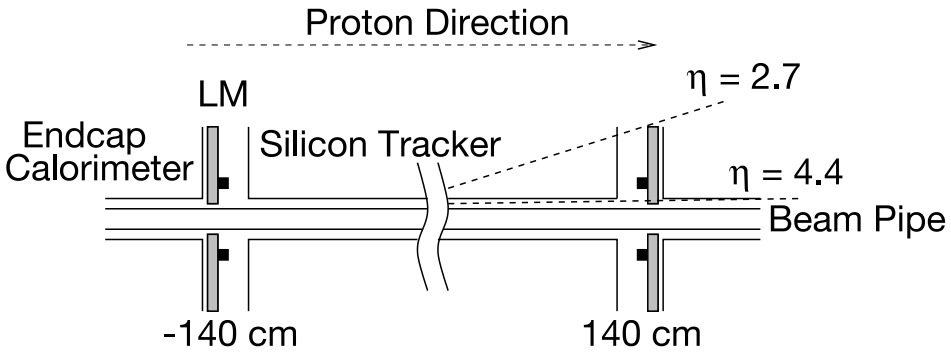

Figure 2.22: $r - z$ view of the luminosity monitor system.

pipeline is a selection rate of 40 to 80 events per second out of 1.7 million events per second. This corresponds to a storage rate of approximately 12 MB per second.

The L1 trigger selection is a hardware trigger based on fast readout of the detector. The L1 sub-detector triggers are (L1Cal) and (L1Muon). Events which are passed onto L2 are partially reconstructed to look for lepton and jet like objects. The selection is based on hardware and software decisions. The Level 3 trigger is a farm of fast computers and the decision is based on reconstructed physics objects.

Chapter 3

Event Reconstruction and Particle Identification

In this chapter we discuss how the raw data from each of the different sub-detectors is reconstructed to select objects with particle properties. This process is done with the D0reco packages. D0reco is the name of the computer program that takes the raw data from the different sub-detectors, converts analog to digitial (ADC) counts to energy, applies appropriate calibrations, does pedestal subtractions, and so forth.

3.1 Track and Vertex Reconstruction

A charged particle moving through the tracking system leaves hits in the SMT and CFT. These hits are reconstructed into tracks in three steps:

1. Cluster Finding - points in space reconstructed from hits in the SMT or CFT.
2. Pattern Recognition - find lists of clusters which form track candidates
3. Filtering and Refitting - remove duplicate track candidates and find track properties such as p_T.

Recall that the SMT has dual layer and single layers of silicon strips. The stereo layers strips are arranged perpendicular to one another so that they provide both a x and a y measurement (in the plane of the strip). The single layers only

provide one measurement of x or y. Each barrel of the CFT has an axial fiber and two fibers, called the stereo fibers. The axial fiber measures ϕ and r, the stereo layers allow a measurement we will call tilt which gives a direction on the surface of the fiber barrel.

The cluster finding algorithm takes the raw data from the silicon strips and the central fibers and converts the charge into spatial measurements. Based on each of the different SMT and CFT measurements there are four cluster types:

1. SMT cluster with x, y, and z,
2. SMT cluster with z and either x or y (but not both),
3. CFT cluster with r, ϕ, and a tilt,
4. CFT cluster with r and ϕ and no tilt.

The number of hits in both the SMT and CFT for most events ranges from 10,000 to 1,000,000. Once all hits in the SMT and CFT have been converted into clusters, the clusters are used as inputs to pattern recognition algorithms which will output arrays of clusters which are track candidates.

The DØ track reconstruction software uses two different track pattern recognition algorithms, each of which is run independently. The algorithms are the Histogram Track Finder (HTF) [26] and the Alternative Algorithm (AA) [27]. Both of these algorithms start with seed clusters and one by one add other clusters along a path (called a road). Pattern recognition is used to determine the most likely list of clusters to form tracks.

Besides creating lists of clusters the pattern recognition software provides first order measurements of track properties such as curvature. This first guess of the track properties along with the lists of track cluster candidates is sent to the Kalman track fit algorithm [28], which simulates the effect of the non uniform magnetic field and interaction of charged particles with the matter of the SMT, CFT, and beam-pipe which have small but non negligible radiation and interaction lengths which must be accounted for. Additionally, the two different pattern recognition algorithms, HTF and AA, often produce the same track candidates; these duplicates must be removed.

The final list of reconstructed tracks contains multiple parameters such as ρ, the curvature of the track and the distance of closest approach (DCA) of the track with respect to the beamspot. A Z boson decays promptly so the DCA of a track matched to a lepton from Z boson decay should be very small. The DCA is useful to identify and remove multiple backgrounds such as from short lived (but not prompt) decays of for example B mesons (from QCD and top quark events) and τ leptons. Additionally, cosmic rays and beam halo have random DCA distributions.

From the curvature ρ of the track and the magnitude and direction of the magnetic field the q/p_T, where q is charge of a track is determined. Recall that the direction of the magnetic field changes between stores, additionally the magnitude of the magnetic field has changed during RunIIa.

3.2 Electron and Photon Reconstruction

Before discussing how D0reco selects EM objects, it is important to understand where an electron or photon deposits energy in the calorimeter. An example is helpful. The energy deposition of a 45 GeV electron as a function of radiation length is shown in Fig. 3.1. From this figure it is clear that an electron deposits energy in a DEAD region, four EM layers, and the first FH layer. The region labeled "DEAD" represent the preshower, solenoid, cryostat walls, and central tracker. Unfortunately the energy readout of the preshower detector is useless for electrons with $p_T >$ 5 GeV [23]. Another important feature to notice is that the profile is shifted such that the peak of the profile falls between the second and third EM layers. The addition of the solenoid and preshower has shifted the peak from being primarily in the third layer, as it was in Run I [1], to being between the second and third EM layers in Run II. This affects the energy resolution.

In order to best measure the energy of an electron or photon, the energy deposition in the four EM layers and first FH layer should be used. D0reco starts by doing what is called preclustering. The algorithm to find preclusters is the Simple Cone algorithm. First EM towers are sorted by E_T. An EM tower is defined as the four EM layers (EM1-4) of the calorimeter plus the first Fine Hadronic (FH1) layer in a 0.1×0.1 ($\eta \times \phi$) projection. The EM tower with the largest E_T is selected to be the seed tower. A EM cluster is defined to be the seed tower and all the towers

[1] The Tevatron ran at $\sqrt{s} = 1.8$ TeV from 1992-1996; this period is know ans Run I. After 1996 the Tevatron was upgraded (so was the DØ detector) and has been running at $\sqrt{s} = 1.96$ TeV since 2001; this later period is know as Run II.

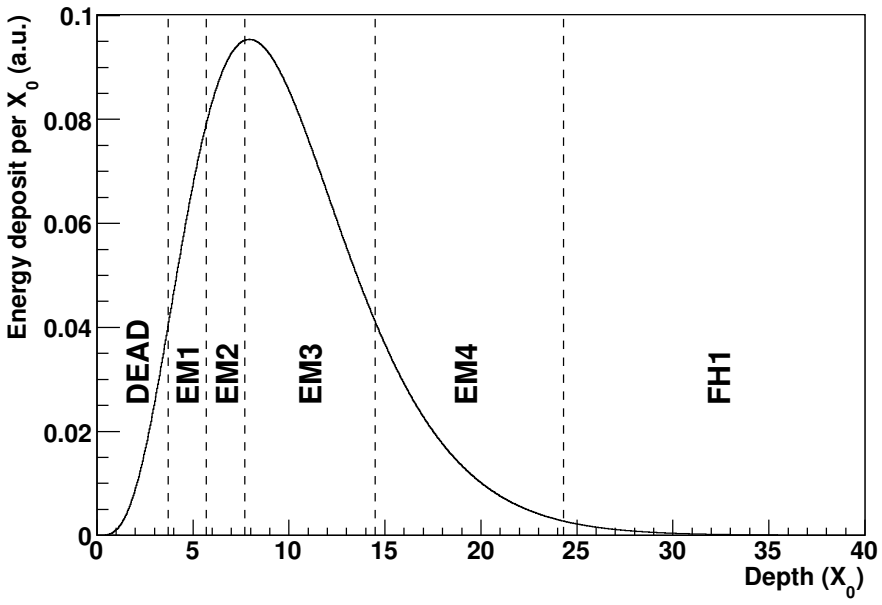

Figure 3.1: Energy deposition per radiation length X_0

within a 0.4 centered on the seed tower, this corresponds to 13 towers.

An EM precluster must then pass a few loose selection cuts. The EM cluster energy isolation f_{iso} is defined as:

$$f_{iso} = \frac{E_{total}(\Delta R = 0.5) - E_{EM}(\Delta R = 0.2)}{E_{EM}(\Delta R = 0.2)} \tag{3.1}$$

The variable E_{total} is the defined to be the energy of all layers in a 0.1×0.1 tower and E_{EM} is the energy of EM layers plus the first FH layer. The fraction f_{EM} of EM cluster energy compared to the total energy is defined as:

$$f_{EM} = E_{EM}/E_{total} \tag{3.2}$$

Hadronic showers deposit on average less than 10% of their energy in the EM layers of the calorimeter. Additionally, hadronic showers have a broader distribution in $\eta \times \phi$. The variables f_{iso} and f_{EM} are useful to discriminate against hadronic jets.

Only clusters with $f_{iso} < 0.2$, $f_{EM} > 0.9$, and $E_T > 1.5$ GeV are selected. Clusters which pass these criteria are stored in a list and a search is done for a track match to the cluster. For each reconstructed track a fit quality variable χ^2 defined as:

$$\chi^2 = \left(\frac{\Delta\phi}{\sigma_{\Delta\phi}}\right)^2 + \left(\frac{\Delta z}{\sigma_{\Delta z}}\right)^2 + \left(\frac{E_T/p_T - 1}{\sigma_{E_T/p_T}}\right)^2 \tag{3.3}$$

is determined. The z and ϕ of the track and EM cluster are determined by projecting to the third floor of the calorimeter, Δz and $\Delta\phi$ are the difference from the track and EM cluster. For EM clusters in the EC region of the calorimeter the E_T/p_T term is dropped. If a track has its probability of χ^2 greater than 0.01 the EM cluster is considered to have a track match. Each cluster is assigned a variable called $EMID$ which is assigned value of +11 or -11 if the cluster has a track match (the charge from the track match determines the sign) or a value of 10 if the cluster has no track.

The EM cluster centroid is determined using a log-weighted algorithm. The θ (and hence η) and ϕ of a EM cluster is determined from the z component of the track vertex if the cluster has a track match or from the cluster centroid and z component of the primary vertex if the track has no track match. The energy E of the EM cluster is defined as the total energy in the four EM layers and FH layer. We define $p_T = E\sin(\theta)$. The momentum four vector is defined in terms of p_T as $p_\mu = (E, p_T\cos(\phi), p_T\sin(\phi), p_T\sinh(\eta))$. Besides η another useful variable is η_D (detector-η) of the EM cluster which is defined as the η of the EM cluster projected from the origin to the third EM layer.

A few multivariate discriminators are determined based on a number of inputs.

The first discriminator has seven inputs and is denoted as H-matrix7($hmx7$). H-matrix7 is based primarily on the shape of the EM shower. The seven inputs are: f_{EM} for each of the four EM layers, the primary vertex, E, and the size of the cluster in $\eta \times \phi$ at the third EM layer. A H-Matrix8 ($hmx8$) discriminator is also defined with 8 inputs, seven of which are the same as $hmx7$ with one more input based on the transverse width of the shower.

Another important multivariate discriminator is Likelihood which incorporates tracking information as well as shower shape. The Likelihood discriminator has seven inputs which are (including upper and lower bounds):

- $0.90 < f_{EM} < 1.0$,
- $0 < hmx7 < 50$,
- $E_T/P_T < 3.1$,
- Probability($\chi^2_{spatial}$)> 0,
- $|DCA|$ from the primary vertex < 0.05 for tracks with SMT hits,
- Number of tracks in a cone of $R = 0.05 < 5$,
- Total track p_T in a cone of $R = 0.4 < 3.5$ GeV.

Any EM cluster which does not meet any of the bounds is assigned Likelihood $= -1$.

3.3 Jet Reconstruction

Free quarks do not exist as long lived particles; they must go through a process called hadronization which pulls quark anti-quark pairs out of the vacuum to form color neutral particles (color confinement). This process continues pulling quark anti-quark pairs out of the vacuum forming hadrons along the way. Most of the hadrons produced are pions. This results in a jet of final state hadrons. The charged pions leave many hits in the tracking detectors and then shower in the calorimeter. The neutral pions decay almost immediately (on order 10^{-16} s) to photon pairs which create an EM shower.

Jets at DØ are reconstructed based on calorimeter information. This is done in four steps [24]. The first step, denoted the E-Scheme, forms jet towers from the calorimeter cell. The second step uses the Jet Simple Cone Algorithm to find a list of preclusters. This is similar to finding EM cluster. The list of preclusters is used as seeds for the Run II Cone Algorithm to find a list of proto-jets. Finally, the list of proto-jets is run through a Merging and Splitting Algorithm to remove double counting and produce the final list of jet candidates.

The E-Scheme calculates momentum four-vector $(E, \vec{p})_n$ (assuming zero mass) for each calorimeter cell n. Where E of the cell is the measured energy and the momentum vector $\vec{p}$ has magnitude E of the cell and direction defined from the primary vertex to the center of the read out channel. Noisy read out channels are removed. Jet tower momentum four vectors $(E^{\text{tower}}, \vec{p}^{\text{tower}})$ are defined as:

$$(E^{\text{tower}}, \vec{p}^{\text{tower}}) = \sum_{n=1}^{N} (E, \vec{p})_n \tag{3.4}$$

where the sum is over all read out channels in one 0.1×0.1 wedge. The jet tower momentum four vectors, unlike the momentum four-vectors of the read out channels, can have mass. Once all jet towers have been formed the list is passed onto the Simple Cone algorithm.

The Simple Cone Algorithm first loops through a list of jet towers and sorts them by p_T until there is no jet tower with $P_T > 500$ MeV. Starting with the first tower in the sorted list, called the seed, the first highest E_T jet tower within $\Delta R < 0.3$ of the seed is added to a precluster P, the center of the precluster is recalculated based on the E-Scheme and becomes the new seed. This process repeats until there are now more jet towers with $\Delta R < 0.3$ to add to the precluster. The next highest p_T remaining jet tower in the list becomes a seed for a new precluster and the process repeats until no more seed preclusters remain. Once all the precluster list has been formed all preclusters with $p_T < 1$ GeV and those formed from only one jet tower are removed.

The Run II cone algorithm takes the list of preclusters (sorted by p_T) and forms a list of proto-jets. For the Run II cone algorithm $\Delta R = \sqrt{(\Delta Y)^2 + (\Delta\phi)^2}$, where ΔY is the difference in the rapidity and not the pseudorapidity. This is done because the jet tower momentum four-vectors can have mass. The first precluster tests if $\Delta R/2 > 0.5$, if true the precluster becomes a seed for a proto-jet, if false the precluster is skipped and the next precluster is tested. A seed proto-jet is used as a proto-jet candidate (PC). All preclusters within a $\Delta R > 0.5$ are added to the PC based on the E-scheme until the PC is stable. This PC is added to the list of proto-jets and the process repeats. Proto-jets can share p_T and therefore to avoid

double counting a Merging and Splitting algorithm is employed.

The Merging and Splitting algorithm takes the list of proto-jets, sorted by p_T, and test if any proto-jets jets share p_T with another. If the shared p_T between proto-jets is greater than 50% of either of the proto-jets total p_T the proto-jets are merged to form a new proto-jet (removing the former proto-jets from the list) and the process repeats. If the shared p_T between proto-jets is less than 50% than the shared p_T is assigned to only one of the pro-jets and the proto-jets are reordered in p_T. This process continues until no more merging and splitting is necessary. The final list of pro-jets becomes the list of reconstructed jets.

Various variables are calculated for each reconstructed jet such as the jet momentum four-vector as well as jet specific variables. The reconstructed jet variables we use are :

- chf - fraction of jet p_T in the coarse hadronic layers.
- f_{EM} - fraction of jet p_T in the EM layers of the jet towers.
- $hotf$ - ratio of the cell with the highest p_T to the cell with the next highest.
- $n90$ - the number of jets with 90% of the total jet p_T.

Most electrons and photons will be reconstructed as jets; f_{EM} and $n90$ help to distinguish real jets from real electrons and photons. The variables chf, $hotf$, and $n90$ are used to remove instrumental effects where noisy cells fake jets.

3.4 Muon Reconstruction

There are three types of reconstructed muons: muons found with the muon detector with a momentum determined from the central tracker (central-muons), muons found in the muon detector with their momentum determined from the toroid magnets (local-muons), and muons found in the calorimeter (calorimeter-muons). There are muons definitions which combine both local and central tracking information, however, these definitions have a resolution which is at best only as good as central-muons. Calorimeter-muons have a much lower identification efficiency than central-muons. For these reason we only will only concern ourselves with central-muons.

The time it takes electrons created by a muon in the gas of the drift tube to reach the anode wire is used to determine the radius of a circle from which the muon could have originated. As a muon transverses multiple drift tubes circles are determined for each wire of the tubes. A straight line is then fitted between the circles [16]. The line fit is called a segment. Figure 3.2 shows a cartoon of a muon moving through drift tubes with the circle for each wire and a line fit of its path.

The B and C-layers can be though of as one layer which we call the BC-layer, the A-layer is not grouped with the others because it is sandwiched between the BC layer by the thick toroid magnet. The minimum number of wire hits necessary in a layer to form a segment is two [15]. Each segment must be associated with at least one scintillator hit in the layer of the segment. Only one segment is required to reconstruct a muon. We classify four types of central-muons with a variable called

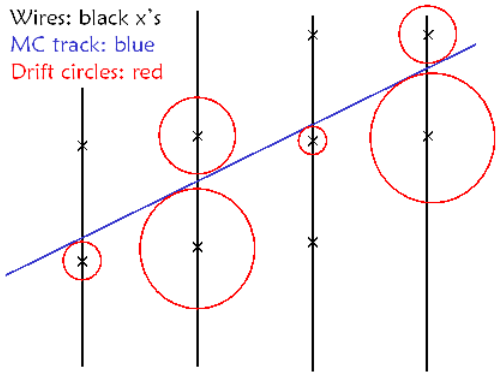

Figure 3.2: Cartoon drawing of a muon transversing drift tubes. The circles represent the possible location the muon was produced in each cell.

nseg:

1. $nseg = 1$ – A-Layer segment only,
2. $nseg = 2B$ – BC-layer segment only and B layer scintillator timing,
3. $nseg = 2C$ – BC-layer segment only and C layer scintillator timing only,
4. $nseg = 3$ – A-Layer and a BC-layer segment.

Most muons from for example Z boson decays have $nseg = 3$.

Once segments have been found, an attempt is made to fit reconstructed tracks from the central tracking system to the segments [17]. Each segment matched to a track is placed into the final list of reconstructed muons. The transverse momentum p_T of the muon is determined from the track it is matched to by the relation $p_T = qRB$, where R is the radius of curvature of the track, B is the magnetic field (2 T), and q is the charge of the muon (± 1). The η and ϕ are determined from the track

match. It is also useful to define a detector-η (η_D) for muons. The angle between the origin and the intersection of the track match projected onto the A-Layer (even if the muon does not have an A-Layer segment), defines η_D for muons. The q/p_T of tracks matched to muons that only have CFT hits is corrected using the beamspot [18]; this greatly improves the p_T resolution of tracks without SMT hits.

Various variables are employed from the reconstructed muons, the most relevant ones are listed as follows:

- iso - the sum of the energy in $\Delta R = 0.4$ centered on the jet minus the sum of the energy in a cone with $\Delta R = 0.2$
- $timeA, B, C$ - scintillator timing at the A, B, or C-layer (if the muon has scintillator timing at those layers)

The variable iso is useful to reduce the background from hadronic punch through for muons only identified at the A-layer. Scintillator timing helps reduce backgrounds from cosmic rays, beam backscatter, and beam halo. However, the DCA and z_{vtx} of the track matched to the muon are significantly more useful than scintillator timing.

Chapter 4

Analysis

In this chapter is discussed the methods used to search for Z boson pair from Standard Model production. The number of events N_{exp} expected to be observed in a channel is:

$$N_{exp} = (\sigma Br)LA + B \tag{4.1}$$

where L is the luminosity, A is the acceptance, σBr is the cross section times branching ratio, and B is the background. The variable σ is determined from theory to be 1.6 pb [2]. The branching ratios for each channel are known from [3]. Three quantities remain to be measured for each channel: the number of observed events N, the acceptance A, and the total background B. The details for how these quantities are determined for each channel are discussed in Sec. 4.5, Sec. 4.6, and Sec. 4.7. For now, though, we will discuss the general methods used to determine these quantities.

4.1 Event Selection - Determining N

All channels must have a least four reconstructed leptons as defined in Sec. 3.2 and Sec. 3.4. Electrons and muons in all channels are required to have $p_T > 15$ GeV. Electrons are restricted to $|\eta_D| < 1.1$ or $1.5 < |\eta_D| < 3.2$. Muons have no explicit η_D restrictions, however, reconstructed muons are implicitly required to have roughly

$|\eta_D| < 2.0$. In the $eeee$ channel, at least three electrons must have a loose track match; in the $\mu\mu ee$ channel both electrons must have loose track matches. Muons are restricted to be close to the beam spot and the difference in the vertex along the beam-pipe between all muons must be less than 3 cm. Only muons identified before the toroid are required to be isolated. Finally, the Z bosons for a ZZ candidate must have $M_{\ell\ell} > 30$ GeV.

4.2 Acceptance A

The acceptance A, is the fraction of events which would be observed compared to the total events produced. There are holes in $\eta - \phi$ space for which there is no detector coverage. Additionally, kinematic cuts on the leptons and between lepton pairs limit the total phase space of ZZ production. Finally, the detectors are not perfect and therefore do not identify every lepton that passes through them. All these factors must be considered in determining the acceptance A.

A Monte Carlo event generator is used to create a list of four-momenta of the four final state leptons from the Z boson pairs. The effect of the detector on the four-momenta of each lepton is simulated in order to determine the event acceptance. The detector is simulated in three steps:

- Smear the four-momenta of each lepton to simulate the resolution of the detector sub-systems.
- Apply geometric and kinematic selection cuts based on the detector boundaries and lepton selection.

- Test each lepton based on its four-momenta to see if it passes the identification efficiency.

4.2.1 Standard Model Event Generator

For the SM ZZ cross section, the event generator PYTHIA is used. The acceptance is defined for $M_{\ell\ell} > 30$ GeV for the leptons which came from the Z bosons from generator level.

4.2.2 Detector Resolution

The resolution of the calorimeter and muon detectors is modeled with a DØ framework package know as PMCS [38]. PMCS takes the generator level four-momenta of each lepton from PYTHIA and smears four-momenta to simulate the detector resolution.

4.2.2.1 Calorimeter Resolution

The energy resolution of the Calorimeter is modeled with three terms. The first is called the noise term N. This is a fixed value independent of the energy of a particle. The second term is the sampling term S resulting from statistical fluctuations in the energy deposited in a read-out channel. The last term is the constant term C which represents how well we know the calorimeter is calibrated. We can write the energy resolution of the calorimeter as:

$$\left(\frac{\delta E}{E}\right)^2 = \left(\frac{N}{E}\right)^2 + \left(\frac{S}{\sqrt{E}}\right)^2 + C^2 \tag{4.2}$$

Figure 4.1 shows the energy resolution of the calorimeter as a function of E and the three parameters N, S, and C. Recent results have shown some η dependence for the sampling term as well as a stronger energy dependence, however, for the level of precision of this analysis flat terms are sufficient. Figure 4.1 shows the resolution of the calorimeter as a function of the three terms. PMCS uses different terms for the CC and EC.

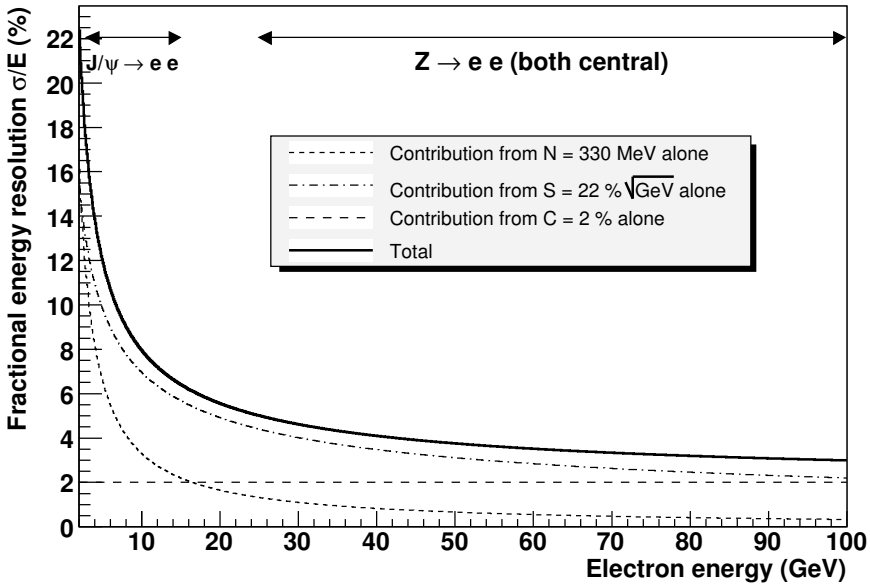

Figure 4.1: Resolution of the calorimeter as a function of E and the three parameters: N, S, and C.

4.2.2.2 Muon Detector Resolution

The momentum of reconstructed muons is determined from the reconstructed track matched to segments in the layers of the muon detectors. Unlike electrons, the

momentum resolution does not improve with large p_T; for muons the momentum resolution improves inversely with p_T. Therefore, the resolution is modeled inversely to the p_T of the track. Given a generator level $p_T(gen)$ the smeared $p_T(smear)$ is modeled in two steps. First by smearing the $p_T(gen)$ with the relation:

$$\frac{\sigma/p'_T}{1/p_{T'}} = \sqrt{\frac{A^2 p_T(gen)^2}{L^4} + \frac{B^2}{L\sin(\theta)}} \tag{4.3}$$

where L represents the track bending lever arm, A presents measurements uncertainties in the trackering detector, and B represents the effect of multiple scattering. The final $p_T(smear)$ is scaled with the relation:

$$p_T(smear) = Cp'_T \tag{4.4}$$

where C models imperfections in the magnetic field.

4.2.3 Single Lepton Efficiencies

The efficiencies to identify the leptons are necessary to model the detector. The principal method used to determine the lepton efficiencies is called the tag and probe method [19]. This is based on finding $Z \to \ell\ell$ candidates in data. Stringent requirements are applied to one of the leptons to ensure that it is indeed a lepton, this lepton is called the tag. The second lepton is selected with cuts which are considered unbiased to the efficiency which will be determined. For example if the tracking efficiency is being determined the probe will cannot require a track match, instead different requirements will be used to selected the probe. Once a good tag and probe candidate event is found the probe is tested to see if it passes the selection

of interest. The efficiency ϵ for that selection is the ratio of events which pass the test to the total events which are tested.

The electron efficiencies were determined with EM_CERT [35] and the muon efficiencies were determined with MUO_CERT [34]. These are standard DØ software packages which determine the single lepton efficiencies using the tag and probe method. Each efficiency is found for the kinematic properties it is most dependent on. For example the efficiency for a muon to have a track match is a function of η and the z_{vtx} of the track. The single muon efficiencies are described in Sec. 4.5.3.2 and the single electron efficiencies in Sec. 4.6.2.

4.3 Backgrounds B

There are many background sources which can lead to four lepton final states. The significant background sources arise form QCD jets, top quark production, lepton pairing combinatorics and beam halo.

4.3.1 QCD Jet Backgrounds

The main QCD jet backgrounds, using j to denote a jet, are: Zjj, $Z\gamma j$, $Wjjj$, and $jjjj$. A jet, however, is not a lepton and therefore it must either contain a lepton or fake a lepton to form a reconstructed lepton. Reconstructed electrons inside jets are usually fakes from π_0 decays and photon conversion. Reconstructed muons inside jets, however, are usually real muons arising from prompt B and D meson decays. One exception is hadronic punch through, where a jet is not entirely

contained within the calorimeter and punches through to leave hits in the muon detectors. Muons in side jets can also arise from in flight decays of $\pi^{+/-}$, K_L, or $K^{+/-}$.

Prompt decays followed by in flight decays make up the largest fraction of the real muons produced in QCD jets. In some thin regions of the detectors, hadronic punch through is significant.

The QCD jet background for each channel is determined by first finding the rate at which a jet will produce a reconstructed muon or electron (real or fake). This rate is then applied to events with two leptons and two jets or three leptons and one jet from the data set to determine the QCD background. The electron and muon QCD jet rates and backgrounds are discussed in Sec. 4.6.1.1 and Sec. 4.5.2.1 respectively.

4.3.2 Top quark Backgrounds

Top production at the Tevatron can lead to a four lepton final state through the intermediate state $t\bar{t} \rightarrow W^+W^-b\bar{b}$. The b jets can produce muons and the W bosons can decay to leptons directly or produce leptons inside of jets. The largest background arises from the channel where the b jets produce muons and the W bosons decay to leptons directly. The W bosons are seven times as likely to decay to jets. However, these are general jets without a heavy quark bias and therefore the rate for these jets to produce leptons is tiny in comparison to the greater production rate. Electrons are required to be isolated and at least one

must pass Likelihood > 0.20. Therefore the top background in the *eeee* channel is negligible. However, muons generally do not have an isolation requirement and therefore muons produced from B meson decays must be considered.

The top background was determined using PYTHIA where the W bosons were only allowed to decay to muons for the $\mu\mu\mu\mu$ channel and electrons for the $\mu\mu ee$ channel. The muon and electron geometric and kinematic acceptance was applied as well as the lepton efficiencies. A top cross section of 6.6 pb [20] is used.

B mesons have displaced vertices and therefore can have large impact parameters with respect to the beamspot. The muons are required to pass a tight DCA cut (explained in Sec. 4.5.1.2) which can greatly reduce the top background. PMCS, however, does not model the DCA; therefore, full simulation Monte Carlo was used to determine the ratio of $t\bar{t} \to \mu\mu\mu\mu, \mu\mu ee$ events before and after the DCA cut. The result is that the DCA cut reduces the top background by approximately a factor of three. The final top background in the $\mu\mu\mu\mu$ channel is found to be 0.01 ± 0.005 events. In the $\mu\mu ee$ channel the top background is found to be 0.006 ± 0.003 events. The uncertainty on the number of background events is assigned a value of 50% to account for the uncertainty of the top cross section, the unceratinty from PYTHIA, and the uncertainty on the luminosity.

4.3.3 Lepton Pairing Combinatorics

In the $\mu\mu\mu\mu$ channel and the *eeee* channel there is an ambiguity in which leptons pairs to choose (see Sec. 1.2.1) to form a Z boson pair candidate. Employing

the $M_{i,j}$ to represent invariant mass between the pair of leptons i and j there are three possible invariant mass pairs that can be chosen with four identically flavored leptons (ignoring charge). The event selection in these channels requires that at least one of the following conditions is met:

1. $M_{1,2} > 30$ GeV and $M_{3,4} > 30$ GeV
2. $M_{1,3} > 30$ GeV and $M_{2,4} > 30$ GeV
3. $M_{1,4} > 30$ GeV and $M_{2,3} > 30$ GeV

This allows for the possibility that a $Z\gamma^*$ event can be selected where $M_{\gamma^*} < 30$ GeV but the event is still selected. An illustration can be helpful. Figure 4.2 shows a drawing of a $Z\gamma^* \to \mu\mu\mu\mu$ event[1] with the muons from the Z boson denoted as μ_1 and μ_2 and the leptons from the γ^* denoted as μ_3 and μ_4. Let us assume $M_{1,2} = 93$ GeV and $M_{3,4} = 20$ GeV, and $M_{1,3} = 60$ GeV and $M_{2,4} = 50$ GeV. This event is outside of our acceptance which is defined on the correct Z/γ^* boson pairs with $M_{i,j} > 30$ GeV. However, because one of the Z pairs passes the selection the event is selected. Such events are denoted the combinatorial background. They are real Z/γ^* boson pair events; however, they are outside of how the acceptance is defined.

The combinatorial background is determined from the Monte Carlo event generator by knowing the correct pairs and counting the false pairs that pass the invariant mass cuts when the correct pairs fail. For the $\mu\mu\mu\mu$ channel these events

[1]It is not exactly correct to describe Z^* and γ^* distinctly because of quantum interference, however, this detail is an unnecessary complication for the illustration.

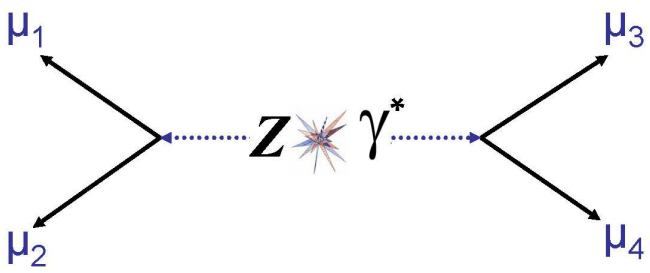

Figure 4.2: Cartoon drawing of a Z boson and γ^* decay.

can be seen in Fig. 4.3. The combinatorial background is found to be 0.016 ± 0.003 events in the $\mu\mu\mu\mu$ channel and 0.015 ± 0.003 events in the $eeee$ channel. The uncertainty was determined by moving the invariant mass cuts to 29 GeV and 31 GeV to account for uncertainties in lepton p_T and η.

4.3.4 Backgrounds Originating Outside of the Beam Pipe

A dirty beam which interacts with matter up stream from the detectors can produce a spray of particles which can leave many hits in the muon detectors and tracking system. This is denoted as beam halo. Additionally, a high energy cosmic ray can produce two reconstructed muons. These backgrounds are easily suppressed by requiring that the track matched to the muon have a DCA close to the beamspot. Beam halo and cosmics arrive random with respect to the beam spot. This is explained in more detail in Sec. 4.5.2.3.

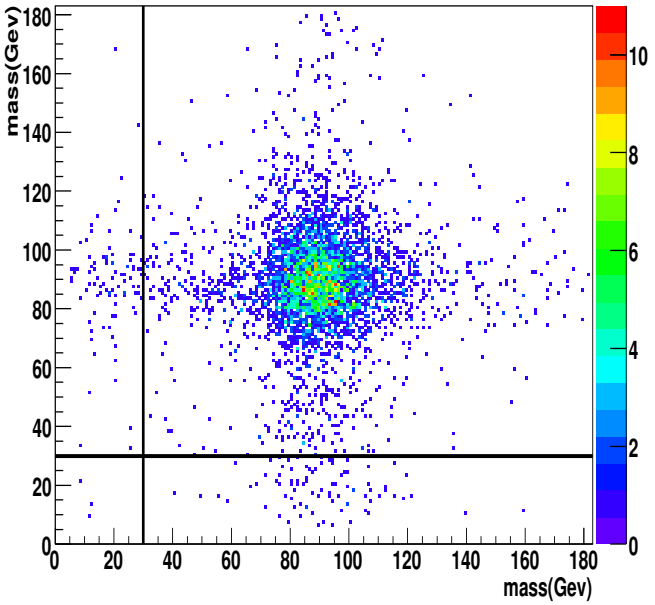

Figure 4.3: $M_{\ell\ell}$ of one Z boson versus $M_{\ell\ell}$ of the other Z boson after selection cuts and smearing. The color intensity represents the number of events per square invariant mass bin. The black lines show the 30 GeV invariant mass cut used to determined the combinatorial background.

4.3.5 Other Physics Backgrounds

Another background source is $Z\gamma\gamma \rightarrow \ell^+\ell^-\gamma\gamma$ with the final state photons faking electrons. The cross section for $Z\gamma\gamma$ is small and both photons have to fake electrons to be a background. The Likelihood selection cut on at least one electrons as well as lepton separation requirements greatly suppresses this background. There is also the quartic gauge coupling $Z^* \rightarrow ZW^+W^- \rightarrow \ell\ell\ell\ell + X$ or $W^* \rightarrow ZZW \rightarrow \ell\ell\ell\ell\ell + X$. However, the cross sections for these processes are negligibly small at the Tevatron.

4.4 Data Set

The data were taken between Oct 2002 and Feb 2006. The trigger list versions range from 8.41 to 14.93. This comprises most of the Run IIa dataset.

Data are not taken continuously during a store, instead the data taking is broken up into runs. A run is a continuous period of data taking. The maximum duration of a run is four hours after which the run is stopped; ideally a new run begins within a few minutes of the last run. Due to many problems during the beginning of Run IIa data taking, run numbers less than 166503 are excluded. A plot of the events that enter the $\mu\mu\mu\mu$ data set versus run number can be seen in Fig. 4.4.

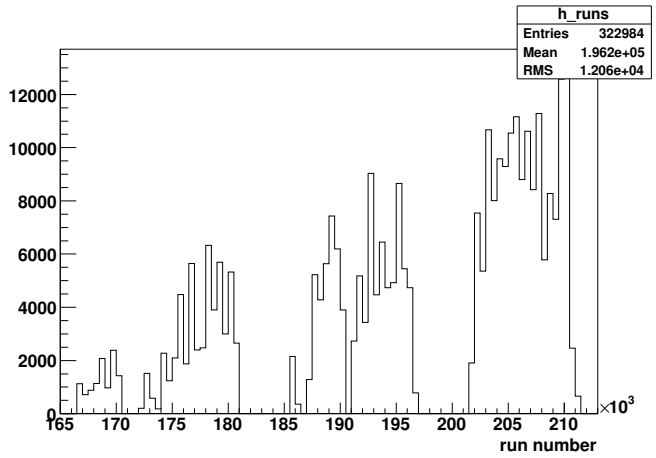

Figure 4.4: Events versus run number in the $\mu\mu\mu\mu$ data set

4.4.1 Hardware Changes

At least two changes were made to the detectors during the collection of the data set. During the Summer 2003 shutdown, C layer scintillators were added in octants the hole region of MUC to increase muon trigger and spatial coverage [29], [30]. The first run after the Summer 2003 shutdown was 184951.

After the Fall 2004 shutdown, the solenoid was unable to attain the previous value of 2 T it ran at and its field was reduced to 1.92 T [33]. The first run after the Fall 2004 shutdown was 201485.

Additionally, the accelerator division in April 2005 installed a device called the flying wire at E0 to measure the beam profile. The wire would "fly" through the beam once an hour per store for a very brief time interval producing a beam halo which flooded the muons system and tracker with many hits [32].

4.4.2 Data Quality

The data were required to pass some quality conditions. Runs that met any of the following conditions were excluded:

- CAL_quality = BAD,
- SMT_quality = not ("GOOD" or "REASONABLE"),
- CFT_quality = not ("GOOD" or "REASONABLE").

Selections that required final state muons also excluded runs with the condition: MUON_quality = not ("GOOD" or "REASONABLE"). Luminosity is measured in blocks of time during a run, if for some reason the luminosity could not be determined during that time then that Luminosity block is removed. Finally, if the calorimeter event quality flags were marked bad those events were also excluded.

4.4.3 Luminosity

Table 4.1 shows the total integrated luminosity for each of the three channels. The luminosity for the *eeee* channel is the largest for two reasons. The electron triggers used were active more often and because no muon detector quality cuts are applied. The luminosity of the $\mu\mu ee$ channel is the next largest because it uses the electrons triggers but applies muon detector quality cuts. The luminosity in the $\mu\mu\mu\mu$ channel is the lowest because it applies both muon and calorimeter quality cuts (for calorimeter isolation) and because the muon triggers used were disabled more often than the electron triggers.

Channel	Luminosity
$\mu\mu\mu\mu$	$(944 \pm 61)\text{pb}^{-1}$
$eeee$	$(1070 \pm 70)\text{pb}^{-1}$
$\mu\mu ee$	$(1020 \pm 66)\text{pb}^{-1}$

Table 4.1: Luminosity for the three different channels

4.5 Four Muon Channel

From a list of reconstructed muons additional selection requirements are done to reduce or remove backgrounds. A brief explanation for each selection cut is given; more details are given later. The selection cuts are:

- All muons are required to have $p_T > 15$ GeV. The p_T from muons from QCD production falls off exponentially, however the p_T of leptons from ZZ production peaks at approximately 45 GeV. Therefore a p_T cut is useful to reduce the QCD background.

- Muons only identified in the A-Layer ($nseg = 1$) are required to have calorimeter isolation less than 2.5 GeV ($iso < 2.5$ GeV), this reduces the hadronic punch-through background.

- To reduce backgrounds from cosmic rays, beam halo, and top quark production, the muons are constrained to be close to the beamspot. For track matches with SMT hits DCA < 0.02 cm, if the track has no SMT hits than DCA < 0.2 cm.

- The scintillator timing at least one of the A, B, or C-layers must be between -10 ns and 20 ns. Scintillator timing helps reduce the cosmic and beam halo background.

Any remaining four muon events are further required to pass cuts based on properties between the muons:

- The difference in the z_{vtx} between all muon pairs must be less than 3 cm ($|\Delta z_{vtx}| < 3$ cm). The z_{vtx} comes from the track match of each muon. This requirement is very effective at removing the beam halo background.

- Each muon pair is also required to have an opening angle α between the muons that is not too small. The requirement is that $\cos(\alpha) < 0.96$. This selection removes the background along the MUC and MUF boundary ($\approx \eta = 1$) where there is fewer interaction lengths and a greater probability of hadronic punch-through

If any four muon events remain, then one last selection cut is done based on invariant mass cuts between muon pairs. By applying invariant mass cuts between muon pairs we can reduce the background from γ^* boson pairs and heavy quark decays. There are three possible Z boson pairs that can be formed from four identical leptons. We label the invariant mass between lepton i and lepton j as $M_{i,j}$. If any one of the three invariant mass conditions in Sec. 4.3.3 is true the event is selected as a final Z boson pair candidate.

4.5.1 Di-muon Studies

Di-lepton events from $p\bar{p} \rightarrow Z/\gamma^* \rightarrow \ell\ell$ are useful to study single lepton properties due to the high statistics (on order 100,000 events). One needs to be careful that the differences between leptons in single Z boson events and ZZ events is taken into account.

4.5.1.1 Muon Only Identified at the A-Layer

Muons identified only at the A-Layer suffer from a large hadronic punch through rate (see Sec. 4.5.2.4). To reduce the hadronic punch through rate we require all $nseg = 1$ muons to have $iso < 2.5$ GeV. Figure 4.5 shows the invariant mass of muon pair events from data where at least one muon was required to have $nseg = 1$ before calorimeter isolation. Figure 4.6 shows an almost identical plot except the $nseg = 1$ muons are required to have $iso < 2.5$ GeV. Note that the calorimeter isolation requirement greatly reduces the background from hadronic punch through.

4.5.1.2 Distance of Closest Approach

The DCA of a track matched to a muons is required to be close to the beamspot. This is done to reduce backgrounds from beam halo, cosmic rays, and top quark events. Tracks with and without SMT hits have significantly different DCA distributions. Figure 4.7 and Figure 4.8 shows the DCA of tracks matched to muons with and without SMT hits. We require that tracks with SMT hits have

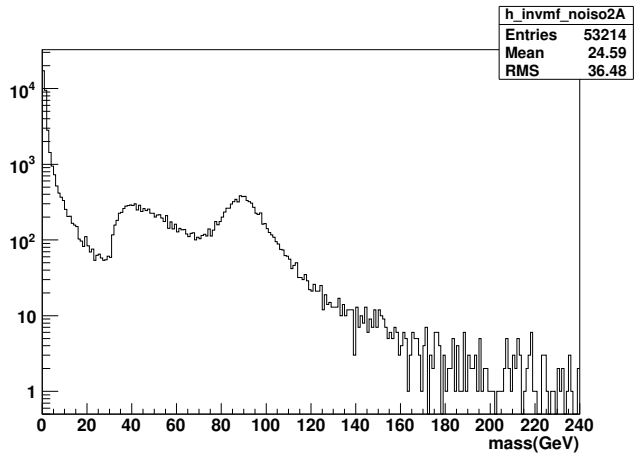

Figure 4.5: $M_{\mu\mu}$ for events with at least one muon with $nseg = 1$.

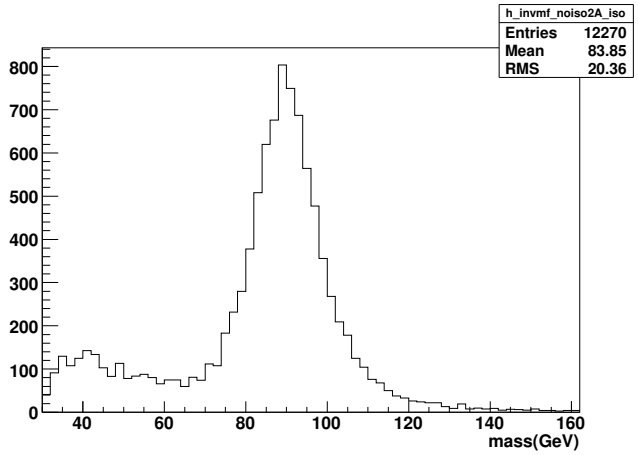

Figure 4.6: $M_{\mu\mu}$ for events with at least one $nseg = 1$ calorimeter isolated muon

DCA < 0.02 cm and tracks without SMT hits to have DCA < 0.2 cm. The invariant mass of di-muon events where at least one muon failed the DCA cut is shown in Fig. 4.9. No signal is visible in this plot. Most of the events in Fig. 4.9 are reconstructed di-muon events from a cosmic ray.

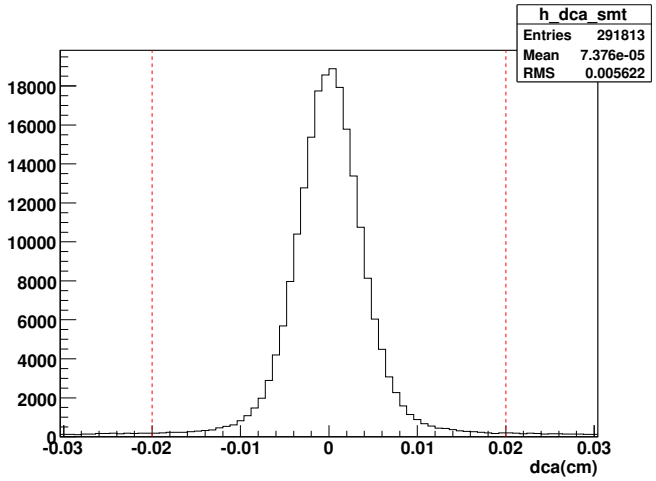

Figure 4.7: DCA for muons with SMT hits after beam-spot correction.

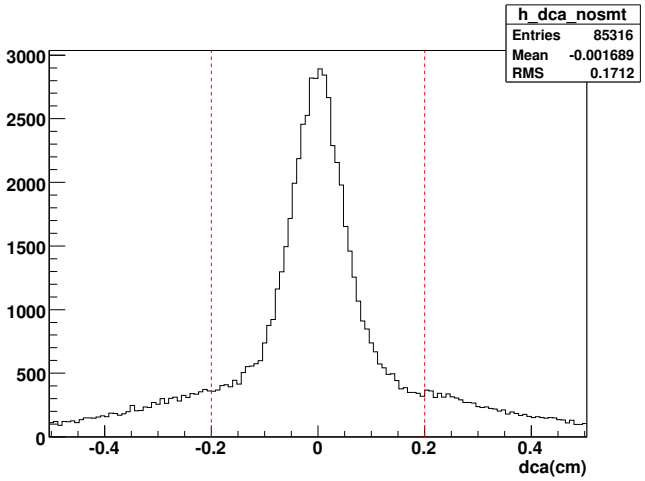

Figure 4.8: DCA for muons without SMT hits after beam-spot correction.

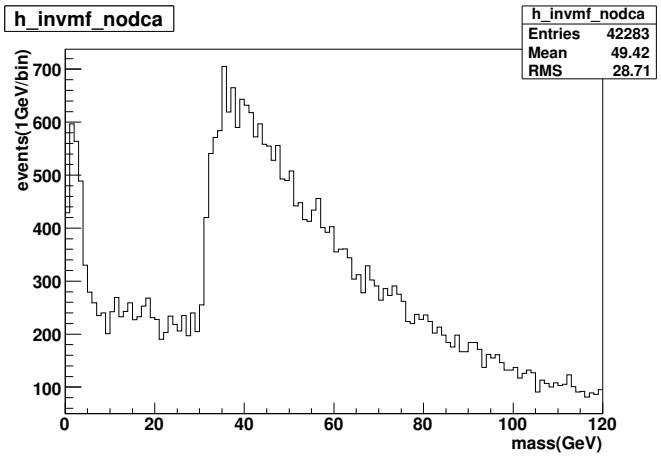

Figure 4.9: $M_{\mu\mu}$ of events that failed the DCA cuts.

4.5.1.3 Scintillator Timing

Scintillator timing can be used to cut a number of backgrounds such as cosmic rays and beam halo (see Sec. 4.5.2.5). The scintillator timing of muons is required to be between -10 ns and 20 ns. Figure 4.10 shows the invariant mass of di-muon events where at least one muon failed the timing cut. Most of the events appear to be background. However a small signal bump can clearly be seen 90 GeV.

4.5.1.4 $\cos(\alpha)$ Selection

Hadronic punch through will be associated with multiple hits in the muon detector inside the cone of a jet. Therefore the opening angle α will be small between multiple muons from hadronic punch through. Instead of determining α between muon pairs we find instead $\cos(\alpha)$ which is easily calculated from the vector

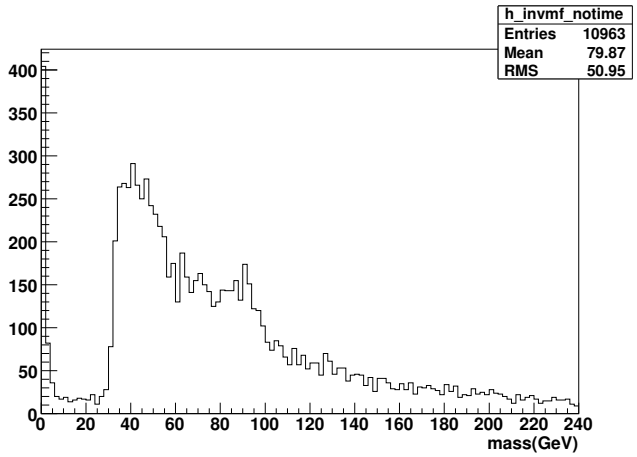

Figure 4.10: $M_{\mu\mu}$ of events that failed timing cuts.

product of the muon momenta $\vec{p1}$ and $\vec{p2}$:

$$\cos(\alpha) = \frac{\vec{p_1} \cdot \vec{p_2}}{|\vec{p_1}||\vec{p_2}|}. \tag{4.5}$$

Figure 4.11 shows the $\cos(\alpha)$ between muon pairs from data. The peak around $\cos(\alpha) \approx 1$ is from hadronic punch through.

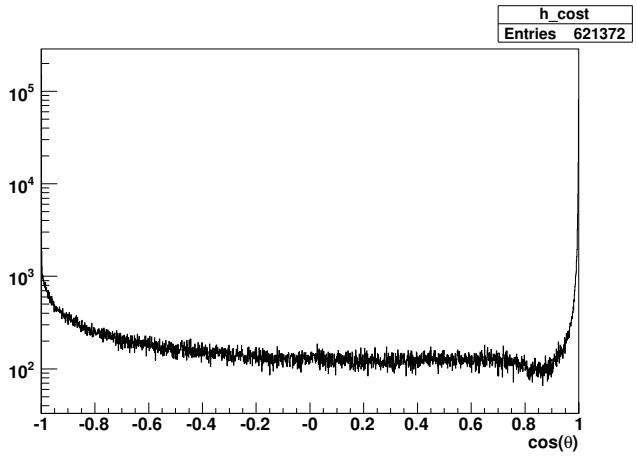

Figure 4.11: $\cos(\alpha)$ between muon pairs

The invariant mass $M_{1,2}$ between two high p_T leptons i and j can be written

as:

$$M_{i,j} = 2E_iE_j(1 - \cos(\alpha)). \tag{4.6}$$

where E_i and E_j are the energies of the two muons. Events with $\cos(\alpha) > 0.96$ will have a small invariant mass. The invariant mass of muon pairs from data which have $\cos(\alpha) > 0.96$ is shown in Fig. 4.12. The peak at low invariant mass is from hadronic punch through. No Z boson signal is visible.

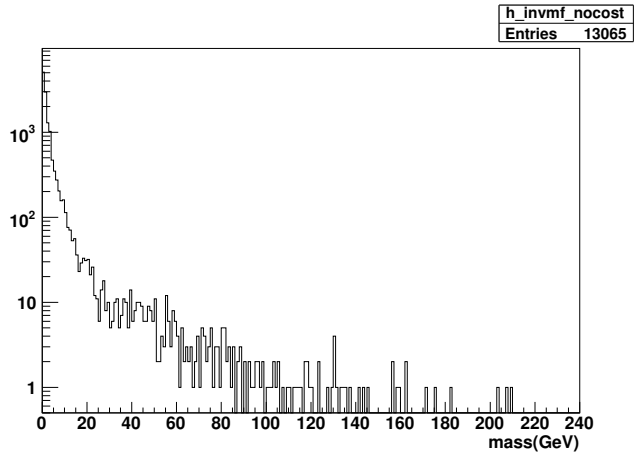

Figure 4.12: $M_{\mu\mu}$ of events that failed $\cos(\alpha)$ cut

4.5.1.5 Δz_{vtx} Selection

The muons in ZZ events should come from the same vertex. Multiple cosmic events or tracks from beam halo will have random vertices, and therefore muons that survive a DCA cut will appear at random z positions. Fig. 4.13 shows the difference in z_{vtx} positions after all cuts but the vertex cut. Almost all of the events have a z_{vtx} difference within 2 cm. For four muons the muons with the maximum and minimum z_{vtx} are found and the absolute value of their difference is required to

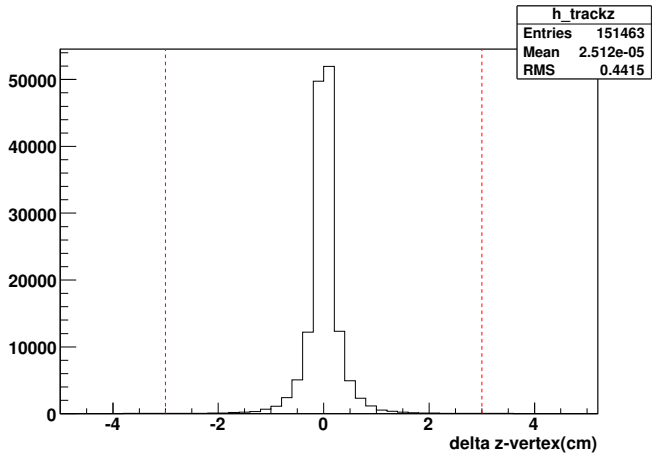

Figure 4.13: z_{vtx} difference.

be less than 3 cm. Fig. 4.14 shows the invariant mass of di-muon events that failed the $|\Delta z_{vtx}| < 3$ cm cut. No signal events are visible.

4.5.2 Backgrounds

The four muon channel does not have backgrounds from photons, however, because of the lack of an isolation requirement on the muons , the four muon channel has a non negligible top background. Muons also have backgrounds from hadronic punch through and beam halo all of which must be considered.

4.5.2.1 QCD Muon Fake Rate

To calculate the backgrounds from jets a rate for jets to produce muons was found. This is called the muon fake rate, though the term muon fake rate is a misnomer as, in fact, the muons are usually real muons produced inside of a jet. The term is more applicable for electron fake rates where the jet usually fakes an

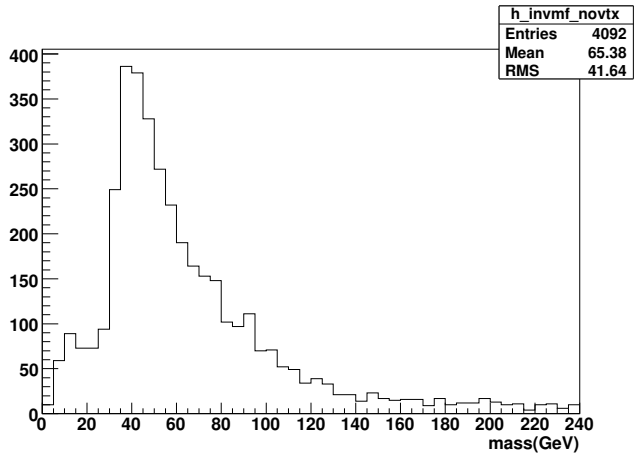

Figure 4.14: $M_{\mu\mu}$ of events that failed vertex cut

electron but no real electron was produced inside the jet.

The muon fake rate was found with a QCD data set selected with the following triggers: JT_8TT, JT_15TT, JT_25TT_NG, JT_45TT, JT_65TT, JT_95TT, or JT_125TT

Events were required to have exactly two jet candidates. No jet energy scale corrections were done. The highest p_T jet was chosen as the tag jet and must pass the following cuts.

- $E_T > 15$,
- $0.05 < f_{EM} < 0.90$,
- $chf < 0.4$,
- $n90 < 1$,
- $hotf < 10$,

The other jet (called the probe) has no additional cuts, however, the tag jet and the probe jet must have $\Delta\phi > 3.0$. All events of this type are filled versus the p_T of the tag jet in a histogram, d. A muon that passes the muon selection cuts is then searched for within a $R < 0.2$ of the probe jet, if one is found a histogram ,n, is filled with the p_T of the tag jet. The muon fake rate is the ratio of the histogram n to the histogram d. The muon fake rate was found as a 2D function of η and p_T. However, it was found the fake rate as a function of p_T is sufficient to determine the QCD jet background.

The muon fake rate is shown in Fig. 4.15 for different selection variations on how close in R the muon had to be to the probe jet and also the MET of the event. The difference in each of these selections with respect to the nominal selection for $R < 0.2$ and no MET cut is shown in Fig. 4.16. These variations are used to asses a 30% systematic uncerertainty to the muon fake rate.

An important point is that the muon fake rate is the probability of a jet of a given p_T to produce a muon with p_T of 15 GeV or greater. The actual p_T of the muon is not known from the fake rate except that muon must have $p_T > 15$ GeV.

Note that the muon fake rate rises linearly and monotonically from $p_T > 15$, this compensates somewhat for the fact that the number of jets found as a function of p_T falls exponentially with p_T.

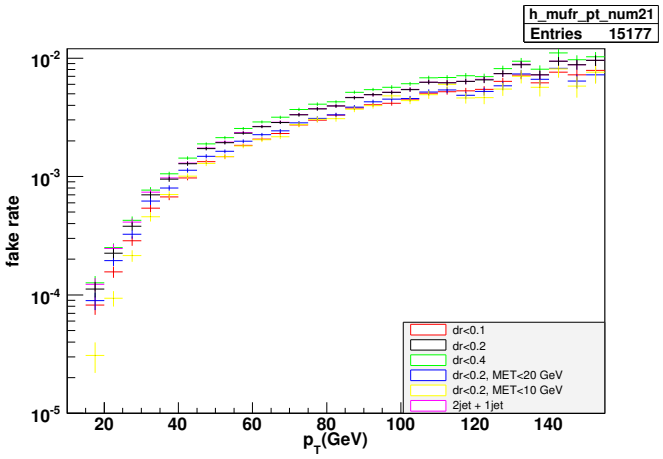

Figure 4.15: Muon fake rate versus jet p_T

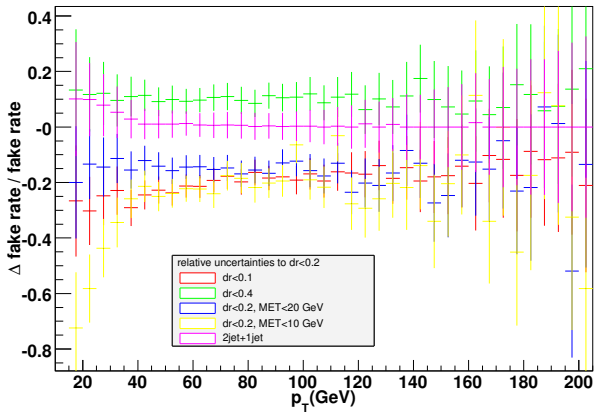

Figure 4.16: Difference in the muon fake rate versus jet p_T with respect to the fake rate that required the muon to be within $R < 0.2$ of the probe jet.

4.5.2.2 Normalization

The QCD jet background contribution from events such as Zjj is determined by finding events with two muons and two jet and applying the muon fake rate to the jets as a function of the p_T of the jets. The total QCD jet background is the sum of the fake rate found for each event. Jet and muons were required to be separated by $R > 0.5$, this was done to avoid double counting for events where a jet already produced a muon.

An event weight is assigned to each event that is found. The background is the sum of all the event weights from each event in the $\mu\mu\mu\mu$ data set.

The total QCD jet background is determined from the $\mu\mu jj$ method to be $0.00315 \pm 0.00007_{stat} \pm 0.0012_{sys}$. The statistical uncertainty is determined by counting the number of $\mu\mu jj$ events and the systematic uncertainty is asserted to be 30% of the background based on the studies of cut variations in determining the fake rate. Additional studies were done using variations on the jet and muon separation and for the fake rate as 2D function of η and p_T. These studies led to backgrounds estimates that were well within the 30% systematic unceratinty assigned to the QCD jet background.

4.5.2.3 Beam Halo

Fig. 4.17 shows the number of four muon events observed before DCA, timing, or Δz_{vtx} selection cuts were applied as a function of run number. Clearly most of these events appear towards the end of the data set. Closer studying of these events

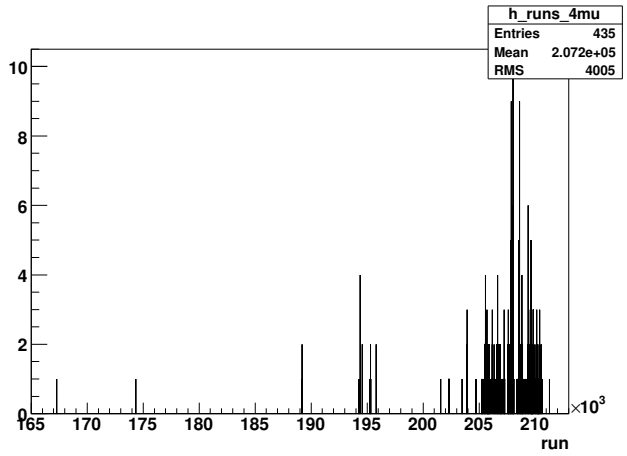

Figure 4.17: Number of four muon events selected before DCA, vtx, or timing cuts versus run

revealed that they often contain 20 or more muon candidates or dozens of tracks above 15 GeV. Graphical event displays of the events looked like a bomb went off in the detector flooding the central tracker as well as the B and C layers of the muon detectors with many hits. However, the calorimeter was usually quiet as well as the A-Layer of the muon system. Most muons were reconstructed as $nseg = 2C$ muons. The fact that there were so many hits in the tracker and muon system increased the probability that random track matches could be matched to muon segments.

The suspect for these events was beam halo. To study this the $fastz$ (see Sec. 2.3.5) of the luminosity counters was used. A proton halo variable is flagged true if $fastz \approx 140$ cm and an anti-proton halo variable is flagged true if $fastz \approx -140$ cm.

Fig. 4.18 shows the proton halo rate versus run number for events with 20 or more muon candidates. The p–halo rate is defined as the number of events where

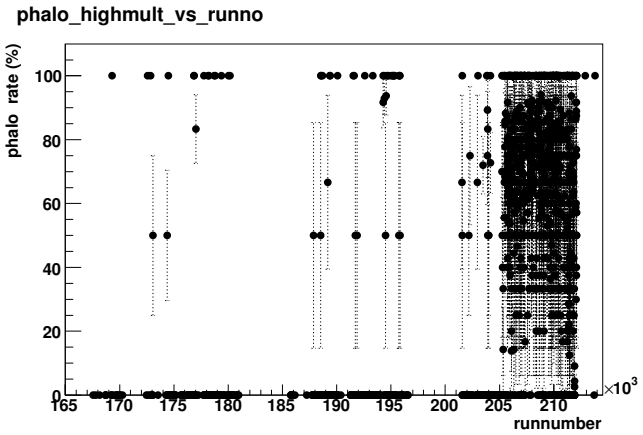

Figure 4.18: Proton halo versus run number for events with 20 or more muon candidates

the proton halo variable is flagged true. If only one event is found in the run and the halo bit is set the rate is 100%.

There is clearly a sharp turn on for the proton halo rates around run 205226. This same effect can be seen in the anti-proton rate and the fastz rate for events with 20 or more muon candidates. The source for most of these halo events has been discovered [32] to be caused by a device installed in the Tevatron in April 2005 called the Flying Wire.

Once every hour the Tevatron measures the beam profile for a short period of time with the Flying Wire device which disturbs the beam and creates a large beam halo.

The beam halo background can be removed by requiring that all muons pass the Δz_{vtx} cut, DCA cuts, and timing cuts.

4.5.2.4 Hadronic Punch Through

Not all hadronic showers are contained within the calorimeter, some showers punch through the calorimeter and can leave hits in the A-layers or even B and C-layers in thin regions. The thin regions of the DØ detector are important to understand because the Likelihood for hadronic punch through is greatest there.

Figure 4.19 shows the number of interaction lengths versus θ of the DØ detector from Run I. Note that there is a thin region at about 40° which corresponds to $\eta \approx 1$; this corresponds to the central and forward toroid boundary, see Fig. 2.4.

There are other thin regions not shown in Fig. 4.19. The Main Ring in Run I passed through the calorimeter and toroid at $\phi = 1.72$ radiants (see Fig. 2.21). In this region the calorimeter is thinner. More importantly, for Run II the hole through the toroid was plugged with concrete which has less interaction lengths than iron.

In order to understand hadronic punch through for this analysis we separate our study into muons which are identified only in the A-layer ($nseg = 1$ muons) and any other muon ($nseg \neq 1$ muons). Muons with $nseg \neq 1$ are muons with both A and BC-layer segments or just BC-layer segments.

Fig 4.20 shows a 2D histogram of the number of $nseg \neq 1$ muon pairs with $\cos(\alpha) > 0.96$ versus η and ϕ. Note the pairs appear along the $\eta \approx 1$ central and forward toroid boundary. Additionally, there are two hot spots at approximately $\phi = 1.7$. These are from the concrete plugs for the Main Ring hole in the forward toroids.

The toroid adds up to five interaction lengths to any hadronic particles which

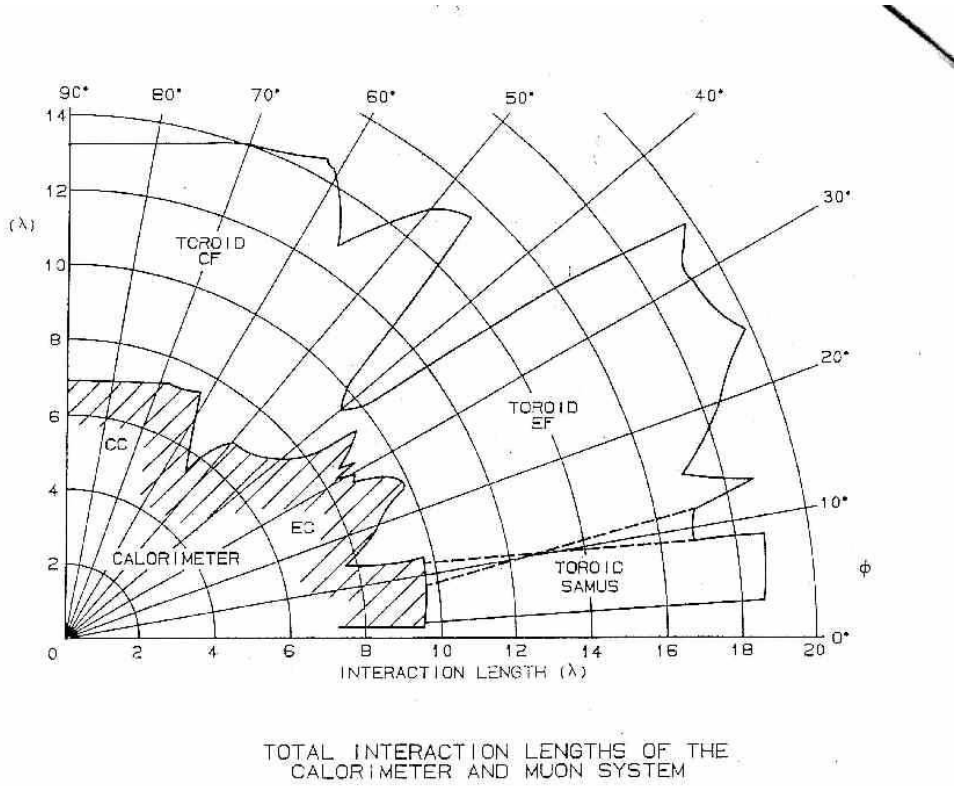

Figure 4.19: Number of interactions lengths versus θ of the DØ detector from Run I.

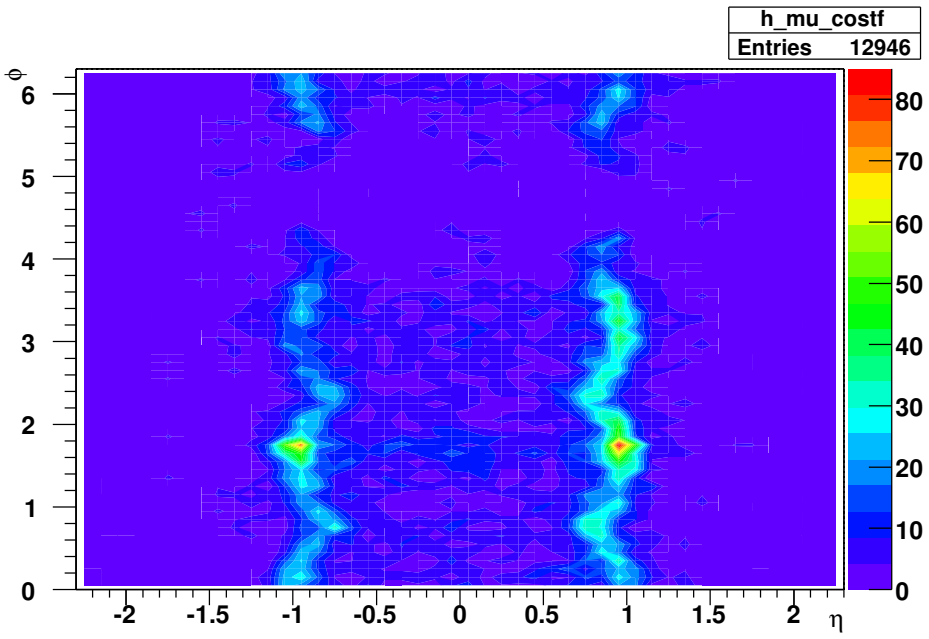

Figure 4.20: η versus ϕ distribution of muon pairs with $\cos\alpha > 0.96$. The events appear mostly along the central and forward toroid boundary. The hot spots at approximately $\phi = 1.7$ and $|\eta| = 1$ are from the Main Ring hole in the forward toroids.

punch through the calorimeter. This effectively eliminates fake muons from hadronic punch through that are identified after the toroid at the B and C layers (except at the toroid central and forward boundary). However, the A-layer of the muon detectors suffers from a large hadronic punch-through rate which must be reduced to identify real muons produced from for example Z boson decays. By requiring that the energy in a annulus around the track of a muon in the calorimeter be less than 2.5 GeV, punch through at the A-Layer is removed.

4.5.2.5 Scintillator Timing

Cosmic rays with high p_T muons enter the muon detectors at random points[2]. One muon from a cosmic rays which passes through the muon detectors will reconstruct as two muons. The path of a cosmic ray is unlikely to pass close to the beamspot. Moreover, to reconstruct four muons in the final state we would need at least two high p_T cosmics both of which must pass near the beamspot to be selected. By requiring that the distance of closest of approach of the track of to be close to the beamspot, we can remove the cosmic ray background.

The timing t for each of the A-Layer scintillators counters is adjusted so that $t = 0$ for that scintillator is the time it would take a muon moving at c to travel from the origin (0,0,0) to that scintillator. The B-Layer and C-layer scintillator counters use a global time subtraction to define $t = 0$. A cosmic ray which enters the top of the detector and exits the bottom of the detector will appear latter in

[2]With the exception of neutrinos, few particles from cosmic rays will be entering the bottom of the detector because of the earth

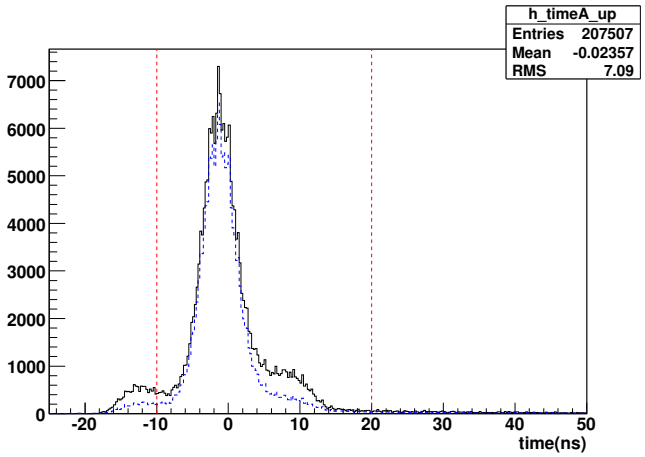

Figure 4.21: Scintillator timing at top A layer before (solid line) and after (dashed line) the DCA cut

time in the bottom scintillator counters. The minimum distance between the A layers is 6 m and the maximum distance is 9 m. In time this is 20 ns to 40 ns. Figure 4.21 shows the scintillator timing for muons with scintillator hits in the top layer of MUC. Figure 4.22 shows the scintillator timing for muons with scintillator hits in the bottom layer of MUC. A bump between 20 ns and 40 ns can clear be seen in the bottom MUC scintillators. The track matches to muons from cosmic rays will also have a poor DCA. Fig 4.23 shows the timing of muons with scintillator hits in both the top and bottom layers which failed the DCA selection. The cosmic rays between 20 ns and 40 ns are quite clear. By applying a timing cut cut of $t < 20\ ns$ we can remove many of the cosmic rays.

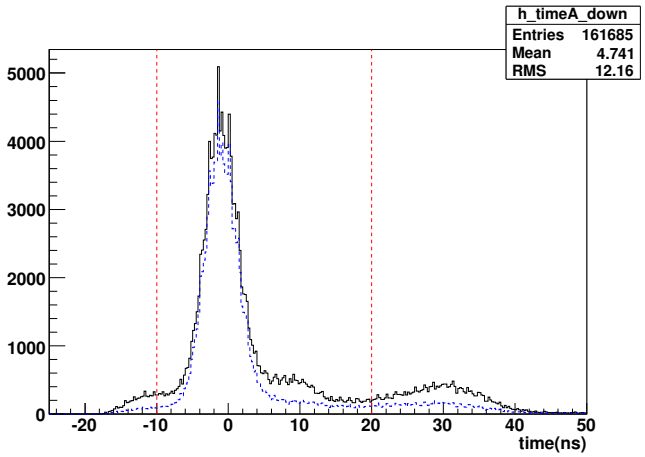

Figure 4.22: Scintillator timing A layer down before (solid line) and after (dashed line) the DCA cut

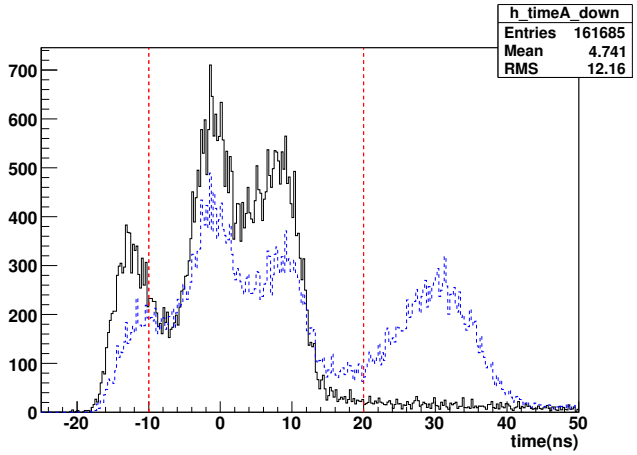

Figure 4.23: Scintillator timing at top (solid line) and bottom (dashed line) A layer that failed the DCA cut

4.5.3 Efficiencies

4.5.3.1 The Muons Detector Geometric Boundaries

As described in Section 2.3.4, the muon detector drift tubes and scintillators were installed in octants for both MUC and MUF. The boundaries between the octants are called the octant gaps. Additionally, for MUC, the drift tubes and scintillators have gaps along z. Finally, at the bottom of the muon detector cube there are supports for the calorimeter. In some areas of this region there is no detector coverage. This is the designated as the muon hole region.

Figure 4.24 shows an z versus ϕ distribution of muons detected in the MUC. Different colors are used to signify the muon types (defined by $nseg$). The octant gaps appear at $\phi = 0.0(6.3),\ 0.8,\ 1.6,\ 2.4,\ 3.1,\ 4.7$, and 5.5. Note that for the A-Layer (shown in red) there are no octant gaps at $\phi = 0.0(6.3)$ and $\phi = 3.1$. The z gaps can clearly be seen $|z| \approx 130$ cm, however, there are no z gaps at the C layer (shown in blue). The most noticeable feature of course is the hole region at $3.92 < \phi < 5.5$. Notice that in this region there is virtually no $nseg = 1$ muons, meaning all muons identified in this region only have one segment in either the A-layer or the BC-layer but not both.

Figure 4.25 shows the x versus y distribution of muons for one side of MUF (the other side has an almost identical distribution) using the same color scheme as Figure 4.24 (compare this with Figure 2.18. The square region at $|x| < 110$ cm and $|y| < 110$ cm where there are very few hits, is from the shielding around the beam pipe (the events which appear in this region come from miscalculation of n_D). This

translates to an η of roughly two which is about the limit of the muon detector. The eight octant gaps can clearly be noticed and are wider than the MUC octant gaps. Additionally, notice that in the region $-300 < y < 270$ there are no $nseg = 3$ muons, this is also the hole region which is mostly covered by A ($nseg = 1$) and B ($nseg = 2B$) layer muons.

The efficiencies were created for implementation into PMCS. The details of how PMCS models the muon acceptance and efficiencies is explained in [36]. The latest version of PMCS includes efficiencies to model the hole region at $3.75 < \phi < 5.65$ in MUC. This definition of the hole region is larger than the previous one to account for the nseg = 1 coverage that extends beyond the old hole definition. The efficiencies for the different nseg regions may each have different efficiencies and so a 2D map was done in this region.

4.5.3.2 Loose Efficiency and Tracking Efficiency

The efficiency for a muon to be identified in the muon detector (have at least one segment in one of the three layers) is denoted loose efficiency. The product of the loose efficiency and tracking efficiency is the reconstructed muon efficiency. Figure 4.26 and Fig. 4.27 shows the loose efficiency for MUC and MUF versus η_D for the regions outside of the octant boundaries and outside of the hole region. The efficiencies inside the octant gaps and on the boundaries of the octant gaps for MUC and MUF can be found in [36]. The efficiency in the hole region was implemented using the 2D map versus z and ϕ shown in Fig. 4.28.

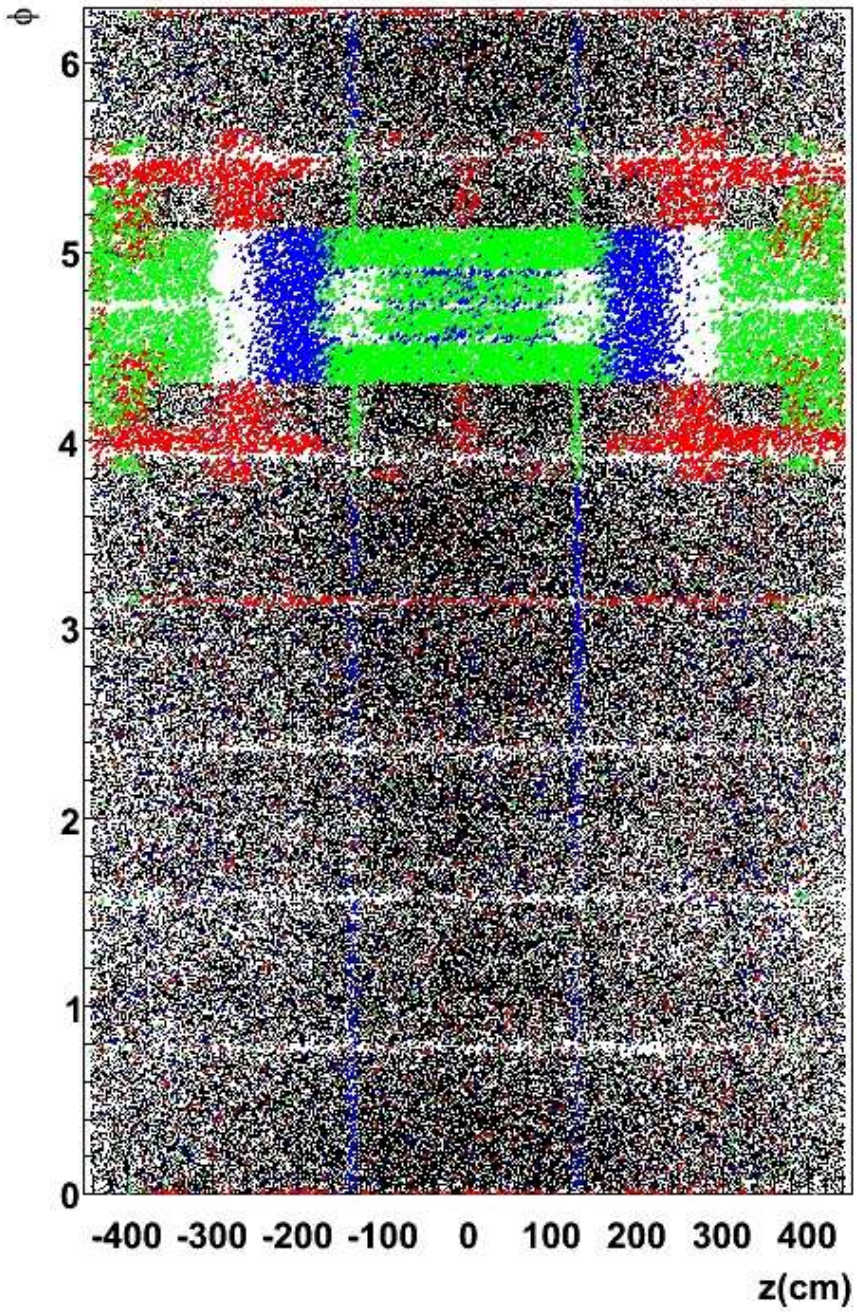

Figure 4.24: z (cm) versus ϕ distribution of muons in MUF. The colors represent $nseg$ of the muons: red for $nseg = 1$, green for $nseg = 2A$, blue for $nseg = 2B$, and black (the most common muon type) for $nseg = 3$

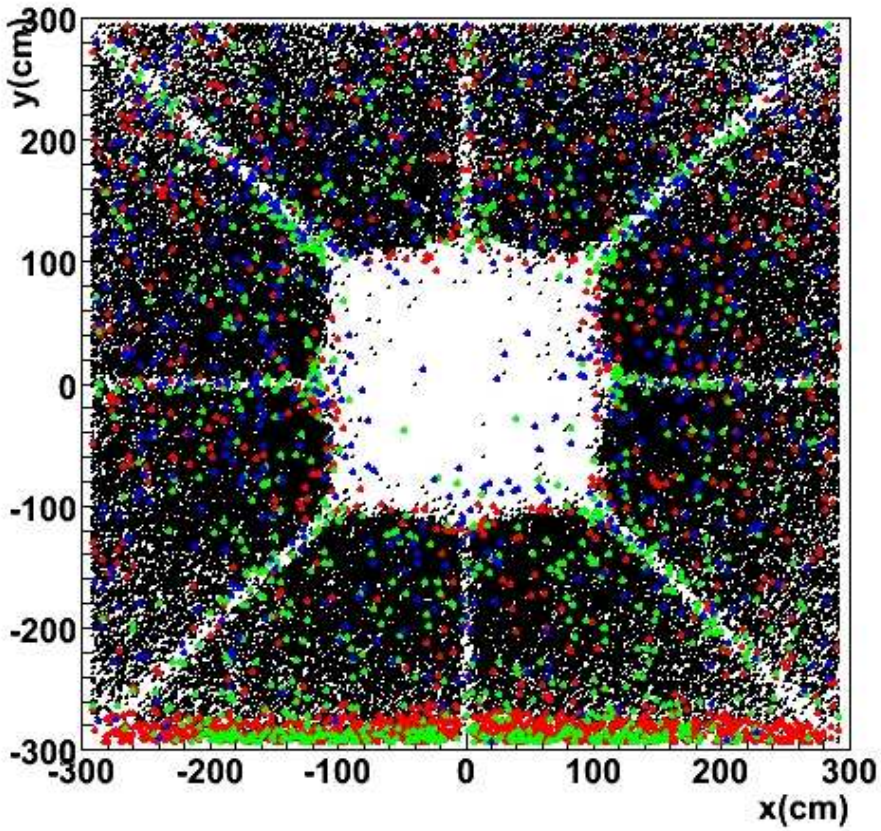

Figure 4.25: x (cm) versus y (cm) distribution of muons in MUF. The colors represent how the muons were identified. Black means the muons were identified from hits both before and after the toroid. Red means the muons were identified only before the toroid. Blue and green means the muons were identified only after the toroid

.

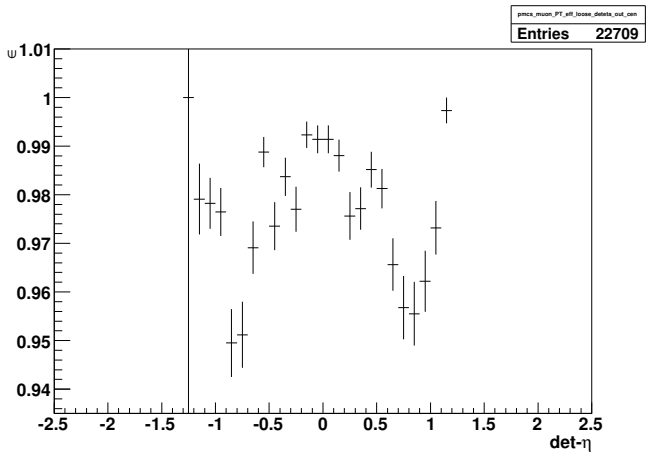

Figure 4.26: Loose Efficiency for MUC out of octant boundary

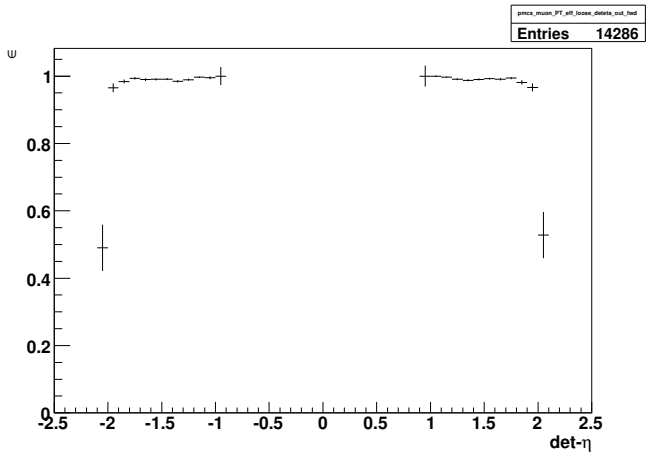

Figure 4.27: Loose Efficiency for MUF out of octant boundary

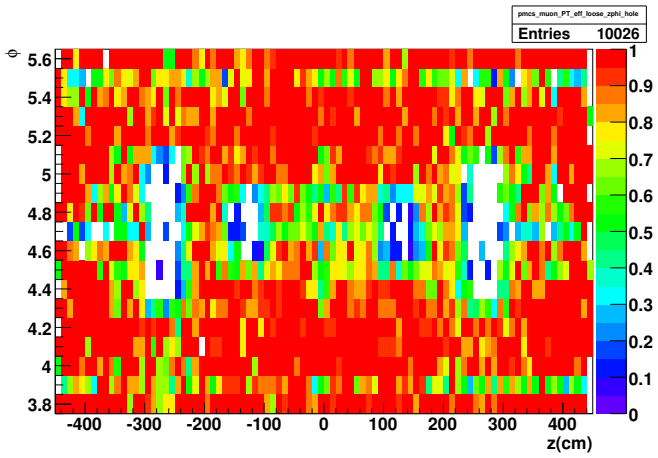

Figure 4.28: Efficiency in the hole region versus z(cm) and ϕ

The average efficiencies in and out of the hole region are given in Table 4.2.

Type	Average loose efficiency(%)
Excluding the hole region	94.5
In hole region only	67

Table 4.2:

PMCS uses five efficiency files to model the tracking system. Each is a different range based on the z_vertex of the track. The ranges are: $z_{vtx} < -39$ cm, -39 cm $< z_{vtx} < -10$ cm, -10 cm $< z_{vtx} <$ 10 cm, 10 cm $< z_{vtx} <$ 39 cm, $z_{vtx} >$ 39 cm. The efficiency for -10 cm $< z <$ 10 cm as a function of η is shown in Fig. 4.29.

4.5.3.3 Other Single Muon Efficiencies

The triggers that were used in the search are given in Table 4.3. Only single muon triggers are used because the efficiency to trigger on at least one of four muons

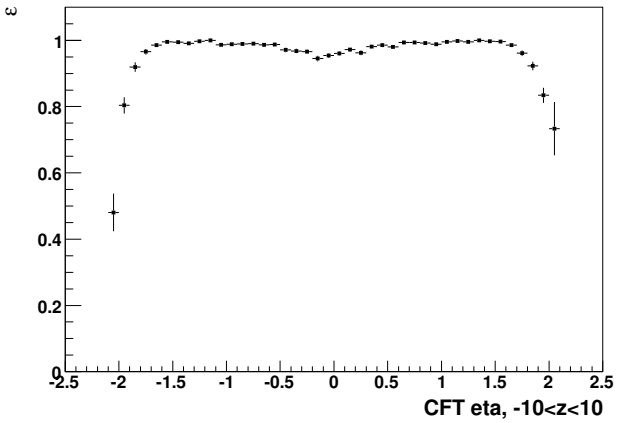

Figure 4.29: Efficiency tracking -10 cm $< z <$ 10 cm

is approximately 100%.

Trigger list	Trigger Name(s)
v8-v10.3	MU_W_L2M5_TRK10
v10.3-v11	MUW_A_L2M3_TRK10
v12	MUW_W_L2M3_TRK10
v13	MUH1_TK12, MUH1_LM15, MUH1_TK12_TLM12

Table 4.3: Muon triggers used in search

The trigger efficiency was found by assuming the trigger efficiency for ZZ is greater than for a WZ di-boson analysis [37] which found the trigger efficiency to be 0.98 ± 0.02. The average average single muon trigger efficiency from this analysis can be inferred to be about 74% as $1 - (1 - 0.74)^3 = 0.98$. Therefore the ZZ muon triggger efficiency is $1 - (1 - 0.74)^4 = 0.99 \pm 0.01$. As an additional check, an event trigger efficiency of only 90% was tried. This implies an average single muon trigger

efficiency of less than 44%. This did not change the final cross section limit for the combined channels or the number of expected signal events in the combined channels. The final result is only weakly sensitive to the trigger efficiency in the $\mu\mu\mu\mu$ channel.

The $\cos(\alpha)$ cut is treated as a geometric acceptance and is measured from Monte Carlo data (see Section 4.5.4.2). The timing, Δz_{vtx}, nseg = 1, and DCA efficiencies are all essential 100% efficicent. The final ZZ efficiency for the for the timing, Δz_{vtx}, nseg = 1, DCA, and charge opposite cuts is 0.993 ± 0.004

4.5.4 Acceptance

4.5.4.1 Geometric Acceptance

There is only one geometric cut applied in PMCS, and this is used to cut out the hole in MUF where the beam-pipe and shielding pass through [36]. The cut implemented in PMCS is $|X_A| > 110$ cm and $|Y_A| > 110$ cm. The hole region in octants 5 and 6 of MUC is treated as part of the loose efficiency and not in the geometric acceptance. The geometric acceptance is given in Table 4.4. For comparison the acceptance with $4.25 < \phi < 5.15$ cut in MUC (the traditional hole region definition) is given and in addition the acceptance for an inclusive Z study is also given.

Table. 4.4 shows that there is a 60% loss for the geometric acceptance for $ZZ \rightarrow \mu\mu\mu\mu$ when the hole region is cut! This justifies the effort that went into studying the hole region to recover acceptance.

Type	Acceptance
no hole region cut in MUC	0.65 ± 0.013
hole region excluded in MUC	0.41 ± 0.01
Single Z boson production [39]	0.47

Table 4.4:

The uncertainty on the geometric acceptance was found by studying by eye the shape of the boundary at $|X_A| > 110$ cm and $|Y_A| > 110$ cm in data. In data this region is not a perfect rectangle and therefore the hole was allowed to vary by ± 5 cm. This gave an uncertainty of 2%. Some of the variance in this boundary seen in data could be due to a mismeassured z_{vtx}, as projecting to the A layer requires the z_{vtx}.

4.5.4.2 Kinematic Acceptance

There are two kinematic cuts: $p_{T\,track} > 15$ GeV and $\cos(\alpha) < 0.96$ between all muon pairs. The kinematic acceptance with variations of the $\cos(\alpha)$ and p_T cut are given in Table 4.5. There is a 15.8% loss in acceptance with a $p_T > 15$ GeV cut compared to a $p_T > 10$ GeV cut. This is an acceptable loss because the jet p_T spectrum falls exponential and so a higher p_T cut removes a large fraction of background for a moderate loss in acceptance.

The uncertainty on the p_T cut was found by assuming an uncertainty on the muon energy scale of ± 0.02 GeV [40]. This corresponds to an uncertainty on the acceptance of less than 0.2%.

The uncertainty on the $\cos(\alpha)$ cut was determined by assuming uncertainties on η and ϕ of of 0.003 and 0.001 [25] respectively. These uncertainties in effect move the $\cos(\alpha)$ cut to $0.960\pm < 0.002$. This gives an uncertainty of less than 0.5%.

Type	Acceptance
$p_T > 10$ GeV	0.9427
$p_T > 15$ GeV	0.804 ± 0.002
$p_T > 20$ GeV	0.644
$\cos(\alpha) < 0.96$	0.923 ± 0.005
$\cos(\alpha) < 0.97$	0.944 ± 0.005
$\cos(\alpha) < 0.98$	0.964 ± 0.005

Table 4.5:

4.5.4.3 Lepton Identification

The ZZ efficiencies uncertainty was found by defining an event uncertainty using the propagation of uncertainty formula and summing the event uncertainty and then dividing by the total number of event uncertainties found. The event uncertainty is defined to be:

$$\delta\epsilon_{event} = \epsilon_1\epsilon_2\epsilon_3\epsilon_4\sqrt{(\frac{\delta\epsilon_1}{\epsilon_1})^2 + (\frac{\delta\epsilon_2}{\epsilon_2})^2 + (\frac{\delta\epsilon_3}{\epsilon_3})^2 + (\frac{\delta\epsilon_4}{\epsilon_4})^2} \tag{4.7}$$

where ϵ_i and $\delta\epsilon_i$ are the efficiency and uncertainty on the efficiency for the i–th muon in terms their relevant variables (η_D,ϕ,η_{CFT},z_{vtx}).

The ZZ loose efficiency is found to be 0.700 ± 0.054 and has the largest uncertainty of all the cuts (7%). As a cross check, the average uncertainty of the loose efficiency per muon was about 3% and the effect of the loose efficiency on the ZZ acceptance should lead to uncertainty of about $\sqrt{4 * 0.03^2} = 0.06$ using error propagation. The uncertainty is large due to the inclusion of the hole region which typically has a single muon efficiency uncertainty of 10%. The ZZ track efficiency is found to be 0.83 ± 0.016, the uncertainty being about 2%. The average single muon tracking uncertainty is about 1% and therefore the is expected to be about 2%. A summary of the acceptances for each cuts is given in Table 4.6.

Selection	Exclusive Acceptance	Cumulative Acceptance
geometric	0.650 ± 0.013	0.650 ± 0.013
$p_T > 15$ GeV	0.804 ± 0.002	0.523 ± 0.011
$cos(\alpha) < 0.96$	0.923 ± 0.005	0.482 ± 0.010
track match	0.830 ± 0.016	0.400 ± 0.011
loose	0.700 ± 0.054	0.280 ± 0.023
DCA, $\lvert\Delta z_{vtx}\rvert$, timing, nseg = 1	0.993 ± 0.004	0.278 ± 0.023
trigger	0.990 ± 0.010	0.276 ± 0.023
total		0.276 ± 0.023

Table 4.6: Summary of acceptance with uncertainties of each cut

If the hole region had been cut and muon isolation had been required (on each muon) the acceptance would only have been about 0.11. That is a factor 2.5 lower

than the current acceptance.

In addition to the lepton cuts, the z_{vtx} distribution of the events can affect the final acceptance. The z_{vtx} does not have a constant distribution. A well focused beam has a tighter distribution than a less focused beam. Additionally as a store progresses the beam degrades and the vertex distribution broadens. Figure 4.30 shows the z_{vtx} of inclusive Z events for the complete muon data set. A Gaussian fit has a width of about 26 cm but is a rather poor fit particularity near 0 cm and at the tails. Figure 4.31 shows the same z_{vtx} data with a fit to a double Gaussian. The double Gaussian fits the data better. The widths of the two Gaussians are about 17 cm and 31 cm. For a more complete discussion of the z_{vtx} as a function of different luminosities see [42] and [41].

PMCS calculates the z_{vtx} by choosing a random number from a z_{vtx} distribution taken from an early subset of the complete data set. A Gaussian fit to the PMCS distribution fits well and has a width of about 24.5 cm. The z_{vtx} is needed in determining the detector η of muons and tracks. Detector η is needed for the geometric cut in MUF and the loose and tracking efficiency . In addition the z_{vtx} is needed for the five z_{vtx} bins of the tracking efficiency.

The difference in the default PMCS distribution and the distribution from a double Gaussian fit to the complete data set was found to differ by 1.2%.

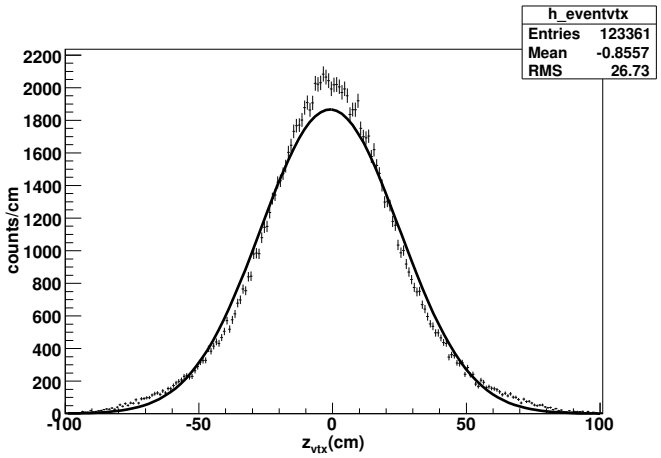

Figure 4.30: z_{vtx} of the inclusive Z events over the full data set. The solid line is Gaussian fit with width of about 26 cm.

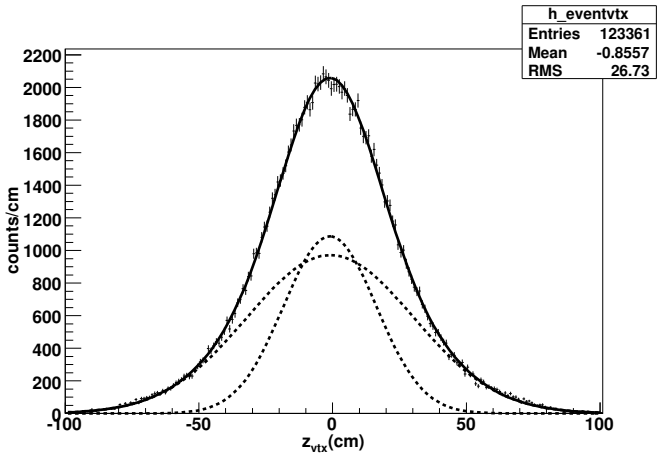

Figure 4.31: z_{vtx} of the inclusive Z events over the full data set. The solid line is a double Gaussian fit to the data. The two dashed lines are Gaussians of the double Gaussian fit and have widths of about 17 cm and 31 cm.

4.6 The Four Electron Channel

We will now discuss the *eeee* channel. Reconstructed electrons are required to have $p_T > 15$ GeV. Additionally, they must have $|\eta_D| < 1.1$ or $1.5 < |\eta_D| < 3.2$. If four electrons are found then at least three out of four of them must have Likelihood > 0.2. If one electron has Likelihood < 0.2 then that muon must have $hmx7 < 12.0$ if $|\eta_D| < 1.1$ or $hmx8 < 20.0$ if $1.5 < |\eta_D| < 3.2$.

The mixed Likelihood and H–Matrix selection is done to improve the event efficiency in the forward regions where the Likelihood efficiency is poor and the H–Matrix efficiency is better (see Sec. 4.6.2.2 and Sec. 4.6.2.3).

Similar to the $\mu\mu\mu\mu$ channel, the *eeee* channel has three possible Z boson pairs that can be formed from four identical leptons. At least one Z boson pair must pass the same invariant mass cuts as in the $\mu\mu\mu\mu$ channel.

4.6.1 Backgrounds

The four electron channel has the same QCD jet production processes as as background as the four muon channel (see section 4.6.1.) However, electrons differ from muons in that a electron found in a QCD jet is usually a fake from π^0 decays and/or photon conversion whereas for muons the jet often produces a real muon originating from bottom or charm quarks. Electrons do not have the cosmic or beam halo background that muons have. Nor do electrons have the background from top quark production as the electrons in b-jets will fail the electron isolation cut and the Likelihood selection. However, the four electron channel does have additional

sources of QCD jet background from $Z\gamma j$. The four electron channel suffers from the same combinatorial background as the four muon channel arising from the inability to distinguish identically flavored leptons with the same charge. Fortunately, the additional background involving final state photons can be determined by finding the rate for a jet to fake an electron (called the fake rate) and applying that fake rate to events with three electrons and one jet.

4.6.1.1 Electron Fake Rates

In order to find the backgrounds arising from QCD jets, the probability for a jet to fake an electron was determined. Because of the mixed event selection, only three out of four of the electrons have to pass the Likelihood > 0.20 different fake rates are necessary to determine the total QCD jet background contribution. The following fake rates were found:

- The fake rate for a jet to pass preselection
- The fake rate for a jet that passed preselection to pass Likelihood > 0.20
- The fake rate for a jet that passed preselection to fail Likelihood > 0.20 but pass the electron H-Matrix cut.

The electron fake rates are determined with a similar method as the muon fake rate. A QCD skim is used with the same jet triggers as the muon fake rate. Events with exactly two jets are selection. The highest p_T jet is defined to be the tag and pass the same tag requirements as for muons. The tag jet and probe yet are

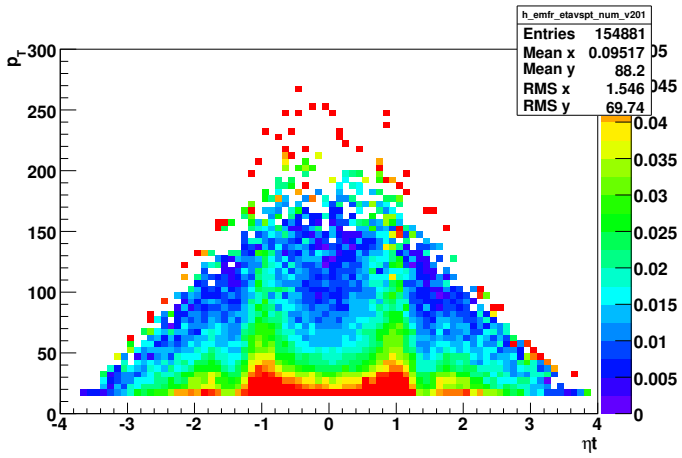

Figure 4.32: Electron fake rate versus η_D and p_T for jets to pass preselection

required to be separated by $\Delta\phi > 3.0$. An electron is searched for within a $R < 0.5$ of the probe jet, if one it is found a histogram n and a histogram d are filled with the η and p_T of the electron, otherwise the histogram d is filled with the η and p_t of the probe jet.

The fake rate for a jet to pass preselection is shown versus η_D and p_T in Fig. 4.32. The fake rate for a jet to pass preselection can be as much as 5%. The fake rate for a jet that already passed preselection to pass Likelihood > 0.20 is shown versus p_T in Fig. 4.33 and versus *eta* in Fig. 4.34, there were too few jets to find this fake rate as 2D function of η and p_T. The η dependence is the strongest and therefore it is the one that is used in determining the background. Note that the fake rate for a jet that passed preselection to pass Likelihood is about 1%. The fake rate to pass preselection and then pass likelihood is on the order of 10^{-4}. The fake rate for a jet that passed preselection to fail the Likelihood but pass the H-Matrix requirement is shown versus η and p_T in Fig. 4.35.

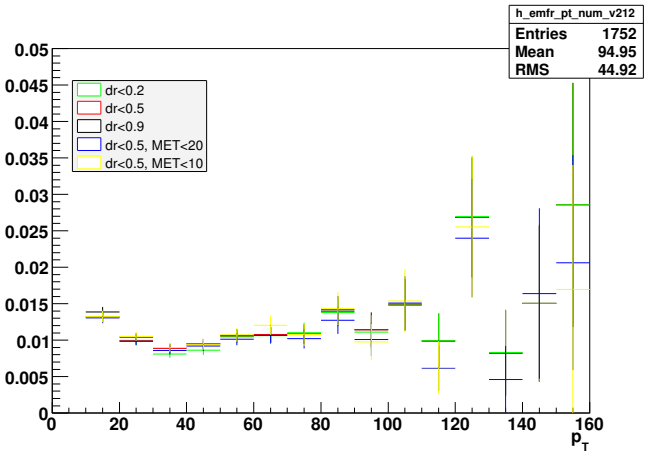

Figure 4.33: Electron fake rate versus p_T for electrons that passed preselection to pass Likelihood > 0.20

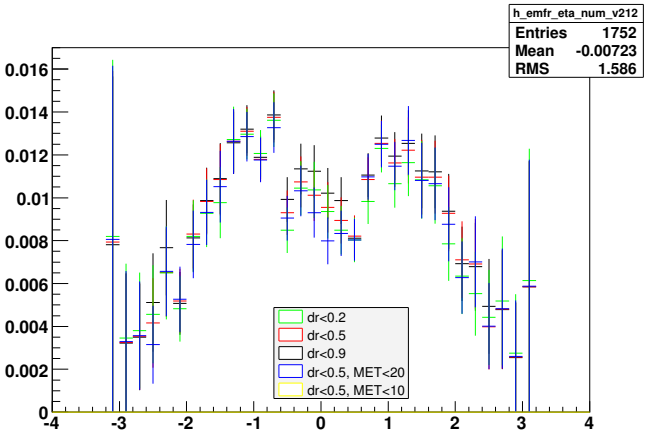

Figure 4.34: Electron fake rate versus η_D for electrons that passed preselection to pass Likelihood > 0.20

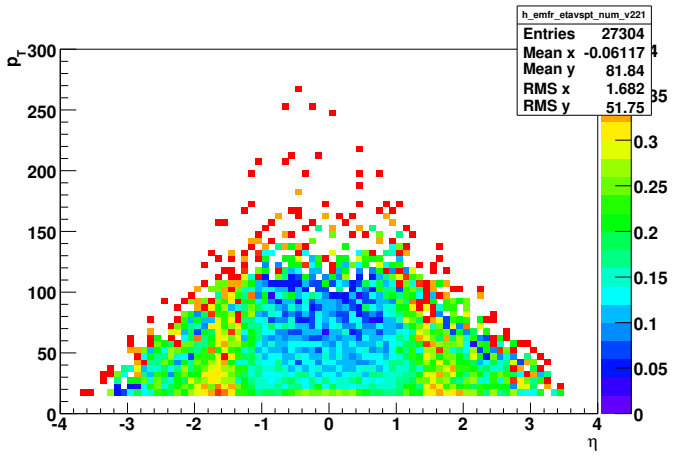

Figure 4.35: Electron fake rate versus η_D and p_T for jets that passed preselection to fail Likelihood > 0.20 but pass the H-Matrix cut

4.6.1.2 The QCD Jet Background

The event selection in the *eeee* channel allows events where one electron fails the Likelihood cut but passes the H-Matrix cut. This is done because there are regions in η_D and z_{vtx} space that have poor or no tracking coverage and an electron that goes into one of these regions is likely to fail the Likelihood cut. However, allowing an electron that does not have a track match introduces a background from $Z\gamma j$ events. In order to determine this background events with three electron candidates are found and one jet and an appropriate electron fake rate is applied to this jet. This sample will include Zjj and $Z\gamma j$ events. The other method that was tried was one based on events with two electron and two jets but this method cannot properly account for the $Z\gamma j$ background.

The QCD jet background is found for two different selection, one requiring that at least three electrons pass the Likelihood cut and if one fails it must pass the

H-matrix cut, this is called the 3/4h selection, the other selection requires that all four electrons pass the Likelihood cut, this is called the 4/4 selection. This is done to determine which selection will gives the best significance.

The appropriate electron fake rate to apply to each jet depends on the type of electrons that are found. In the 3/4h selection, many of the electrons that are found have two electrons that pass the Likelihood cut and one that fails it but passes an H-Matrix selection. In this case, the electron fake rate to pass preselection followed by the Likelihood cut is used. The summary of the event weights for each selection can be found in Appendix D. The QCD jet background for the 3/4h selection is found to be 0.065 ± 0.021 and for the 4/4 selection 0.0012 ± 0.0006.

The only other background that enters the four electron channel is the combinatorial background, this was determined from MC to be 0.015 ± 0.003 for the 3/4h selection and 0.0135 ± 0.001 for the 4/4 selection. A final summary of the QCD jet and combinatorial backgrounds for each selection is given in Table 4.7.

Type	background events
QCD jets 3/4h	0.065 ± 0.021
Combinatorics 3/4h	0.015 ± 0.003
Total 3/4h	0.08 ± 0.03
QCD jets 4/4	0.0012 ± 0.0006
Combinatorics 4/4	0.013 ± 0.001
Total 4/4	0.015 ± 0.014

Table 4.7: Summary of the backgrounds in the *eeee* channel.

4.6.2 Efficiencies

The preselection efficiency and Likelihood efficiency were determined using em_cert over the full dataset. The H-Matrix efficiency cut was determined using a tag and probe method from the full dataset. The Likelihood efficiency is the efficiency for an electron to pass Likelihood > 0.2 given that it passed preselection. The H-matrix efficiency is the efficiency for an electron to pass the H-Matrix cut given that the electron failed the Likelihood cut but passed preselection.

4.6.2.1 Preselection

The preselection efficiency was found using a tag and probe method [42] which required the probe to be a track. In the CC region there are 32 detector modules versus ϕ. A variable called the ϕ_{mod} is defined for each module as $\frac{32}{2\pi n}\phi$, where n is module number starting at zero. The ϕ_{mod} is constrained between zero and one. Many analyses require $0.1 < \phi_{mod} < 0.9$ to remove the regions with reduced coverage at the module boundaries. The preselection efficiency as a function of ϕ_{mod} superimposed for all modules is shown in Fig. 4.36. Note that there is indeed coverage in the ϕ_{mod} boundaries that are usually removed. For this reason no ϕ_{mod} boundary cuts were done on the preselection. This has a noticeable effect on the overall preselection efficiency. With the $0.1 < \phi_{mod} < 0.9$ cut the average preselection efficiency in the CC regions is 99%, however without the ϕ_{mod} cut the average preselection efficiency drops to 96%. However, due to the fact that no ϕ_{mod} cut is done the geometric acceptance in the CC region is increased 20% per electron

which leads to a much larger increase in the ZZ geometric acceptance.

The preselection efficiency as a function of η_D for the CC and EC region is given in Fig. 4.37 and Fig. 4.38. In determining the preselection a track is required. Unfortunately, at large $|\eta_D|$ there is little or no tracking coverage there resulting in very limited statistics to determine the preselection using this method at large $|\eta_D|$. Additionally, the background subtraction done in determining the preselection sometimes causes the efficiency estimate to be larger than 1 (or less than zero). For the EC region the average preselection efficiency for $1.5 < |\eta_D| < 2.5$ was found to be 0.99 ± 0.01, the preselection at higher $|\eta_D|$ where the method to determine the efficiency is not as effective is assumed to also be 0.99 ± 0.01.

The preselection efficiency as a function of p_T for the CC region is given in Fig. 4.39. The p_T dependence in the CC, region for the most part is removed when the $0.1 < \phi_{mod} < 0.9$ is imposed. Within statistics, no p_T dependence in the EC region is observed, most likely because the EC region does not have the ϕ module boundary issues that are found in the CC region.

4.6.2.2 Likelihood

The Likelihood efficiency is the efficiency for an electron to pass Likelihood $>$ 0.20 given that the electron passed the preselection (this is also known as the loose track efficiency). Since the Likelihood cut is strongly dependent on tracking, the Likelihood efficiency was found as a function of η and z_{vtx} and is shown in Fig. 4.40. Note the loss in efficiency at $|\eta| > 2.5$. The empty bins are regions that had no

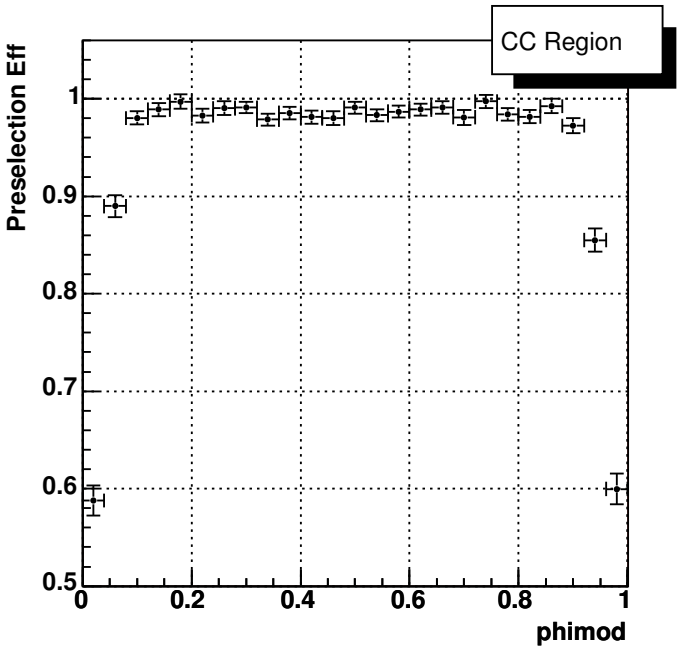

Figure 4.36: Preselection efficiency versus phi-mod

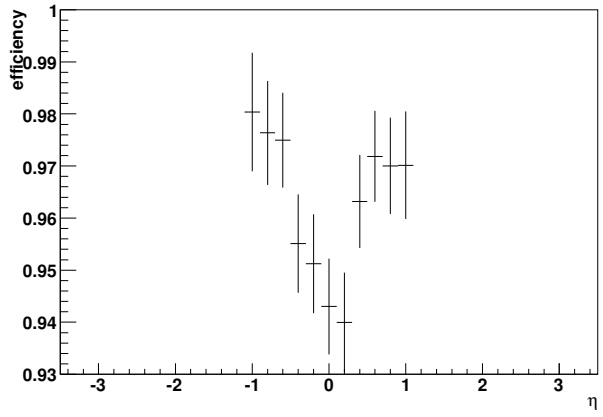

Figure 4.37: CC Preselection efficiency versus η_D

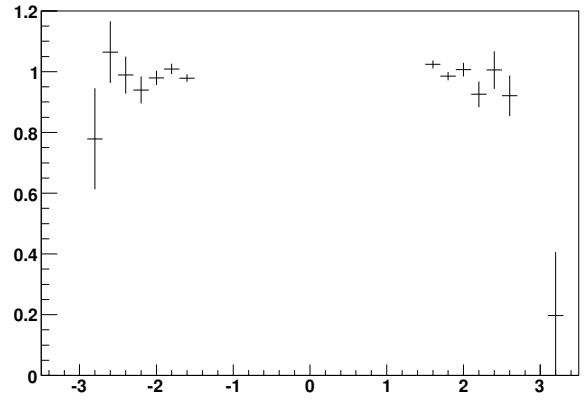

Figure 4.38: EC Preselection efficiency versus η_D

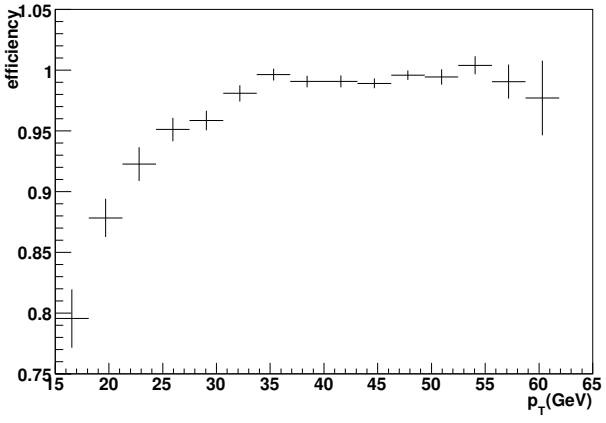

Figure 4.39: CC Preselection efficiency versus p_T

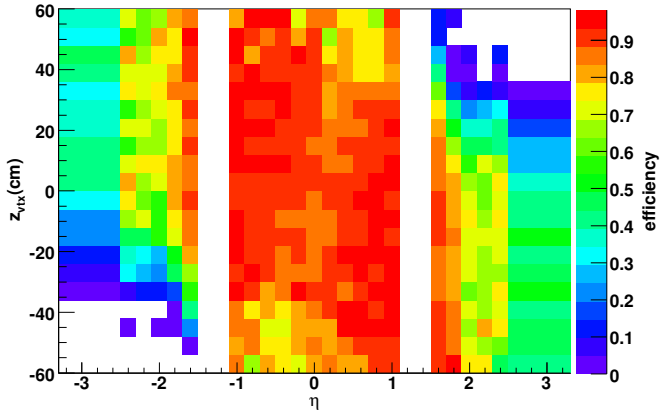

Figure 4.40: Loose Track efficiency versus η_D

data. Tracks with large positive z_{vtx} can be detected at $\eta < -2.5$ and tracks with a large negative z_{vtx} can be detected at $\eta > 2.5$. However, the Likelihood efficiency nevertheless with no data and is still quite low for most of $|\eta| > 2.5$. To improve the electron detection efficiency the H-Matrix cut is used for the electrons that fail the Likelihood cut.

4.6.2.3 H-Matrix

The H-Matrix efficiency has no tracking inputs and therefore does not suffer from the same tracking issues. This efficiency is for an electron to pass the H-Matrix requirement given that the electron failed the Likelihood > 0.2 cut. A tag and probe method was used to find the efficiency. The tag was required to have $p_T > 25$ GeV and Likelihood > 0.85. The invariant mass between the electron pairs was required to between 70 and 110 GeV and the MET of the event less than 25 GeV. The H-Matrix efficiency is shown in Fig. 4.41. The low efficiencies in the CC region are

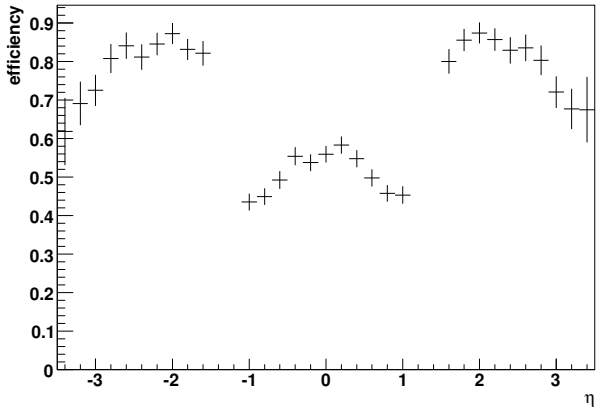

Figure 4.41: H-Matrix efficiency versus η_D

thought to be due to the fact that in the CC region the cut is H-Matrix7 < 12 whereas in the EC the cut is H-Matrix $8 < 20$. Additionally the tracking is quite good in the CC region so an electron that fails Likelihood is more likely to in fact be background and fail H-Matrix. In the CC region there is decent tracking coverage for nearly the entire region. However, for the EC even for $1.5 < |\eta| < 2.5$ there are regions depending on the z_{vtx} where this is no coverage. It is especially in these regions where the H-Matrix is helpful.

4.6.3 Acceptance

4.6.3.1 Geometric and Kinematic

The geometric cuts required the electrons to have $|\eta_D| < 1.1$ or $1.5 < |\eta_D| < 3.2$. This gave an acceptance of 0.49 ± 0.005. For comparison, the acceptance for $|\eta_D| < 2.5$ was found to be 0.49. The acceptance is improved by 16% by including

electrons at $2.5 < |\eta_D| < 3.2$.

Electrons are required to pass an isolation cut. The isolation cut excludes electrons within their core cone of radius 0.2. This efficiency removes electrons that overlap within a R of 0.4. The acceptance loss for this cut was found to be 0.935 ± 0.01. The uncertainty was found by determining what the η and ϕ uncertainties would do the R cut. The R cut was varied by ± 0.0035.

The electrons were required to have $p_T > 15$ GeV which has an effect on the acceptance of 0.76 ± 0.01. All the geometric and kinematic cuts are summarized in Table 4.8.

Type	Acceptance	% uncertainty
Geometric 3.2	0.49 ± 0.005	1%
Geometric 2.5	0.42	
Electron cone cuts	0.935 ± 0.01	1%
p_T	0.76 ± 0.01	1%

Table 4.8: Geometric and Kinematic acceptance

4.6.3.2 Efficiencies

The electron triggers include both di-electron and single-electron triggers. The electron triggers used can be found in [37]. The combination of di-electron and single-electron triggers has an efficiency of 0.99 ± 0.01.

In determining the effect of the preselection efficiency on the ZZ acceptance a

flat efficiency of 0.99 ± 0.01 was used in the EC region. The ZZ acceptance using the preselection efficiency as function of η_D in the EC from the output of em_cert differed from the acceptance using a flat value for the EC region by about 1%.

The effect of the Likelihood cuts on the ZZ acceptance was found for four different selections: 2/4, 3/4, 3/4h, and 4/4. Determining the uncertainty for the 3/4h selection requires special care. What was done was to find the efficiency ϵ_{lk4} for all four electrons to pass Likelihood and the efficiency ϵ_{lk3h} for only three electrons to pass Likelihood given that the one that failed passed the H-Matrix cut. With ϵ_{lk4} and ϵ_{lk3h} the efficiency for the 3/4h ϵ_{lk} cut can be written as:

$$\epsilon_{lk} = \epsilon_{lk4} + (1 - \epsilon_{lk4})\epsilon_{lk3h} = \epsilon_{lk4} + \epsilon_{lk3h} - \epsilon_{lk4}\epsilon_{lk3h} \tag{4.8}$$

By summing the product of the electron efficiencies for many events from Monte Carlo and dividing by the number of events ϵ_{lk4} was found to be 56.7% and ϵ_{lk3h} was found to be 47.9%. The 3/4h efficiency is determined from Eq. 4.8 to be 77.4%. Using the propagation of uncertainty formula on Eq. 4.8 the uncertainty was found to be 4%. A summary of how the efficiencies affected the $ZZ \rightarrow eeee$ acceptance can be found in Table 4.9.

4.6.4 Determining the best event selection

With knowledge of the acceptance and background for each of the selections the most optimal selection can be determined. Table 4.10 gives a list of the acceptance A, the signal S, the background B, and the $S/\sqrt{S+B}$ for each of the selection

type	Acceptance	% uncertainty
Preselection	0.88 ± 0.02	2.3%
2/4	0.99	
3/4	0.89	
3/4h	0.75 ± 0.03	4%
4/4	0.50	
Trigger	0.99 ± 0.01	1%

Table 4.9: The effect of the efficiencies on the $ZZ \rightarrow eeee$ acceptance (also known as the event efficiencies)

.

variations. The 3/4h selection has the largest $S/\sqrt{S+B}$ and therefore it was chosen as the event selection. The uncertainties for each of the $S/\sqrt{S+B}$ values are determined using the uncertainties on the background only because the uncertainties on the backgrounds are much larger than the uncertainties on the signal efficiencies. The number of expected signal event is found to be 0.441 ± 0.036.

4.7 The Two Muon Two Electron Channel

Muons are required to pass the same selection cuts as the $\mu\mu\mu\mu$ channel. This includes the cuts between pairs of muons such as the $\cos(\alpha)$ selection. Electrons are required to pass the same preselection cuts as the *eeee* channel. Both electrons are required to pass Likelihood > 0.2. The tighter requirement on the electrons is done,

Type	A	S	B	$S/\sqrt{S+B}$
3/4h	0.228 ± 0.011	0.441 ± 0.036	0.08 ± 0.03	0.608 ± 0.012
4/4	0.152 ± 0.004	0.294 ± 0.021	0.015 ± 0.014	0.530 ± 0.012

Table 4.10: Event selection summary for the *eeee* channel: A is the final acceptance, S is the signal, and B is the background. The selection with the largest $S/\sqrt{S+B}$ is the 3/4h selection. Only uncertainties on the background are used in determining the uncertainty for $S/\sqrt{S+B}$.

because it was found that the backgrounds with the loose muon selection as well as loose electron selection (allowing one electron to fail Likelihood > 0.2 but pass the H–Matrix requirement) were too large. Due to a background which causes electron and muon spatial overlap muons and electron are required to have the $\Delta R > 0.2$ between them.

4.7.1 Backgrounds

The $ZZ \to \mu\mu ee$ channel has all the same sources of QCD jet backgrounds as the four muon and four electron channels, including those involving final state photons. Additionally top anti–top quark production to two muons and two electrons ($t\bar{t} \to W^+W^- b\bar{b}\mu\mu ee$) is a significant background.

The two muon two electron channel has an additional background not found in the $\mu\mu\mu\mu$ and *eeee* channel which is seen as electron and muon overlap (with separate track matches) and is though be caused by final state photon radiation and/or Bremsstrahlung of photons from muons. This background is removed by

requiring that electrons and muons be spatially separated by the relation $\Delta R > 0.2$.

The two muon two electron channel does not suffer from the combinatorial background as the four muon and four electron channels because there is no issue as to which leptons should be paired. The same muon and electron fake rates are used in determining the background in the $\mu\mu ee$ channel.

4.7.1.1 Normalization

Various methods were tried in determining the QCD jet background. The method that was chosen is called the $\mu\mu ej$ method, these are events with two muons one electron and one jet (where the jet must be separated from the leptons by $R > 0.5$). This method can properly account for $Z\gamma j$ events and is not biased with a large $t\bar{t} \rightarrow \mu\mu ej$ background as the final jet from the top production has a higher p_T on average than a jet in Zjj production. Electron fake rates fall with p_T so the fake rate will be sampled in regions where it is lower.

Two difference selections were tried in order to determine the one with the best significance. The first one requires that at least one of the two electrons pass preselection and if one fails the other must pass the H-Matrix cut. This is called the 1/2h selection, the other selection requires that both electrons pass the Likelihood cut. This is called the 2/2 selection. The QCD jet background for the 1/2h selection is determined to be 0.21 ± 0.02 events and for the 2/2 selection 0.007 ± 0.002 events.

Type	background events
$t\bar{t} \rightarrow ee\mu\mu$	0.006 ± 0.003
QCD jet 1/2h	0.21 ± 0.02
Total 1/2h	0.22 ± 0.02
QCD jet 2/2	0.007 ± 0.002
Total 2/2	0.013 ± 0.005

Table 4.11: Summary of the backgrounds in the $\mu\mu ee$ channel.

4.7.2 Acceptance

The geometric boundaries for muons and electrons are the same as in the four muon and four electron channels. The geometric acceptance was found to be 0.560 ± 0.006. The uncertainty was determined in the same way for the electron and muon channels, by varying the beam-pipe cut in MUF for muons and the ICR cuts for electrons. Due to the fact that each Z produces different leptons, the $\cos(\alpha)$ cut and the electron cone separation cuts don't have a noticeable effect on the geometric acceptance. However, some acceptance is lost because electrons and muons are required to be spatial separated from one another. The uncertainty on the separation of electrons and muons was determined by varying the R cut by ± 0.007. This variation is based on the largest uncertainty in R which is the η uncertainties of electrons (0.0035). The uncertainty on the p_T cut was determined by varying the p_T cut by ± 0.233 which is the largest uncertainties from the electrons in the EC region. Better methods could probably find lower uncertainties, however, the largest

uncertainties in the acceptance come from the efficiencies. A summary of the effect of the geometric and kinematic cuts on the ZZ acceptance is given in Table 4.12.

The same muon loose identification, muon tracking, electron Likelihood, and electron H-Matrix efficiencies are used in determining the $ZZ \to \mu\mu ee$ acceptance. The uncertainties are determined using the propagation of uncertainty formula with the efficiency uncertainty by the same method as for the $\mu\mu\mu\mu$ and $eeee$ channel. The trigger efficiency is assigned a value of 0.99 ± 0.1. A summary of the effect of the efficiencies on the ZZ acceptance is given in Table 4.13.

Once the acceptance, A, is known, the expected number of signal S events can be determined. Additionally, with the background B determined the selection with the best $S/\sqrt{S+B}$ can be found. A summary of the acceptance, signal, background, and $S/\sqrt{S+B}$ for the 1/2+hmx, and 2/2 selections can be found in Table. 4.14. Based on the central values and uncertainties of the $S/\sqrt{S+B}$ of the two selections, the 2/2 selection is chosen to be the final selection for the $\mu\mu ee$ channel (otherwise the backgrounds in the $\mu\mu ee$ channel would dominate over the other channels).

Type	Acceptance
Geometric	0.56 ± 0.006
$cos(\alpha)$+electron cone cuts	1.00 ± 0.00
electron and muon separation	0.982 ± 0.001
p_T	0.78 ± 0.01

Table 4.12: The $\mu\mu ee$ channel - the effect of the geometric and kinematic cuts on the ZZ acceptance

1/2+hmx, muon loose, muon track	0.642 ± 0.046
2/2, muon loose, muon track	0.515 ± 0.044
Trigger	0.99 ± 0.01
DCA, timing, Δz_{vtx}, charge	0.997 ± 0.002

Table 4.13: The $\mu\mu ee$ channel - the effect of the efficiencies on the ZZ acceptance.

Selection	A	S	B	$S/\sqrt{S+B}$
1/2h	0.272 ± 0.020	1.005 ± 0.099	0.22 ± 0.02	0.90 ± 0.01
2/2	0.218 ± 0.019	0.806 ± 0.088	0.013 ± 0.005	0.89 ± 0.01

Table 4.14: The $\mu\mu ee$ channel: acceptance A , signal S , background B, and $S/\sqrt{S+B}$

4.7.3 A Candidate Event

One candidate event was found with run number 208854 and event number 35162371. The invariant mass between the electrons M_{ee} is 93.4 GeV, and between the muons $M_{\mu\mu}$ is 33.4 GeV. Due to the low invariant mass of the muon pair if this event is signal it is more likely to be a $Z\gamma^*$ event and not a ZZ^* event[3].

Table 4.15 gives a list of some of the properties of the leptons and Z bosons in this event. Notice that both electrons have a Likelihood near 0.99 and that both muons have muon_quality = tight (which means they are also nseg = 3 muons).

[3]This assumes that one can uniquely distinguish between a Z^* and a γ^*, the more correct answer is an interference of both states.

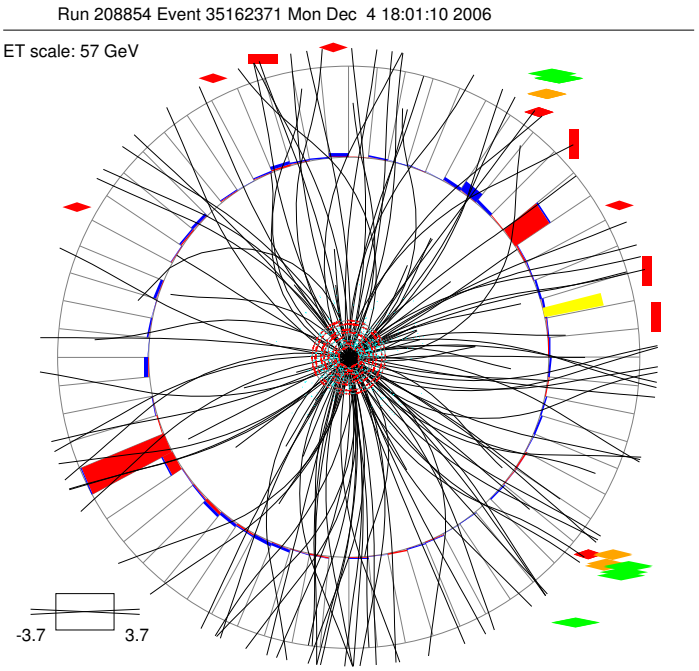

Figure 4.42: Event display of the candidate event with the beam axis into the page ($x - y$ plane).

Additionally, the MET of the event is only 4.6 GeV (after compensating for the two muons). The p_T of both Z bosons are approximately the same and back to back.

Spatial projections into two dimensions of this event in the x-y plane and r-z plane can be found in Fig. 4.42 and Fig. 4.43 respectively. One should be careful not to conclude that any leptons are overlapping from two dimensional projections because in three dimensions all the leptons are separated (as can be seen in Table 4.15).

A plot of the calorimeter occupancy in η-ϕ space is shown in Fig. 4.44. The two electrons can clearly be seen and the rest of the calorimeter is fairly quiet. The MET represented in yellow is not corrected for the two muons, when this is done the MET is only 4.6 GeV.

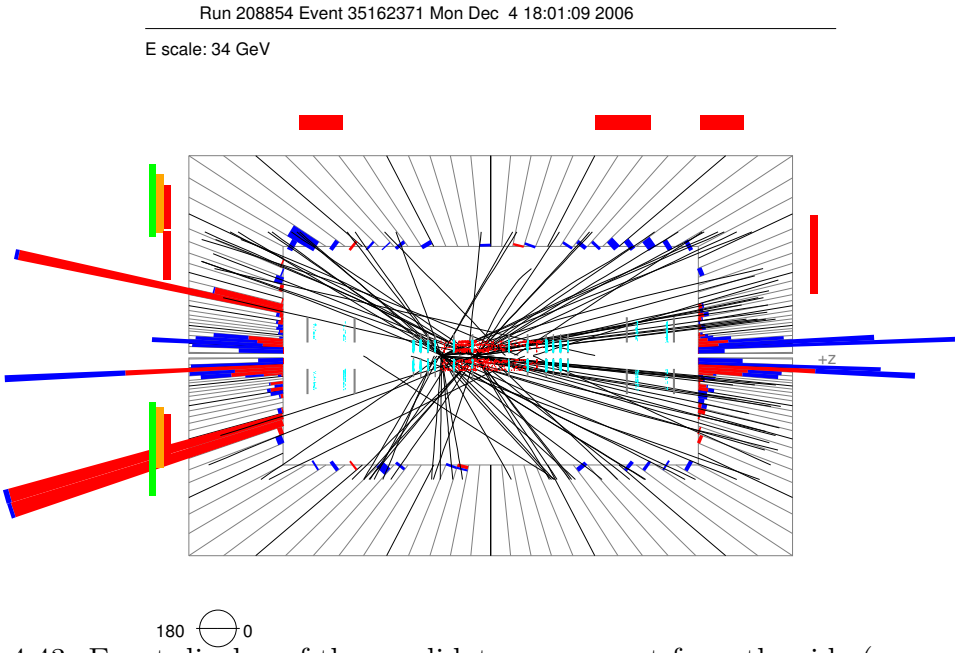

Figure 4.43: Event display of the candidate $\mu\mu ee$ event from the side ($r - z$ plane).

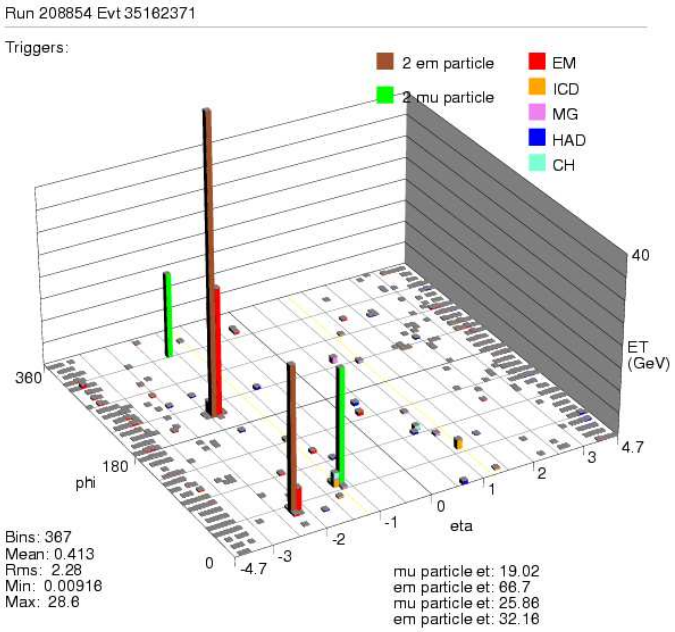

Figure 4.44: Calorimeter occupancy of the candidate $\mu\mu ee$ event

4.8 Results From All Channels and a Limit on the SM Cross Section

The luminosity, acceptance, and background with uncertainties have been determined for each channel. The number of candidate events for each channel has been found. A summary of all these values for each channel can be found in Table 4.16. The total background is simply the sum of the backgrounds in the three channels. To determine the total background uncertainty the background in the $\mu\mu\mu\mu$ channel $B\mu$ is assumed to be uncorrelated with the background Be in the $eeee$ channel. However, the background in the $\mu\mu ee$ channel $B\mu e$ is assumed to be 50% correlated with $B\mu$ and Be. The total uncertainty on the background σ_B is found using the propagation of correlated uncertainties formula to be:

$$\sigma_B^2 = \sigma_{B\mu}^2 + \sigma_{Be}^2 + \sigma_{B\mu e}^2 + 0.5(2\sigma_{B\mu}\sigma_{B\mu e}) + 0.5(2\sigma_{Be}\sigma_{B\mu e}). \tag{4.9}$$

Summing the backgrounds and using Eq. 4.9 the total background is found to be 0.179 ± 0.050.

A cross section limit from the combined channels is determined with the same limit calculator for the individual channels. However, the acceptance is defined to be:

$$A_{comb} = (\alpha A\mu + 2\beta A\mu e + Ae)L_e Br^2 \tag{4.10}$$

where $A\mu$, Ae, and $A\mu e$ are the acceptances for the $\mu\mu\mu\mu$, $eeee$, and $\mu\mu ee$ channels respectively, α is the ratio of the luminosity in the $\mu\mu\mu\mu$ channel to the luminosity in the $eeee$ channel, β is the ratio of the luminosity in the $\mu\mu ee$ channel to the luminosity in the $eeee$ channel, L_e is the luminosity in the $eeee$ channel and Br is the branching ratio for a Z to go to leptons.

The uncertainty of the acceptance for the $\mu\mu\mu\mu$ channel is assumed to be uncorrelated with the uncertainty of acceptance for the *eeee* channel, however, the uncertainty of the acceptance for the $\mu\mu\mu\mu$ channel and the *eeee* channel is assumed to be 50% correlated with the uncertinaty of the acceptance for the $\mu\mu ee$ channel. The luminosities are assumed to be 100% correlated. If A is defined to be Eq. 4.10 but without the L_e term, the uncertainty on the overall acceptance can be written as:

$$(\sigma_{comb}/A_{comb})^2 = (\sigma_A/A)^2 + (\sigma_L/L)^2 \tag{4.11}$$

where L is the luminosity in the *eeee* channel.

The uncertainty σ_A can be written as:

$$(\sigma_A)^2 = Br^4((\alpha\sigma_{A\mu})^2 + (2\beta\sigma_{A\mu e})^2 + (\sigma_{Ae})^2 + 2\alpha\beta\sigma_{A\mu}\sigma_{A\mu e} + 2\beta\sigma_{Ae}\sigma_{A\mu e}). \tag{4.12}$$

With the relevant values for Eq. 4.10 and Eq. 4.11, A_{comb} is determined to be 1.074 ± 0.07. The total signal is found to be 1.7 ± 0.1 and is defined as the sum of the signal from each channel with an uncertainty of A_{comb} times the σ_{ZZ} cross section. One event is observed in the $\mu\mu ee$ channel. The probability for the background to fluctuate to the signal is about 12%. A cross section limit of 4.4 pb at a 95% confidence level.

	e	e	μ_1	μ_2
p_T	66.7 GeV	33.2 GeV	19 GeV	26 GeV
η	-1.88	-2.17	-1.6	-1.2
ϕ	3.62	0.63	5.6	0.91
z_{vtx} from track	-10.31 cm	-10.31 cm	-10.12 cm	-10.57 cm
p_z	-213 GeV	-140 GeV	-46.2 GeV	-38.6 GeV
muon type			tight (nseg = 3)	tight (nseg = 3)
Scintillator time A layer			-3.0 ns	-3.5 ns
smt hits			9	6
charge			1	-1
Likelihood	0.986	0.995		
	Z_{ee}		$Z_{\mu\mu}$	
Boson p_T	35.2 GeV		31.7 GeV	
$p_{x1} + p_{x2}$	-33.2 GeV		30.6 GeV	
$p_{y1} + p_{y2}$	-11.8 GeV		8.6 GeV	
$\cos(\alpha)$	0.86		0.76	
$M_{\ell\ell}$	93.4 GeV		33.4 GeV	
	$ZZ_{\mu\mu ee}$			
MET	4.6 GeV			
4-mass	150 GeV			

Table 4.15: List of various quantities for the $\mu\mu ee$ event

Channel	Luminosity	Acceptance	Background	Signal	N
$\mu\mu\mu\mu$	(944 ± 58) pb^{-1}	0.27 ± 0.02	0.03 ± 0.01	0.46 ± 0.05	0
$eeee$	(1070 ± 65) pb^{-1}	0.23 ± 0.01	0.08 ± 0.03	0.44 ± 0.03	0
$\mu\mu ee$	(1020 ± 62) pb^{-1}	0.22 ± 0.02	0.013 ± 0.005	0.81 ± 0.09	1
Total			0.13 ± 0.03	1.7 ± 0.1	1

Table 4.16: Summary of the luminosity, acceptance, background, signal, and number of candidate events N found for each channel. The total acceptance is defined in Eq. 4.10.

Chapter 5

Neutral Trilinear Gauge Couplings

The $SU(2) \times U(1)$ symmetry of the electroweak terms of the Standard Model allows for tree level trilinear couplings of the gauge bosons (see Sec. 1.1.3). For example, the SM predicts the trilinear couplings of WWZ and $WW\gamma$. However, the SM does not allow for the tree level neutral trilinear gauge couplings . For example ZZZ, $ZZ\gamma$, and $Z\gamma\gamma$ couplings are forbidden since they violate the $SU(2)$ symmetry of the SM.

Neutral trilinear gauge couplings with Z boson pairs in the final state have not been extensively studied at hadron colliders, and any deviation from what is expected in the Standard Model would indicate new physics. Additionally, a sufficiently heavy Higgs boson can decay into Z boson pairs. Distinguishing between anomalous neutral trilinear gauge coupling with Z boson pairs and Higgs boson decays into Z boson pairs may be important.

There are two classes of neutral trilinear gauge coupling structures that preserve Lorentz invariance and $U(1)$ gauge invariance (but break $SU(2)$ symmetry). One class involves an on-shell Z boson and a real photon in the final state such as $Z\gamma Z^*$ and $Z\gamma\gamma^*$. These neutral trilinear couplings are parametrized by the eight couplings h_i^V for $i = 1, 2, 3, 4$ and $V = Z, \gamma$. The other class of neutral trilinear couplings have Z boson pairs in the final state such as ZZZ^* and $ZZ\gamma^*$. These

neutral trilinear couplings are parameterized by the four couplings f_i^V for $i = 4, 5$ and $V = Z, \gamma$. This analysis studies the f_i^V couplings; a study of the h_i^V couplings can be found in [43].

The most general Lagrangian which preserves Lorentz invariance and $U(1)$ gauge invariance that describes the neutral trilinear coupling ZZV can be written as [44]:

$$\mathscr{L} = \sum_{V=Z,\gamma} -\frac{e}{M_Z^2}[f_4^V(\partial_\mu V^{\mu\beta})Z_\alpha(\partial^\alpha Z_\beta) + f_5^V(\partial^\sigma V_{\sigma\mu})\widetilde{Z}^{\mu\beta}Z_\beta] \tag{5.1}$$

where V represents an an off-shell Z/γ boson, $V_{\mu\nu} = \partial_\mu V_\nu - \partial_\nu V_\mu$ and $\widetilde{Z}^{\mu\beta} = \frac{1}{2}\epsilon_{\mu\nu\rho\sigma}Z^{\rho\sigma}$. All couplings violate C invariance, additionally, f_4^V violates CP invariance and f_5^V violates P but conserves CP invariance.

Additional couplings parameters exist if the either or both of the final state Z bosons are allowed to be off-shell, however these couplings are highly suppressed [45]. In the SM at tree level all the f_i^V couplings are zero. The f_5^V coupling does have a one loop contribution on order 10^{-4} [44] and the f_4^V coupling has an even smaller two loop contribution. Figure 5.1 shows the tree level SM ZZ and anomalous ZZV Feynman diagrams.

The f_i^V couplings grow with $\hat{s}$. S-matrix unitarity restricts the couplings to their Standard Model values at large energies. Therefore, the couplings must have a momentum dependent form factor. To parametrize the dependence of the f_i^V couplings on $\hat{s}$ a dipole form factors is chosen:

$$f_i^V(\hat{s}) = \frac{f_i^V(0)}{(1 + \hat{s}/\Lambda_{FF}^2)^n}. \tag{5.2}$$

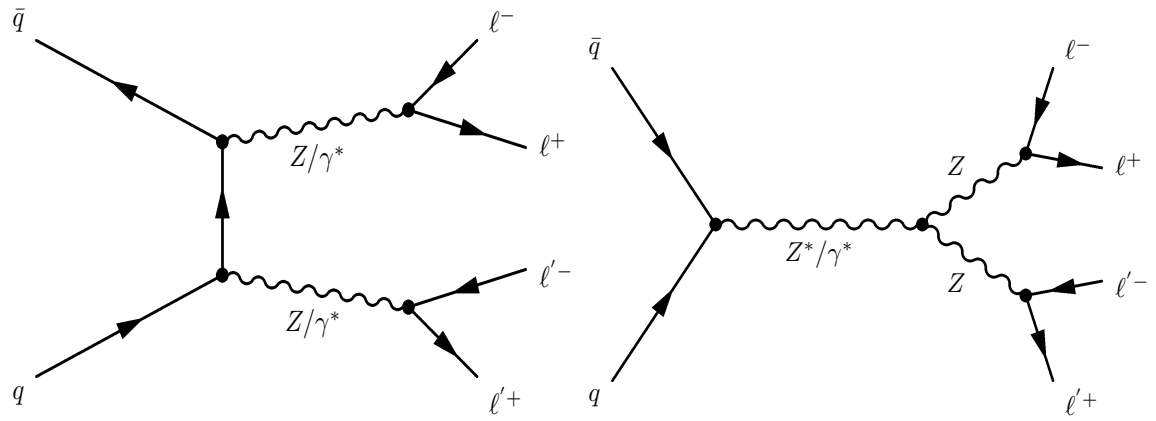

Figure 5.1: Tree level Feynman diagram for $q\bar{q} \rightarrow (Z^*/\gamma^*)(Z^*/\gamma^*) \rightarrow \ell^+\ell^-\ell'^+\ell'^-$. and for $q\bar{q} \rightarrow (Z^*/\gamma^*) \rightarrow ZZ \rightarrow \ell^+\ell^-\ell'^+\ell'^-$. The SM only allows the t-channel diagram and not the s-channel trilinear coupling diagram.

The lower energy value $f_i^V(0)$ (or f_{i0}^V), and n are restricted by partial wave unitarity [44]. In order to preserved unitarity n is required to be greater than 3/2. For a given Λ_{FF} there exists an upper bound on the couplings beyond which unitarity is violated. The couplings f_{i0}^V are found for the largest possible Λ_{FF} for which unitarity is not violated. Following the convention of [44], the variable n is chosen to be 3 in all cases.

5.1 Monte Carlo Event Generators

A Monte Carlo leading order trilinear gauge coupling ZZV event generator [44], denoted the Baur ZZV generator, is used to generate events with the four-vectors of the four final state leptons for each channel [46]. This generator also generates SM ZZ events. The p_T distribution from the four final state leptons is zero due to the fact the initial state gluon radiation is not simulated. The Monte

Carlo event generator PYTHIA which simulates initial state gluon radiation is used to determine the p_T distribution formed from the four final state leptons from Standard Model ZZ production. The four-vectors from the anomalous coupling generator are boosted with the p_T distribution from PYTHIA.

Figure 5.2 shows various comparisons between the PYTHIA event generator and the Baur ZZV generator. Note that for the most part the agreement between the two generators is good. The Baur ZZV generator does not do final state photon radiation which explains some of the discrepancies in the four-lepton and two-lepton invariant mass distributions. Figure 5.2 shows the four-lepton and two-lepton invariant mass with final state radiation disabled in PYTHIA.

The kinematic distributions for ZZV anomalous couplings can differ significantly from what is expected by ZZ production in the Standard Model. Figure 5.4 shows various distributions for the SM and for each of the couplings being 0.5 and the others being zero.

5.2 Event Selection

The lepton and event selection for each channel are identical to that of the SM limit, with the exception of the di-lepton invariant mass cuts. For the SM limit the objective was a search for ZZ and $Z\gamma^*$ production, while for the anomalous couplings involve ZZ only. Accordingly, the di-lepton invariant mass cuts are moved to $M_{ee} > 70$ GeV and $M_{\mu\mu} > 50$ GeV to select a kinematic region dominated by Z pair production rather than $Z\gamma^*$ or $\gamma^*\gamma^*$ production. With this selection, zero

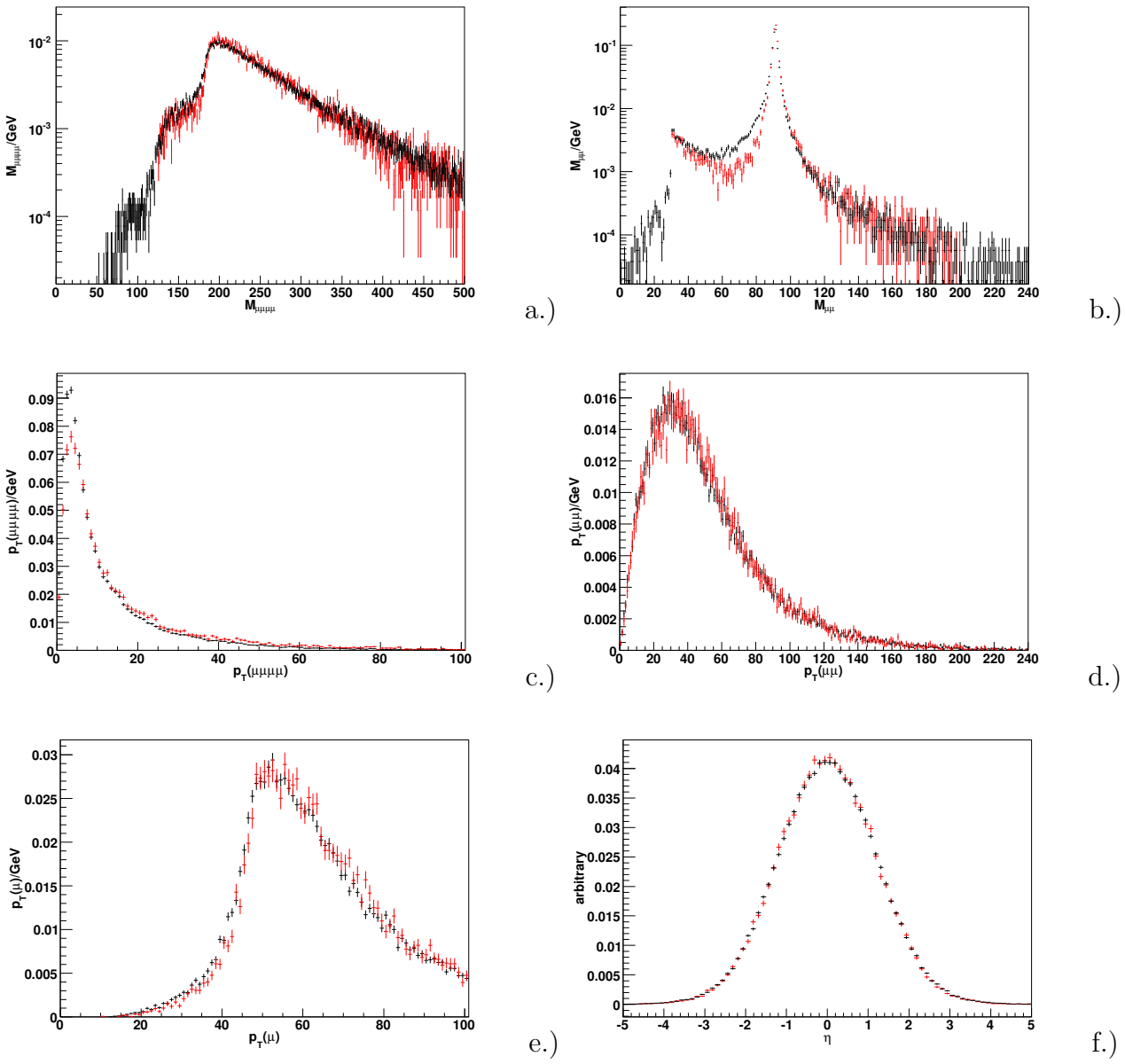

Figure 5.2: Standard Model comparisons between generator level PYTHIA (black points) and Baur ZZV (red points) Monte Carlo event generators: a.) shows the four-lepton invariant mass of the ZZ system, b.) shows the di-lepton invariant mass of the Z bosons. c.) shows the four-lepton p_T of the ZZ system, d.) shows the di-lepton p_T of the Z bosons (the Baur distribution has been boosted with PYTHIA), e.) shows the p_t of the lead electron, and f.) shows the η of the leptons.

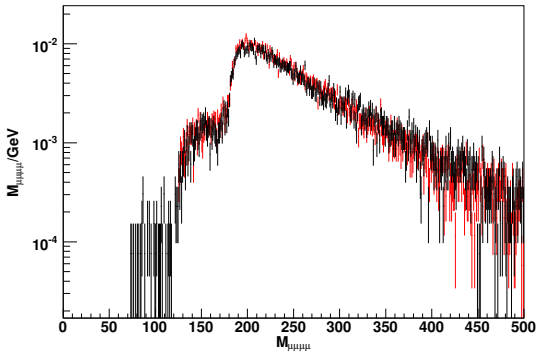

a.)

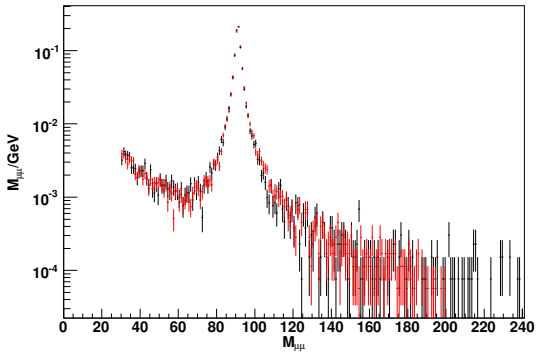

b.)

Figure 5.3: Standard Model comparisons between generator level PYTHIA (black points) without final state radiation and Baur ZZV (red points) Monte Carlo event generators: a.) shows the four-lepton invariant mass of the ZZ system, b.) shows the di-lepton invariant mass of the Z bosons.

candidate events are found.

5.3 Detector Simulation and the Event Acceptance

The same parameterized Monte Carlo used for the SM limit is used to simulate the detector. For comparison the SM acceptance is determined for PYTHIA and the Baur ZZV generator for each channel, these results can be found in Table 5.1. The difference in acceptance calculated with the two generators is 5% in the $\mu\mu\mu\mu$ and $ee\mu\mu$ channels and 1% in the $eeee$ channesl. These uncertainties are less than the 10% uncertainty on the efficiency×acceptance in those channels.

In general, larger anomalous coupling have larger event acceptance. This is mostly due to the fact the lepton p_T is larger on average for anomalous couplings. See Fig. 3. The event acceptance at each grid point is modeled by the detector

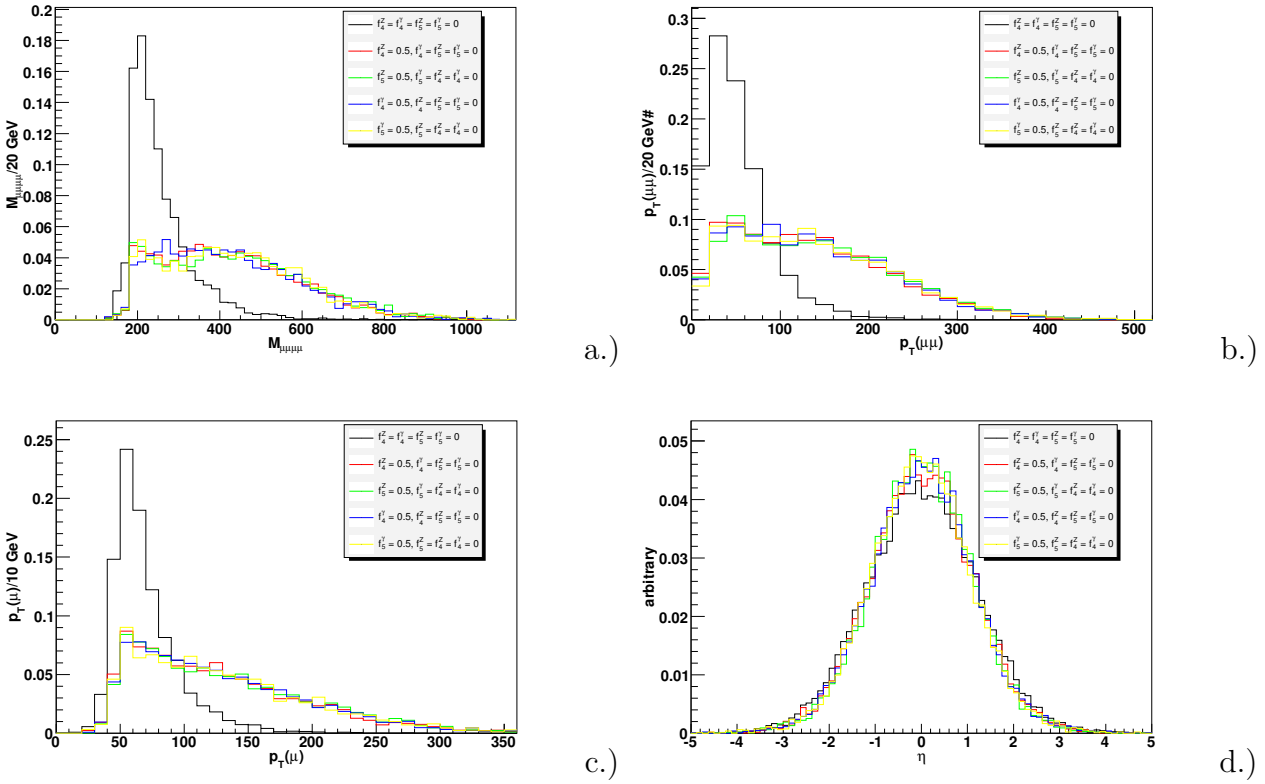

Figure 5.4: Standard Model and anomalous coupling comparisons from the Baur ZZV Monte Carlo generator. Each figure shows five distributions: a.) shows the four-lepton invariant mass of the ZZ system, b.) shows the di-lepton p_T of the Z bosons, c.) shows the p_T of the lead electron, and d.) shows the η of the leptons.

simulation.

Channel	PYTHIA	Baur ZZV	Baur ZZV/Pythia
$\mu\mu\mu\mu$	0.286	0.301	1.05
$eeee$	0.227	0.229	1.01
$\mu\mu ee$	0.226	0.214	1.05

Table 5.1: Standard Model event acceptance for each channel from PYTHIA and the Baur ZZV generator.

5.4 Determining Limits on the Couplings

The cross section and acceptance are determined as a function two parameters for four different grids: f_{40}^{Z} versus f_{50}^{Z}, f_{40}^{γ} versus f_{40}^{Z}, f_{40}^{γ} versus f_{50}^{γ}, and f_{50}^{γ} versus f_{50}^{Z}. The number of points for each parameter is nine yielding 81 points in total for each grid. The range of each parameter was $[-0.5, 0.5]$ in steps of 0.125. The variable Λ was chosen to be 1200 GeV.

The signal s_i for a given grid point i is defined to be

$$s_i = A_i L \tag{5.3}$$

where L is the luminosity in the electron channel. The variable A_i represents the combined acceptance for all channels with the cross section and branching ratios and is defined as:

$$A_i = (\alpha(A\mu)_i + 2\beta(A\mu e)_i + (Ae)_i)\sigma_i Br^2 \tag{5.4}$$

where $A\mu$, Ae, and $A\mu e$ are the acceptances for the $\mu\mu\mu\mu$, $eeee$, and $\mu\mu ee$ channels respectively for the grid point i, α is the ratio of the luminosity in the $\mu\mu\mu\mu$ channel to the luminosity in the $eeee$ channel, β is the ratio of the luminosity in the $\mu\mu ee$ channel to the luminosity in the $eeee$ channel, σ_i is the cross section for the i grid point.

The probability for observing N_i events in a bin with the estimated signal and background events of s_i and b_i is written as

$$P_i = \frac{(s_i + b_i)^{N_i}}{N_i!} e^{-(s_i+b_i)}. \tag{5.5}$$

The overall probability of observing a binned distribution of events is then calculated by:

$$P = \prod_{i=1}^{N_{bins}} P_i. \tag{5.6}$$

The quantities s_i, L, and the background b_i are quantities with uncertainties. We will therefore introduce weighting with Gaussian distributions and integrate them:

$$P' = \prod_{i=1}^{N_{bin}} \int \mathcal{G}_{f_L} df_L \int \mathcal{G}_{f_A} df_A \int \mathcal{G}_{f_b} df_b \frac{e^{-(f_A f_L s_i + f_b b)} (f_A f_L s_i + f_b b)^{N_i}}{N_i!}. \tag{5.7}$$

For convenience, we will use the negative log likelihood values:

$$L = -\ln(P'). \tag{5.8}$$

The background used is 0.13 ± 0.03 events. The uncertainty on A_i is assigned a value of 10%. The luminosity is assigned an uncertainty of 6.1%.

Each grid is fit with a six parameter paraboloid defined as:

$$A + Bx + Cy + Dx^2 + Ey^2 + Fxy \tag{5.9}$$

where x and y are the two parameters of the grid. The fit gives L as a continuous function of the two grid parameters. Figure 5.5 shows the fits for each of the two parameter variations.

One parameter 95% C.L. limits are determined by seting one of the parameters to zero and finding the limits of the other parameter when $\Delta L = 1.92$. Table 5.2 shows the 95% C.L. limits for this analysis and the Lep II 95% C.L. combined limits [48].

Coupling	Lep II limits	This analysis
f_{40}^{Z}	$[-0.30,\ +0.29]$	$[-0.28, +0.28]$
f_{40}^{γ}	$[-0.17,\ +0.19]$	$[-0.26, +0.26]$
f_{50}^{Z}	$[-0.38,\ +0.36]$	$[-0.31, +0.29]$
f_{50}^{γ}	$[-0.34,\ +0.38]$	$[-0.30, +0.28]$

Table 5.2: One parameter 95% C.L. limits from the LepII combined limits and the limits that we have determined.

Two parameter 95% C.L. limits are determined by intersecting a plane at $\Delta L = 3.0$. Figures 5.6 shows the two parameter limits for four different combinations of f_{i0}^{V} and $f_{j0}^{V'}$. The dashed ellipse around the limit shows the unitary bounds contour, all the limits are within the unitarity bounds.

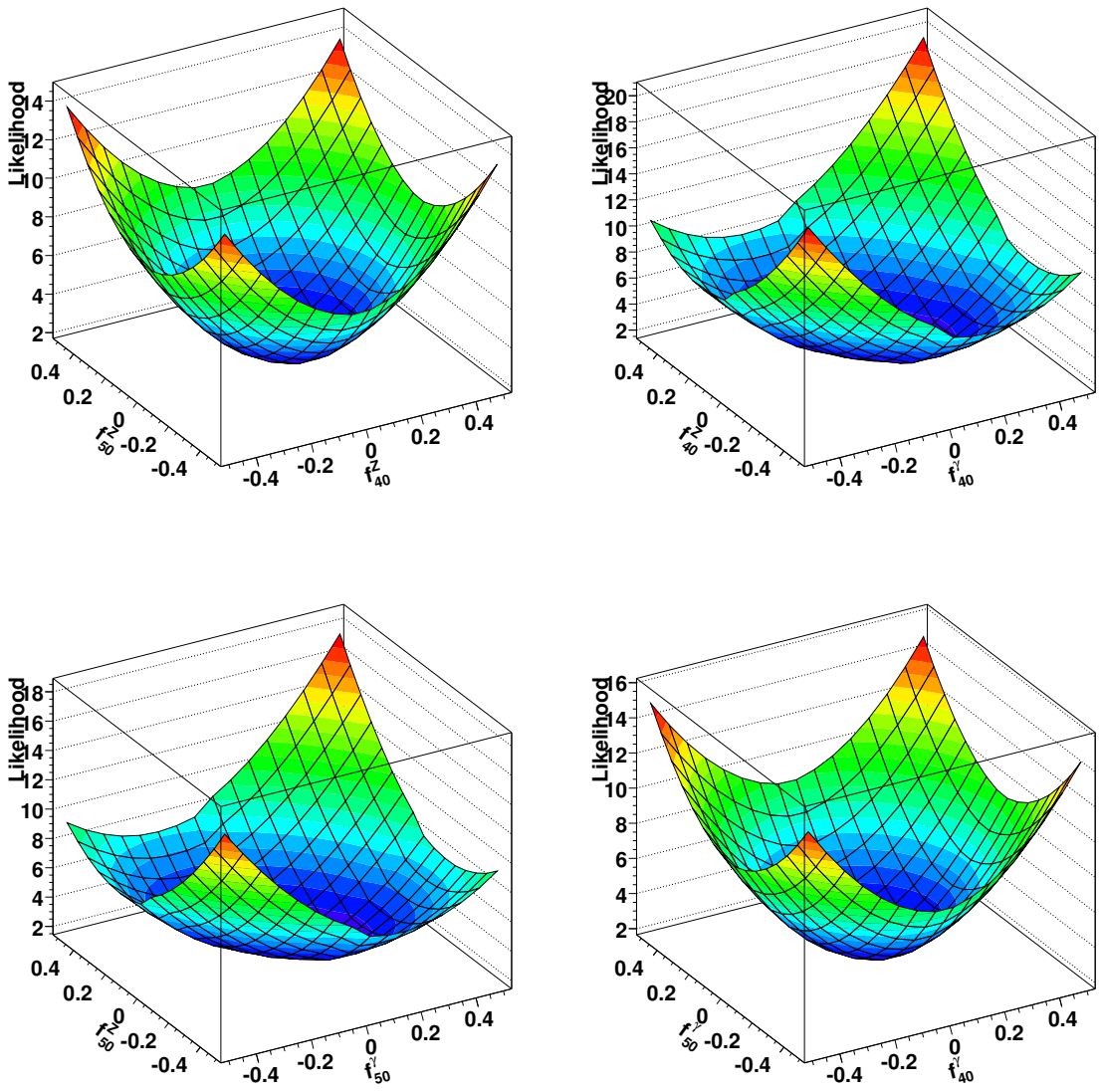

Figure 5.5: Two parameter likelihoods fits for each of the two parameter variations.

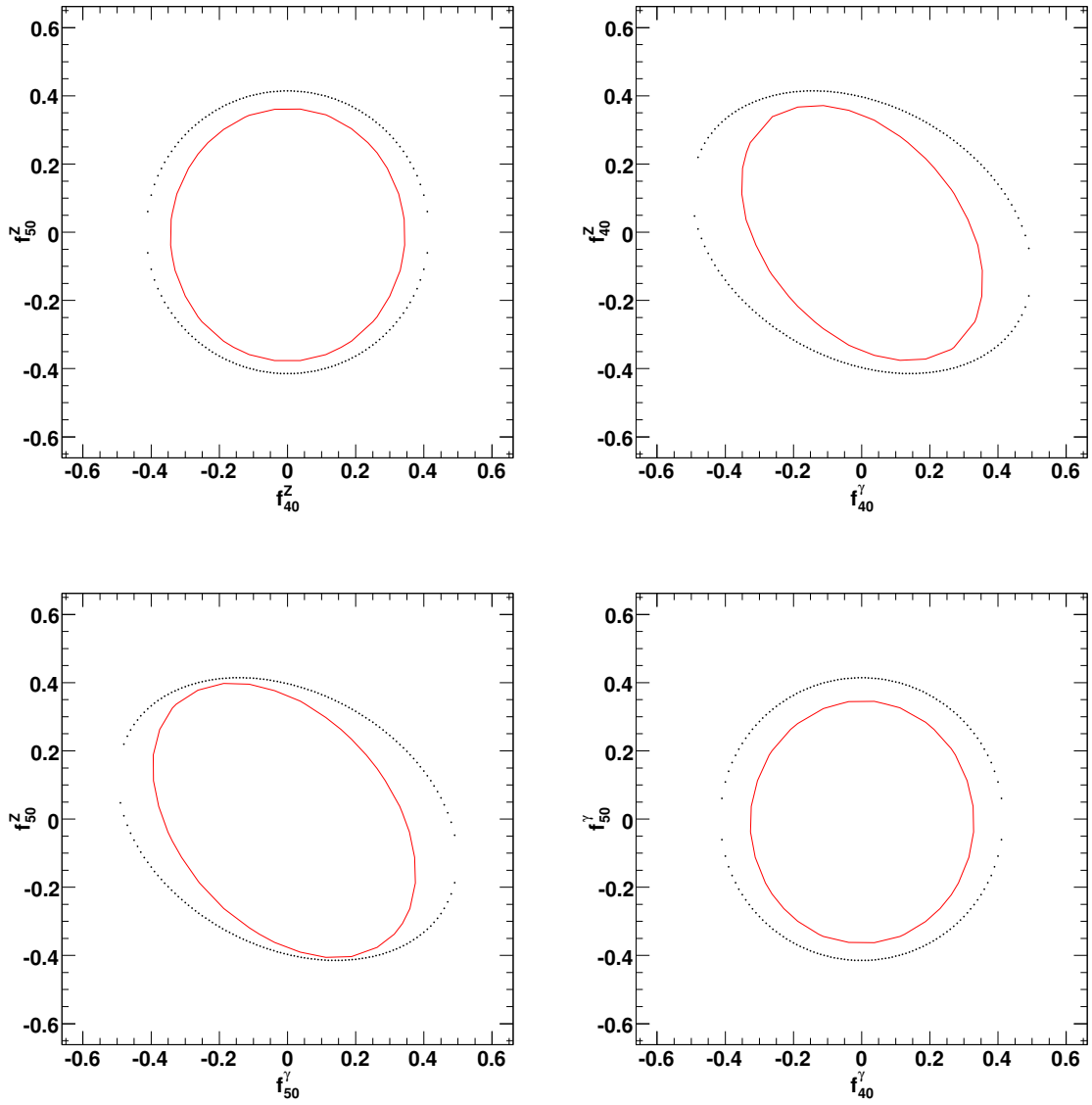

Figure 5.6: Two parameter 95% C.L.limits on ZZV couplings. The solid red line is the 95% C.L. limit and the dotted black line is the bounds for unitarity.

Chapter 6

Conclusions and Future Prospects

In this analysis we have searched for Z boson pair production at $\sqrt{s} = 1.96$ TeV decaying into the $\mu\mu\mu\mu$, $eeee$, and $\mu\mu ee$ final state with approximately 1 fb^{-1} of data. We set a lower limit on the cross section of 4.4 pb at a 95% confidence level. The expected signal was found to be 1.7 ± 0.1 events with a background of 0.13 ± 0.03 events. One candidate event was found in the $\mu\mu ee$ channel. The probability for the background to fluctuate to one event is 12%. In addition, we have determined both one parameter and two parameter 95% C.L. limits on the neutral trilinear gauge couplings ZZZ^* and $ZZ\gamma^*$. There are four couplings labeled f_4^Z, f_4^γ, f_5^Z, and $f_5\gamma$. The couplings have a momentum dependent form factor parametrized by a form factor scale Λ which was chosen in all cases to be 1200 GeV. The coupling limits for f_{40}^Z, f_{50}^Z, and f_{50}^γ are better than LEP II's one parameter limits.

Future iterations of this analysis at the Tevatron have a chance of a 5 σ discovery. Figure. 6.1 shows the expected significance for the selection of this analysis versus luminosity. In addition, other channels could be incorporated such as $ZZ \to \ell^+\ell^-\nu\bar{\nu}$ which, although, it has a larger background source than the four lepton channel and it cannot reconstruct the four momenta of all four leptons, can improve the overall significance for a cross section measurement.

As previously mentioned, the f_5^V coupling does have a one loop contribution

of order 10^{-4}. The Tevatron is sensitive to anomalous ZZV couplings of order 10^{-1}. However, the Large Hadron Collider [49] at CERN will be able to probe the anomalous ZZV couplings down to 10^{-3}.

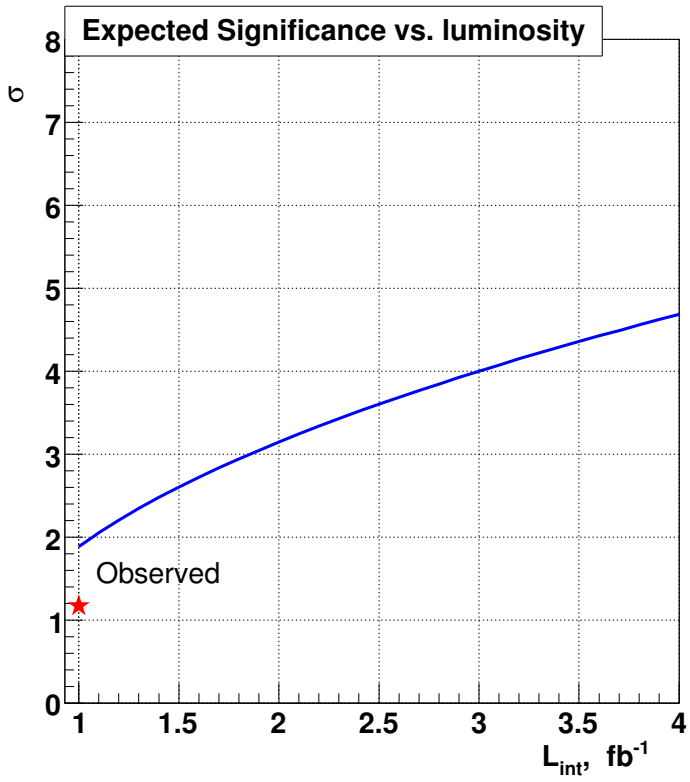

Figure 6.1: Expected significance versus Luminosity.

Appendix A

Rapidity and Pseudorapidty

The velocity transformation of a relativistic particle measured between different frames of reference is not a linear transformation. However, a clever mathematic trick is to parametrize the velocity v in terms of a new parameter denoted rapidity y by:

$$v/c = \tanh y. \tag{A.1}$$

Rapidities do add linearly between frames of reference. Using the relation that $p_z/Ec = v$, where p_z is the longitudinal component of momentum of a particle and E is the total energy of the particle, we can solve for y in Eq. A.1 to get

$$y = \frac{1}{2} \ln \frac{E + p_z c}{E - p_z c}. \tag{A.2}$$

In the case where $v \approx c$ then $v_z/c \approx \cos\theta$ we can approximate Eq. A.1 as

$$\cos\theta = \tanh\eta \tag{A.3}$$

where η, called the pseudorapidty, has replaced y. Solving Eq. A.3 for η we get

$$\eta = -\ln[\tan(\frac{\theta}{2})]. \tag{A.4}$$

An example of Eq. A.4 for $\theta = [0, 180^\circ]$ can be seen in Fig. A.1

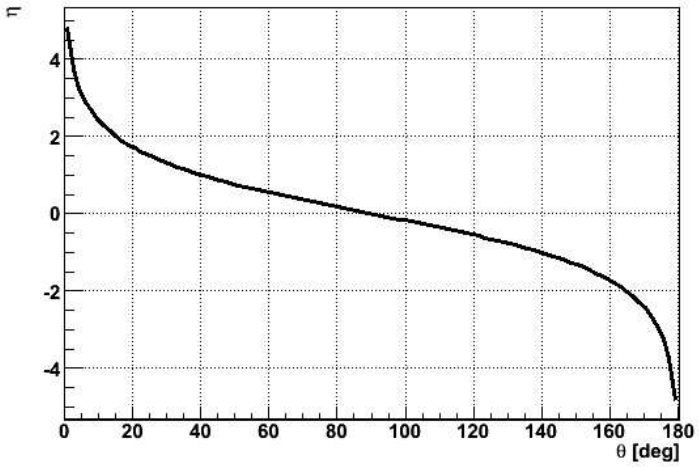

Figure A.1: Pseudorapidty η as a function of angle θ

.

Appendix B

Accelerator Chain

Figure B.1 shows a schematic diagram of the Fermilab accelerator and an aerial photograph of Fermilab. We enumerate the most important components of the accelerator chain as follows:

1. The Proton source - the H^- ion source, the Cockcroft-Walton, the Linac, and the Booster
2. The Anti-proton source - the target, the Debuncher, and the Accumulator
3. The Main Injector and the Recycler
4. The Tevatron

We will briefly discuss each of these components. More details about the Fermilab accelerator can be found in reference [4].

B.1 Hydrogen Ion Source and Cockcroft-Walton

The first stage converts diatomic Hydrogen (H_2) gas into negatively ionized Hydrogen (H^-) gas. The negatively charged hydrogen ions are then boosted, first, with an extractor plate, to an energy of 25 KeV and then to an energy of 750 KeV with a Cockcroft-Walton accelerator. The Cockcroft-Walton is one of the oldest components of Fermilab accelerator apparatus. Figure B.2 shows a photograph of

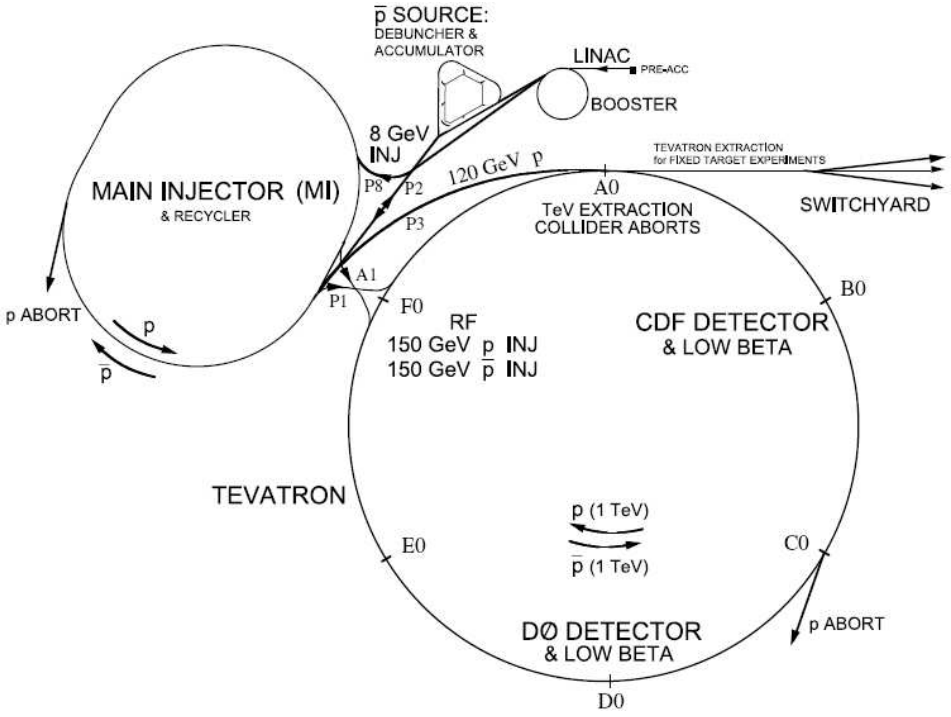

a.)

b.)

Figure B.1: (a) A schematic of the Fermilab accelerator chain. (b) An aerial photograph of Fermilab. For a sense of scale the Main Injector is one kilometer in diameter and the Tevatron is two kilometers in diameter.

the Cockcroft-Walton accelerator. One might expect the monster of Dr. Frankenstein to be created from such a device. The Hydrogen gas resides in a bottle in the dome of the Cockcroft-Walton device. The Cockcroft-Walton is a 750 KV DC voltage source, the voltage is generated by a combination of capacitors and diodes as show in Fig. B.2.

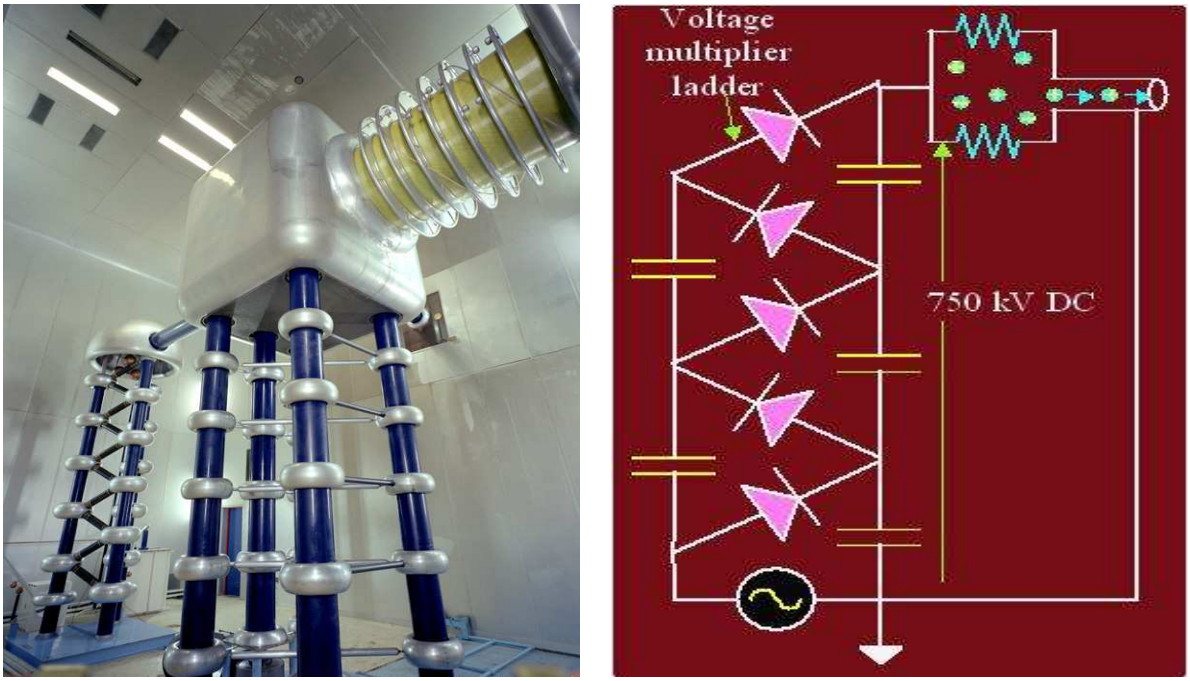

a.) b.)

Figure B.2: (a) A photograph of the Cockcroft-Walton 750kV voltage ladder. (b) An electronic schematic of the Cockcroft-Walton voltage ladder.

B.2 Linac and Booster

After being boosted to 750 KeV, the ions are injected into the Linac, a two stage linear accelerator which is approximately 146 m in length. The first stage of

the Linac is 79 m long and boost the 750 KeV H^- ions to 116 MeV. The second stage is 67 m long and boost the 116 MeV H^- ions to 400 MeV.

In the first stage, the ions are accelerated with RF cavities until the field reverses. At this point, the ions enter a drift tube which shields them from the reversed field. Inside the drift tubes the ions coast (drift) without acceleration. Quadrupole magnets within the drift tubes are used to focus the beam. Once the field reverses again, the ions come out of the drift tubs and experiences a positive field gradient which accelerates the ions between the gaps. As the energy of the H^- ions increases the length of drift tubes and the gaps in between them also increases until the H^- ions reach 116 MeV. Figure B.3 shows a simple drawing of the drift tubes. After reaching 116 MeV, the H^- ions enter the second stage of the Linac. The second stage does not use drift tubes but instead uses side-coupled cavities. This stage operates at four times the resonance frequency of the first stage and boosts the ions to 400 MeV.

The Linac also adds a bunch structure to the beam. In other words, the H^- ions coming out of the Linac come out in pulses (bunches) rather than in a continuous stream.

After the Linac, the H^- ions enter the Booster; the first synchrotron in the accelerator chain. The Booster has a circumference of 475 meters. The H^- ions pass through a thin carbon foil which strips the two electrons of the H^- ions to produce bare protons. The Linac continuously supplies the H^- ions until approximately 3×10^{12} protons accumulate in the Booster at which point the Linac stops delivering H^- ions to the Booster. The protons in the Booster are then accelerated from

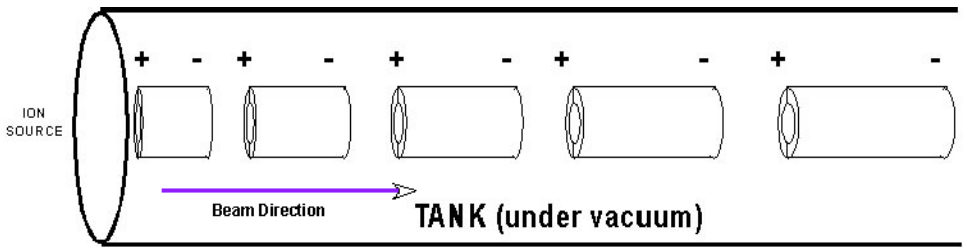

Figure B.3: Drawing of the Linac drift tubes. Note the gaps go from negative to positive charge. When the H^- ions leave the drift tube they accelerate between the gaps.

400 MeV to 8 GeV in about 0.033 seconds. The H^- enter the Booster at about half the speed of light and are boosted to velocities of about 99% the speed of light. The protons are then dumped into the Main Injector, the next synchrotron in the accelerator chain.

B.3 Main Injector and Recycler

The Main Injector is a synchrotron with a circumference of 3.3 km; it serves multiple purposes listed as follows:

- Boosts 8 GeV protons, from the Booster, to 120 GeV and delivers them to the anti-proton source.
- Boosts 8 GeV protons, from the Booster, to 120 GeV and delivers them to the fixed target experiments.
- Boosts 8 GeV protons, from the Booster, to 150 GeV for delivery to the Tevatron.

- Boosts 8 GeV anti-protons, from the Accumulator, to 150 GeV for delivery to the Tevatron.

- Boosts 8 GeV anti-protons, from the Recycler, to 150 GeV for delivery to the Tevatron.

The Recycler is another synchrotron which resides above the Main Injector in the same tunnel. It is a storage ring that always operates at a fixed energy of 8 GeV. The Recycler receives anti-protons from the Accumulator and helps assist the Accumulator in storing anti-protons. The anti-protons in the Accumulator are called the stack and the anti-protons in the Recycler are called that stash. The Recycler or the Accumulator feeds the Main Injector with 8 GeV anti-protons. Additionally, the Recycler receives the remaining anti-protons when a store is ended.

B.4 Anti-proton Source - Target, Debuncher, and Accumulator

The anti-proton source contains three primary components: a fixed target for the production of anti-protons, the Debuncher for conditioning the anti-protons from the fixed target, and the Accumulator for storage of the anti-protons. A drawing of the anti-proton source system can be seen in Figure B.4.

The Main Injector delivers 120 GeV protons to a fixed target made of nickel. Many particles are produced in the violent collision of the 120 GeV protons with the fixed nickel target. These particles pass through a lithium lens, the particles coming out of the lens are mostly in one direction. The particles then pass through a pulsed magnet which acts as a charge mass spectrometer. The pulsed magnet selects anti-

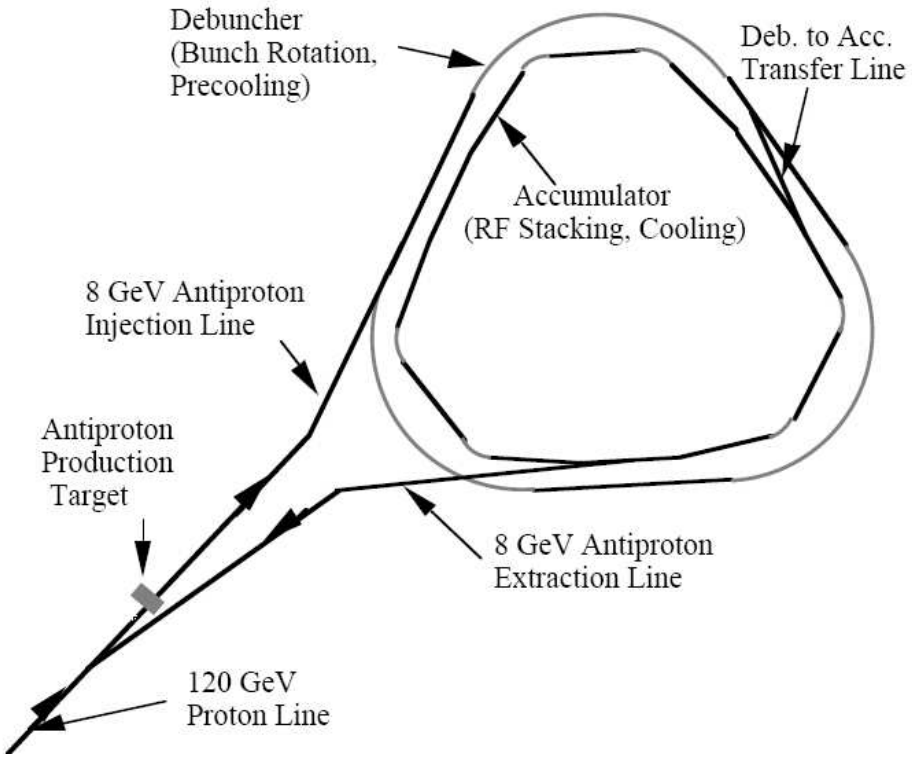

Figure B.4: Drawing of the anti-proton source system

protons and sends them to the Debuncher. A drawing of the Anti-proton station can be seen in Figure B.5

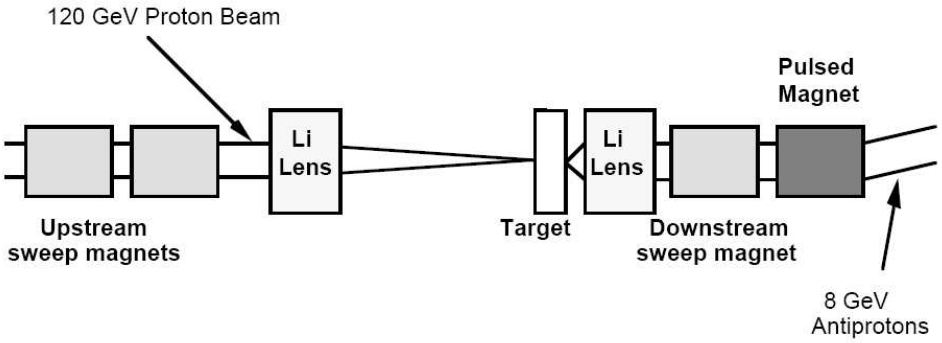

Figure B.5: Drawing of the target station

The Debuncher is another synchrotron with a circumference of 505 m, however, rather than being circular it is shaped more like a triangle. The particles coming from the mass spectrometer have widely varying momenta. However, their velocities are all essentially relativistic. Larger momentum anti-protons will travel a larger path length than lower momentum anti-protons. Therefore, lower energy anti-protons will complete an orbit around the Debuncher in a shorter time than the higher energy anti-protons. By adjusting the phase of the RF cavities the spread in momentum can be reduced after each revolution. This effectively smears out the bunch structure of the beam (hence the name "the Debuncher") in exchange for a narrow spread in momenta. Debunching takes about 100 milliseconds after which the beam can be transfered to the Accumulator.

The Accumulator is a synchrotron with a circumference of 474 m that resides in the same tunnel as the Debuncher; its purpose is basically to stack 8 GeV anti-

protons over many hours from the Debuncher. Stochastic cooling is used to focus the beam in the Accumulator. For every million protons that collide with the nickel target approximately only twenty 8 GeV anti-protons make it to the Accumulator. When a sufficient number of anti-protons has accumulated (of order 10^{12}) stacking is stopped, the anti-protons are further cooled and then transfered to the Main Injector.

Appendix C

Preshower Detectors

The scintillating fibers are triangular shaped and have a larger cross section than the fibers in the CFT detector. The width of a leg of the triangular fibers is 5.9 mm, recall that the CFT fibers are only 0.835 mm thick. Fig. C.1 shows a drawing of the cross section of the preshower scintillating fibers. Like the CFT, VLPCs are used to covert the light in the fibers to an electrical signal.

The number of photons generated in the scintillator is proportional to the energy. The large cross sectional area of the fibers allows for greater photon production and hence the ability to sample the energy of a shower. This early energy sampling is used to measure the start of an electro-magnetic shower.

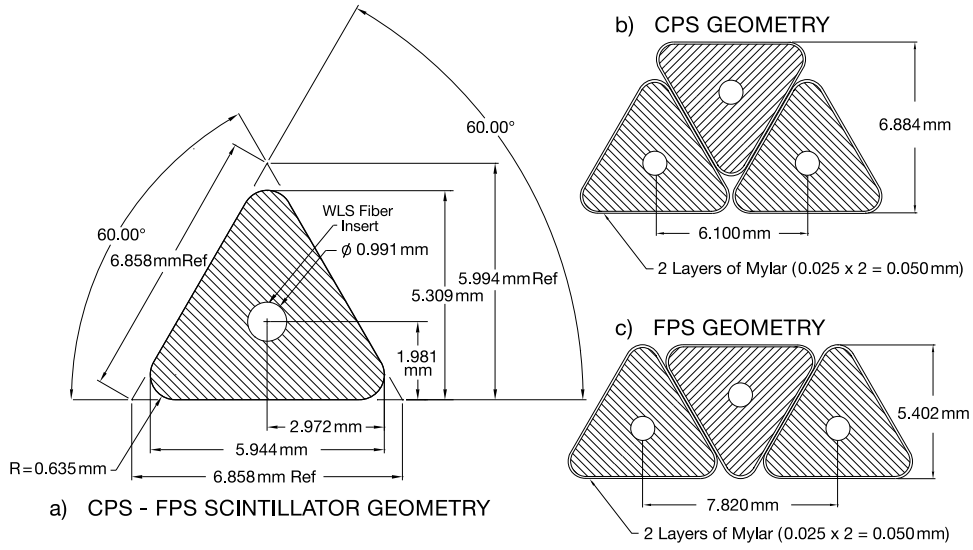

Figure C.1: A drawing of the cross section of the preshower fibers.

The central preshower [7] resides between the solenoid and central calorimeter. The distance between the solenoid and the central calorimeter is about 5 cm. This region is filled first with a layer of lead and then three layers of scintillating fibers. The first layer of fibers is called the axial layer which runs parallel to the beam axis the next two layers are called the stereo u and v layers, tilted 24° and -24° degrees to the beam axis.

The layer of lead promotes particle showers before the scintillating fibers. The thickness of the lead was supposed to be tapered such that any trajectory through the solenoid and lead adds approximately two radiation lengths together, however, this was not implemented and the lead plate has constant thickness. Figure C.2 shows a drawing of the CPS and FPS detectors.

In the region $1.1 < |\eta| < 2.5$ are the forward preachier detectors [8] [9], one for each end cap calorimeter. Each FPS detector has 16 azimuthal 22.5° wedges forming a circle and each wedge has four layers of scintillating fibers. There is no significant mass, such as the solenoid for the CPS, before the FPS detectors to initiate a particle shower. Instead an absorbing lead-stainless-steal plate of approximately two radiation lengths ($2X_0$) is sandwiched between the first two scintillating layers and the last two scintillating layers. The first two layers are known as the MIP (minimum ionizing particle) layers and the layers after the absorbing plate are know as the Shower layers. The MIP layers provide a precise position (η,ϕ,z) measurement of a particle. An electron or photon that passes through the ($2X_0$) lead absorber will readily initiated a electro-magnet shower from which the FPS shower layers can sample the energy. The MIP and shower layers each have a u and v layer. Figure C.3

shows a drawing of the layers in one of the FPS wedges.

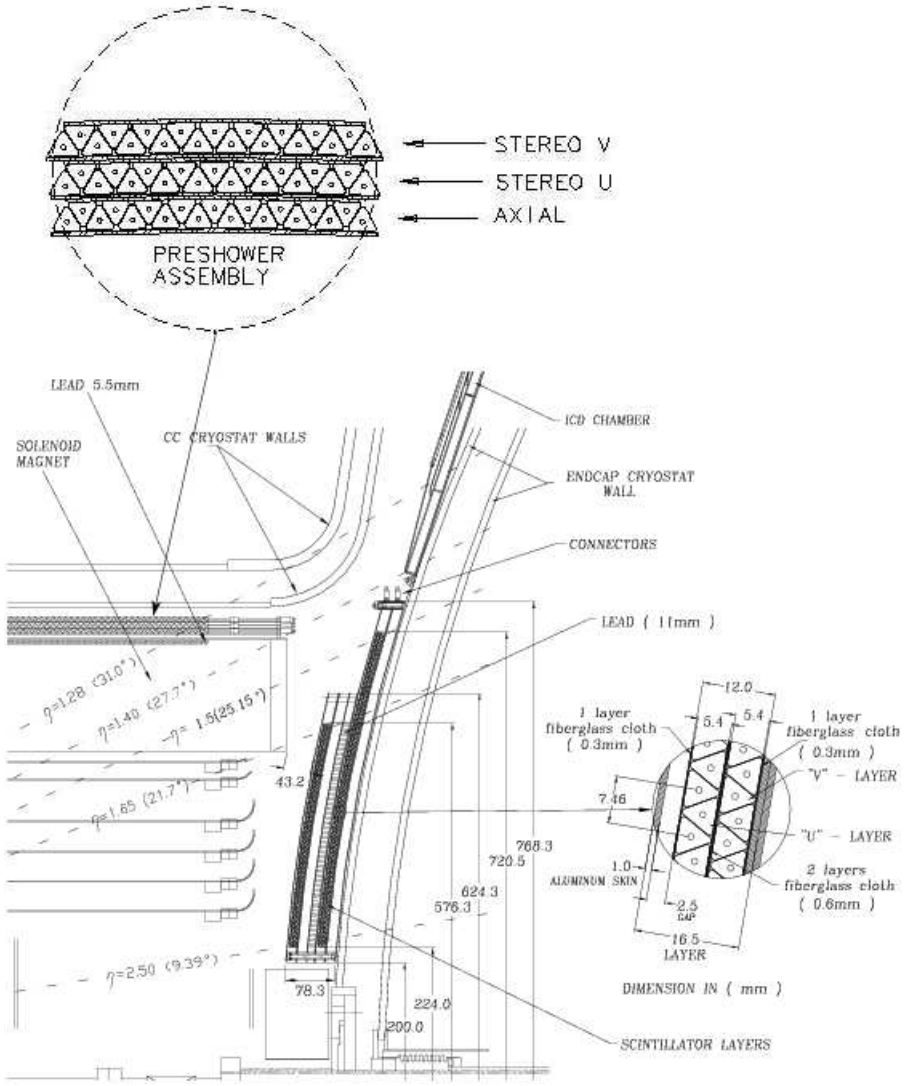

Figure C.2: A schematic of one quarter of the DØ detector highlighting the preshower detectors.

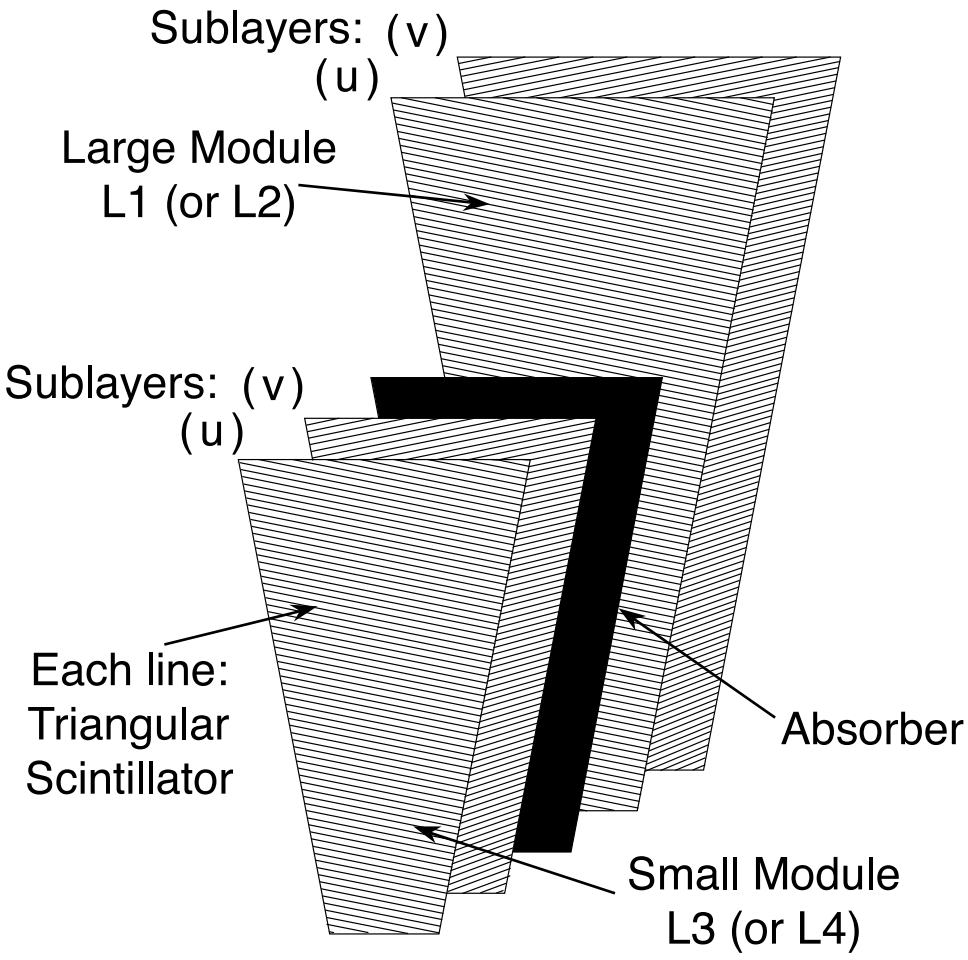

Figure C.3: A drawing of the layers in a wedge of the Forward Preshower. There are two layers of scintillating fibers, called the MIP layers, an absorbing layer of lead, followed by two more layers of scintillating fibers called the shower layers.

Appendix D

QCD Jets Event Weights

Selection	nlk	$nhmx$	weight
4/4	3	x	$f_l(1)$
3/4	3	x	$f_l(1) + f_n(1)$
3/4h	3	x	$f_l(1) + f_h(1)$
0,1,2/4	3	x	$f_l(1) + f_n(1)$
3/4	2	x	$f_l(1)$
3/4h	2	1	$f_l(1)$
0,1,2/4	2	x	$f_l(1) + f_n(1)$
2/4	1	x	$f_l(1)$
0,1/4	1	x	$f_l(1) + f_n(1)$
0/4	0	x	$f_l(1) + f_n(1)$

Table D.1: Event weights for the $eeej$ method: nlk is the number of electrons that passed Likelihood, $nhmx$ is the number of electrons that failed the Likelihood cut but passes the H-Matrix cut , x means the value is irrelevant, $f_l(i)$ is the fake rate for the i-th jet to pass Likelihood, $f_n(i)$ is the fake rate for the i-th jet to fail Likelihood, and $f_h(i)$ is the fake rate for the i-th jet to fail Likelihood but pass the H-Matrix cut.

Selection	nlk	nhmx	eeej
4/4	2	x	$f_l(1)f_l(2)$
3/4h	2	x	$f_l(1)f_l(2) + f_l(1)f_h(2) + f_l(2)f_h(1)$
3/4	2	x	$f_l(1)f_l(2) + f_l1)f_n(2) + f_l(2)f_n(1)$
2,1,0/4	2	x	$f_l(1)f_l(2) + f_l(1)f_n(2) + f_l(2)f_n(1) + f_n(1)f_n(2)$
3/4	1	x	$f_l(1)f_l(2)$
2/4	1	x	$f_l(1)f_l(2) + f_l(1)f_n(2) + f_l(2)f_n(1)$
1,0/4	1	x	$f_l(1)f_l(2) + f_l(1)f_n(2) + f_l(2)f_n(1) + f_n(1)f_n(2)$
3/4h	1	1	$f_l(1)f_l(2)$
2/4	0	x	$f_l(1)f_l(2)$
1/4	0	x	$f_l(1)f_l(2) + f_l(1)f_n(2) + f_l(2)f_n(1)$
0/4	0	x	$f_l(1)f_l(2) + f_l(1)f_n(2) + f_l(2)f_n(1) + f_n(1)f_n(2)$

Table D.2: Event weights for the $eejj$ method: nlk is the number of electrons that passed Likelihood, $nhmx$ is the number of electrons that failed the Likelihood cut but passes the H-Matrix cut , x means the value is irrelevant, $f_l(i)$ is the fake rate for the i-th jet to pass Likelihood, $f_n(i)$ is the fake rate for the i-th jet to fail Likelihood, and $f_h(i)$ is the fake rate for the i-th jet to fail Likelihood but pass the H-Matrix cut.

Selection	nlk	$nhmx$	$ee\mu j$ event weight
2/2	2	0	$f_\mu(1)$
1/2+hmx	2	0	$f_\mu(1)$
1/2+hmx	1	1	$f_\mu(1)$

Selection	nlk	$nhmx$	$\mu\mu ej$ event weight
2/2	1	0	$f_l(1)$
1/2+hmx	1	0	$f_l(1) + f_h(1)$
1/2+hmx	0	1	$f_l(1)$

Selection	nlk	$nhmx$	$eejj$ event weight
2/2	2	0	$f_\mu(1)f_\mu(2)$
1/2+hmx	2	0	$f_\mu(1)f_\mu(2)$
1/2+hmx	1	1	$f_\mu(1)f_\mu(2)$

Selection	$\mu\mu jj$ event weight
2/2	$f_l(1)f_l(2)$
1/2+hmx	$f_l(1)f_l(2) + f_l(1)f_h(2) + f_l(2)f_h(1)$

Table D.3: Event weights for determining the background in the $\mu\mu ee$ channel for the $ee\mu j$, $\mu\mu ej$, $eejj$, $mmjj$ methods

Bibliography

[1] Chris Quigg, "The Electroweak Theory",hep-ph/0204104

[2] J. M. Campbell, R. K. Ellis "An update on vector boson pair production at hadron colliders", hep-ph/9905386.

[3] Review of Particle Physics, "Journal of Physics G",2006, Volume 33, `http://pdg.lbl.gov`

[4] J. Thompson, "Introduction to Colliding Beams at Fermilab", FERMILAB-TM-1909 (1994);
`http://www-bd.fnal.gov/lug/runII\_handbook/RunII_index.html`

[5] The DØcollaboration,"D0 Silicon Tracker Technical Design Report", `http://www-d0.fnal.gov/trigger/stt/sttcommiss.html/smt_tdr.ps`

[6] The DØcollaboration,"The D0 Upgrade: Central Fiber Tracker, Technical Design Report", D0 internal note 4164

[7] M. Adams et al., "Design Report of the Central Preshower Detector for the DØ upgrade", `http://d0server1.fnal.gov/users/qianj/CPS/index.htm`

[8] A. Gordeev et al., "Technical Design Report of the Forward Preshower Detector for the DØ upgrade", DO internal note 3445

[9] Abid Patwa,"The Forward Preshower System and a Study of the $J\psi$ Trigger with the DØ detector", (PhD dissertation, State University of Sony Brook, 2002)

[10] Junjie Zhu,"Direct Measurement of the W Boson Decay Width in Proton-Antiproton Collisions at $\sqrt{s} = 1.96$ TeV", (PhD dissertation, University of Maryland, College Park 2004)

[11] K. De, P. Draper et al.,"Technical Design Report for the Upgrade of the ICD for DØ Run II", D0 internal note 2686

[12] V.M. Abazov. et al.,"The muon system of the Run II DØ detector", Nuclear Instruments and Methods in Physics Research A 552 (2005) 372-398

[13] M. Wetstein et al.,"Determination of the Sampling Term for the CC of Region of the EM Calorimeter in Run II", NEED REFERENCE.

[14] F. Fleuret et al., "The DØ Electron/Photon Analysis Package EMAnalyze", http://www-d0.fnal.gov/d0dist/dist/packages/em_analyze/devel/doc/EMAnalyze_doc.ps

[15] Philippe Calfayan et al., "Muon Identification Certification for p17 data" D0 internal note 5157

[16] O. Peters,"Muon Segment Reconstruction", http://www-d0.fnal.gov/~deliot/fitalg.ps

[17] Frédéric Déliot,"The Fit Algorithm in muo_trackreco", http://www-d0.fnal.gov/~deliot/fitalg.ps

[18] Gavin Hesketh et al.,"The Content of the p17 Muon Thumbnail" D0 internal note 4735

[19] Philippe Calfayan et al.,"Muon Identification Certification for p17 data " D0 internal note 5157

[20] V. M. Abazov et al., "Measurement of the ttbar production cross section in pbarp collisions at sqrt(s) = 1.96 TeV using secondary vertex b tagging", Phys. Rev. D 74, 112004 (2006)

[21] PYTHIA,http://www.thep.lu.se/~torbjorn/Pythia.html

[22] Paul Telford,"The Pmcs_chpt Package" D0 internal note 4923

[23] Drew Alton, Jens-Peter Konrath,"Energy measurements with the central preshower detector", D0 internal note 4665

[24] Emmanuel Buasto, Bernard Andrieu,"Jet Algorithms in the DØ Run II Software: Description and Users Guide", D0 internal note 4457

[25] Bing Zhou, Qichun Xu, James Degenhardt, "Parameterized MC Simulation (PMCS) muon package" D0 internal note 4065, Dec. 2002

[26] A. Khanov,"HTF: Histogramming method for finding tracks", D0 internal note 3778, 2000

[27] G. Borisov,www-d0.fnal.gov/global_tracking/talks/20030228/talk-adm-030228.ps

[28] H. Greenlee,"The DØ Kalman Track Fit", D0 internal note 4303, Jan. 2004

[29] H.T.Diehl, "C-Hole Scintillation Counter Design and D0Gstar Geometry", DØ Note 4088, Jan. 2005.

[30] "C-Hole Scintillation Counter Installation and Testing", http://www-clued0.fnal.gov/~harringt/newScintCount.pdf

[31] M. Sanders, "Beam Position Monitoring in Real Time", DØ Note 4755, Mar. 2005.

[32] C. Jarvis, M. Sanders, T. Yasuda, "Occurrence of High Muon Multiplicity Events after April 2005", DØ Note 5083, April 2006

[33] R.Rucinski, R.P.Smith, "Present Status of the D0 Solenoid', DØ Note 4804, Mar. 2005.

[34] Boris Tuchming et al.,"Muo_cert package", http://www-d0.fnal.gov/d0dist/dist/releases/development/muo_cert/doc/muo_cert.ps

[35] John Hayes, et al.,"The Program Package em_cert ", DØ Note 5070

[36] C.Jarvis, "A study of the D0 muon detector response and an update to the loose identification and tracking efficiencies for PMCS", DØ Note 5076

[37] J. Degenhardt, A. Alton, B. Zhou, A. Askew, "Observation of WZ Diboson Production in Trilepton Final States from pbarp Collisions with 2001-2006 DZero Data", DØ Note 5110, June 2006

[38] PMCS,http://www-d0.fnal.gov/computing/MonteCarlo/pmcs/pmcs_doc/pmcs.html

[39] Emily Nurse, Paul Telford, "Measurement of $\sigma \times Br$ for $(Z/\gamma)* \rightarrow \mu^+\mu^-$ and $Z \rightarrow \mu^+\mu^-$ in $p\bar{p}$ collisions at $\sqrt{s} = 1.96TeV$", DØ Note 4689.

[40] P.Telford, "The Pmcs_chprt Package", DØ Note 4923

[41] Heidi Schellman, "The longitudinal shape of the luminous region at D0", DØ Note 5142, June 2006.

[42] A. Baden, S. Eno, C. Jarvis, J. Mans, T. Toole, M. Yan, "Measurement of the shape of the boson rapidity distribution for $p\bar{p} \rightarrow Z/\gamma^* \rightarrow e^+e^- + X$ events produced at $\sqrt{s}$ of 1.96 TeV" DØ Note 5247, Nov. 2006.

[43] Alexey Ferapontov, Yurii Maravin, "Study of Zgamma events in D0 Run II p17 data", DØ Note 5156.

[44] U. Baur, D. Rainwater, "Probing neutral gauge boson self-interactions in ZZ production at hadron colliders", Phys. Rev. D 62, 113011 (2000)

[45] G.J. Gounairs, J. Layssac, F.M. Renard, "Off-shell structure of the anomalous Z and γ self-couplings" Phys. Rev. D 62, 073012 (2000)

[46] For the Baur ZZV generator the following input parameters are used: $\sin^2\theta_W = 1-(M_W/M_Z)^2 = 0.2226$, $M_Z = 91.187$ GeV, $M_W = 80.4$ GeV, $\alpha(M_Z) = 1/128$, and $\alpha_s(M_Z) = 0.118$. The parton distribution function set is CTEQ5HJ, with a factorization scale $\mu_f = x_1 x_2 s$.

[47] Chad Jarvis, Nick Hadley, Michiel Sanders "A search for Z boson pair production decaying into the $\mu\mu\mu\mu$, $eeee$, $\mu\mu ee$ final states with 1 fb^{-1} of data." , DØ Note 5081.

[48] The LEP Collaborations, " A Combination of preliminary electroweak measurements and constraints on the standard model", hep-ex/0612034

[49] "The Large Hadron Collider", `http://lhc.web.cern.ch/lhc/`